

A theory-guided combinatorial materials design of ductile Mg-based alloys utilizing ab initio and atomistic methods

Von der Fakultät für Georessourcen und Materialtechnik der
Rheinisch-Westfälischen Technischen Hochschule Aachen

**zur Erlangung des akademischen Grades eines
Doktors der Ingenieurwissenschaften**

genehmigte Dissertation

vorgelegt von M.Sc.

Zongrui Pei
aus Henan, China

Berichter: Prof. Dr.-Ing. Dierk Raabe
Univ.-Prof. Dr. rer. nat. Robert Svendsen
Prof. Dr. Jörg Neugebauer

Tag der mündlichen Prüfung: 12. August 2015

Diese Dissertation ist auf den Internetseiten der Universitätsbibliothek online verfügbar.

Do the difficult things while they are easy and do the great things while they are small. A journey of a thousand miles must begin with a single step.

– Lao Tzu

Acknowledgements

Firstly I am grateful to Dr. Martin Friák, Prof. Dr. Jörg Neugebauer, Prof. Dr. Dierk Raabe and Prof. Dr. Bob Svendsen for their long-lasting support and supervision of my thesis. I have found my PhD topic, that they had originally chosen, truly great and it was my pleasure to work on it. Dr. Martin Friák brought me into an interesting research area of quantum-mechanical calculations and guided me through (sometime difficult) times with his broad knowledge and great patience. Prof. Dr. Jörg Neugebauer directed my work with his deep insight and, importantly, provided me with a highly stimulating research environment in his department. Many thanks to our experimental colleagues, Dr. Stefanie Sandlöbes, Dr. Stefan Zaefferer and Prof. Dr. Dierk Raabe for their experimental work that was excellently complementing my theoretical research. I would like to greatly thank Dr. Li-Fang Zhu, who patiently taught me basic as well as very advanced skills related to the VASP software. I really learned a lot from her. From Prof. Dr. Bob Svendsen and Dr. Duancheng Ma I learned a lot of crucial details about various dislocation models that have turned out to be very important for my PhD thesis. I will never forget their kindness.

Further I wish to express my appreciation for our colleagues Dr. Roman Nazarov, Dr. Björn Lange, Dr. Blazej Grabowski, Dr. Christoph Freysoldt, Dr. Mira Todorova and Dr. Biswanath Dutta who constantly answered my many small questions and gave me their patient guidance, kind help and encouragement during my PhD studies. Also I would like to express my gratitude to Ugur Aydin, Albert Glensk and Dr. Tillmann Hickel who helped me to solve many issues related to the German language. Dr. Tillmann Hickel translated the abstract of this thesis into German.

Next, I would like to thank to all members of both our high-performance computing service team and the administrative department. Without their hard work and kind help, I would not have been able to happily enjoy my stay in Max-Planck-Institut für Eisenforschung GmbH.

I am also very thankful to my friends Xie Zhang, Dr. Ying Cui and Dr. Liangfeng Huang for their providing me with enlightenment and encouragement during my hard work. I very much appreciate my parents and my girlfriend for their believing in me and their constant encouragement to do what I want. Without their spiritual and financial support it would have been impossible for me to continue my study and research in Germany. Finally I would like to thank for the financial supports provided by both the Deutsche Forschungsgemeinschaft (DFG) through the Aachen Institute for advanced study in Computational Engineering Science (AICES) and the Max Planck Society.

Abstract

Energy savings and CO₂ reductions are among the most essential tasks in materials science and engineering. Any successful attempt to achieve both goals requires the development of novel light-weight metallic materials. New Mg alloys play a key role owing to their combination of relatively high strength and low density. However, their wider use is hindered by their low room temperature ductility. Recent mechanical testing of pure bulk Mg and of a single phase solid solution Mg-3-wt.-%-Y performed at the Max-Planck-Institut für Eisenforschung (MPIE) in Düsseldorf, Germany, showed that the addition of yttrium increases the room temperature ductility about 5 times and lowers the so-called I₁ intrinsic stacking fault (I₁ SF) energy. In order to obtain a deeper insight into the mechanisms responsible for this increased ductility, the above described experimental studies have been complemented at MPIE by a quantum-mechanical study. Using density functional theory (DFT) calculations, Y additions were found to significantly reduce the I₁ SF energy in excellent qualitative agreement with experiments.

This thesis contains a thorough analysis of the above mentioned scale-bridging connection between atomic-scale reduction of I₁ SF energies and an increased macroscopic ductility in Mg alloys. DFT calculations of I₁ SF energies in 20 different binary Mg-alloys have been performed but only rare-earth elements have been found to reduce the I₁ SF energy and increase the ductility. This prediction was experimentally confirmed at MPIE in case of Mg-Tb, Mg-Dy, Mg-Ho, Mg-Er alloys that all turned out to be ductile. When designing new ductile Mg alloys, rare earth elements do not represent an optimum choice due to their limited natural resources and environmental concerns in their mining and production. In order to identify alternative solutes ductilizing Mg alloys, we have searched for relations between materials properties of elemental solutes and their impact on the I₁ SF energies in Mg alloys. The atomic volume, the electronegativity and bulk modulus of elemental solutes have been found related to the I₁ SF energies and we propose a single numerical indicator based on these three inter-relations. Evaluating this new indicator for 76 binary Mg alloys, we hardly find any alternative to rare-earths. Therefore, we extended our search to ternary alloys and relatively high number of pairs of non-rare-earth solutes have been predicted to reduce the the I₁ SF energies.

Next, aiming at simulations involving a higher number of atoms, an embedded atom method (EAM) potential for Mg-Y alloys was developed. Both DFT and EAM simulations have shown changes of energy barriers within generalized stacking fault energy surfaces (so-called gamma surfaces) due to Y additions. Importantly, these changes sensitively depend on the dislocation slip plane and direction. Extending our DFT calculations to a broader set of 20 binary Mg alloys, we have evaluated changes in energy barriers and Peierls stresses. In order to reduce the number of input energies for gamma surfaces, a new computational approach was developed and the computed gamma surfaces were used within the Peierls-Nabarro model to determine the dislocation properties. All the above summarized findings have deepened our fundamental understanding of plasticity in Mg materials and have been used to propose ductile rare-earth-free alloys.

Zusammenfassung

Energieeinsparungen und CO₂-Reduktion gehören derzeit zu den wichtigsten Herausforderungen der Materialwissenschaft. Erfolgreiche Ansätze, um diese beiden Ziele zu erreichen, erfordern die Entwicklung neuartiger Leichtmetalle. Neue Mg-Legierungen spielen aufgrund ihrer Kombination von verhältnismäßig hoher Festigkeit und geringer Dichte dabei eine Schlüsselrolle. Allerdings wird deren Einsatz durch die geringe Dehnbarkeit bei Raumtemperatur derzeit verhindert. Kürzlich durchgeführte mechanische Test an reinem Mg-Volumenmaterial und an einphasigen Mg- 3Y (wt.%) Legierung am Max-Planck-Institut für Eisenforschung (MPIE) in Düsseldorf haben gezeigt, dass das Hinzufügen von Yttrium die Dehnbarkeit bei Raumtemperatur um einen Faktor 5 erhöht und die so-genannte I₁ intrinsische Stapelfehler (SF)-Energie erniedrigt. Um ein tieferes Verständnis der Mechanismen, die ursächlich für den Anstieg der Verformbarkeit sind, zu bekommen, wurden die zuvorgenannten experimentellen Studien am MPIE durch theoretische quanten-mechanische Studien ergänzt. Unter Verwendung von Dichtefunktionaltheorie (DFT) wurde herausgefunden, dass Y-Zusätze die I₁ SF-Energie erheblich reduzieren, was eine exzellente qualitative Übereinstimmung mit dem Experiment darstellt.

In dieser Dissertation wurde die zahlenübergreifende Verbindung zwischen der Reduktion der I₁ SF-Energie auf der atomaren Skale und dem makroskopischen Anstieg der Dehnbarkeit weitergehend untersucht. DFT-Rechnungen der I₁ SF-Energien von 20 verschiedenen binären Mg-Legierungen wurden durchgeführt, wobei nur Seltene-Erd-Elemente eine Reduktion der I₁ SF-Energie und einen Anstieg der Dehnbarkeit zeigten. Diese Vorhersage wurde experimentell am MPIE in den Fällen von Mg-Tb, Mg-Dy, Mg-Ho und Mg-Er-Legierungen bestätigt, die sich allesamt als dehnbar erwiesen. Bei der Herstellung neuer, dehnbarer Mg-Legierungen stellen Seltene-Erd-Elemente allerdings keine optimal Wahl dar, weil deren natürliches Vorkommen begrenzt und deren Abbau und Produktion ökologisch bedenklich sind. Um alternative Legierungskomponenten zu finden, die Mg-Legierungen dehnbar machen, haben wir nach Zusammenhängen zwischen den Materialeigenschaften elementarer Legierungselemente und deren Einfluss auf die I₁ SF-Energie in Mg-Legierungen gesucht. Das atomare Volumen, die Elektronegativität und der Kompressionsmodul haben einen solchen Zusammenhang gezeigt und basierend auf diesen drei Werten konnten wir eine einzige Kennzahl vorschlagen. Eine Auswertung dieser Kennzahl für 76 binäre Mg-Legierungen ergab kaum Alternativen zu den Seltenen Erden. Wir haben daher unsere Suche auf ternäre Legierungen erweitert und eine relativ hohe Zahl von Legierungselement-Kombinationen verhertgesagt, die nicht zu den Seltenen Erden gehören und die I₁ SF-Energie reduzieren.

Zusätzlich, wurde ein Embedded-Atom (EAM) Potential für Mg-Y entwickelt, um Simulationen mit einer größeren Zahl von Atomen durchführen zu können. Sowohl DFT- als auch EAM-Simulationen haben eine Änderung der Energiebarrieren auf der verallgemeinerten Stapelfehler-Energieoberfläche (sog. Gamma-Oberfläche) durch Y ergeben. Es ist dabei wichtig, dass diese Änderungen empfindlich von der Versetzungs-Gleitebene und

der Richtung abhängen. In einer Ausweitung unserer DFT-Rechnungen auf einen umfangreicherer Satz von 20 binären Mg-Legierungen haben wir die Änderung der Energiebarrieren und Peierls-Spannungen ausgewertet und die berechneten Gamma-Oberflächen schließlich als Eingangsgröße für ein Peierls-Nabarro-Modell zur Bestimmung der Kernstruktur von Versetzungen verwendet. Dabei haben wir einen neuen numerischen Ansatz verwendet, der die Zahl der notwendigen Eingangsparameter erheblich reduziert.

Contents

Acknowledgement	i
Abstract	ii
Zusammenfassung	iv
1 Introduction	1
1.1 Motivation	1
1.2 Physical Foundation of Magnesium and Magnesium Alloys	2
1.2.1 Crystallographic Structures	3
1.2.2 Dislocations and Stacking Fault	4
1.3 State of the Art of Magnesium Research: History and Methods	6
2 Theoretical Background	10
2.1 Schrödinger Equation	10
2.2 Born-Oppenheimer Approximation	11
2.3 The Electronic Problem	12
2.4 Density Functional Theory	12
2.4.1 The Hohenberg-Kohn Theorems	13
2.4.2 The Kohn-Sham Equations	14
2.4.3 Approximations to E_{xc} : Climbing Jacob's Ladder	16
2.5 Bloch Theorem	17
2.6 Introduction of Molecular Statics	18
3 Binary Mg Alloys	20
3.1 Introduction	20
3.2 Computational Methodology	20
3.2.1 ANNNI Model for E_{SF1}	20
3.2.2 Computational Parameters	22
3.2.3 Murnaghan Equation of State	22
3.3 Results and Discussion	24
3.3.1 Mg-Y Alloys	24
3.3.2 Mg-RE Alloys	28
3.3.3 Mg-non-RE Alloys	35
3.4 Conclusions	40

4 Inter-relations between SFE and Properties of Elemental Solutes	41
4.1 Introduction	41
4.2 Computational Methodology	42
4.3 Results	43
4.3.1 Relation between ΔI_1 SFE($Mg_{15}X$) and Volumes	43
4.3.2 I_1 Stacking Fault Energies in Pure Solutes and Mg Alloys	44
4.3.3 I_1 Stacking Fault Energies and the Atomic Number of Solutes	45
4.3.4 I_1 Stacking Fault Energies and Electronegativity	46
4.3.5 I_1 Stacking Fault Energies and Bulk Modulus	48
4.4 Discussion	49
4.5 Conclusions	56
5 Ternary Mg Alloys	59
5.1 Introduction	59
5.2 Computational Methodology	60
5.2.1 Yttrium Similarity Index of Ternary Mg Alloys	60
5.2.2 Computational Detail	60
5.3 Results	62
5.3.1 Yttrium Similarity Index	62
5.3.2 Ab Initio Computed Stacking Fault Energies	62
5.4 Conclusions	65
6 Generalized Stacking Fault Energies in Mg and Mg-Y Alloys	67
6.1 Introduction	67
6.2 Computational Methodology	68
6.2.1 Concept of Gamma Surface	68
6.2.2 Computational Detail	70
6.2.3 Development of Mg-Y EAM Potential	71
6.3 Results and Discussion	75
6.3.1 The Three Primary Slip Systems	75
6.3.2 GSF of Non-basal Plane Slip	78
6.3.3 Gamma Surface of Non-basal Plane	83
6.4 Conclusions	84
7 The Solute Solution Effect in Mg Alloys	85
7.1 Introduction	85
7.2 Computational Methodology	86
7.2.1 Peierls-Nabarro Model	86
7.2.2 Plane Wave Expansion of the Gamma Surface	88
7.2.3 Computational Parameters	89
7.3 Gamma Surface Analysis	89
7.4 The five GSFEs of Mg alloys	95
7.5 Dislocation Properties	98

7.5.1	Pure Mg	98
7.5.2	Mg Alloys	100
7.6	Case Study of Error Propagation in the Peierls-Nabarro Model . . .	101
7.7	Conclusions	105
8	Conclusions: Design of Novel Ductile Mg Alloys	106
	Bibliography	110
	Appendices	117
	Curriculum Vitae	122

Chapter 1

Introduction

1.1 Motivation

Light weight alloys have recently drawn a lot of attention in material science and engineering communities. Applicable in, for example, automobile and aerospace industries, light-weight Mg alloys are very attractive metallic materials combining low density and high specific strength [1, 2, 3, 4]. The density of pure magnesium is 1.738 g/cm^3 , which is only two thirds of aluminum density and one fifth of iron. Magnesium is also the eighth most abundant element in the Earth's crust, where it contributes about 2.3 wt.% [5]. Therefore magnesium alloys are promising excellent structural materials.

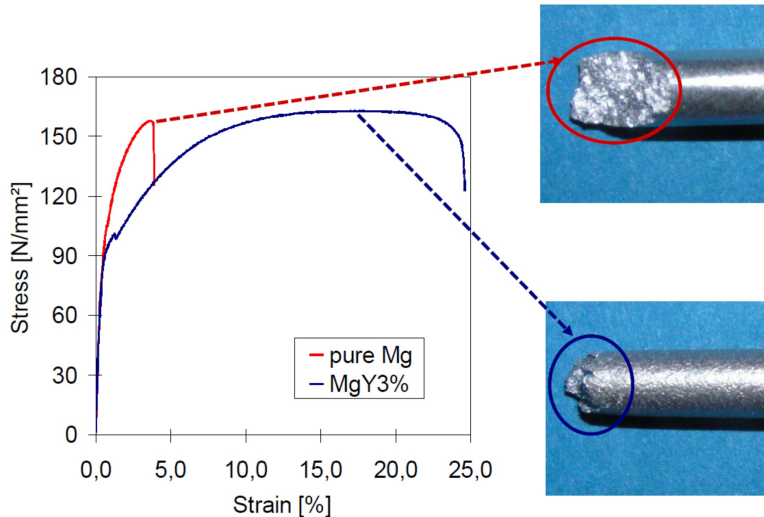


Figure 1.1.1:

Experimental stress-strain curves of tensile tests at room temperature of both pure Mg and a Mg-3wt.-%-Y alloy showing an enhanced ductility in the latter. The rough fracture cross-section of pure Mg and the significantly contracted area of cross-section of Mg-Y indicate the ductility of these materials. (courtesy of Dr. S. Sandlöbes [6])

However the poor room temperature deformability of Mg-alloys is a critical obstacle hindering a wider use of these materials [7] (see Figure 1.1.1). The poor ductility

can be explained by the von Mises criterion [8]. According to this criterion at least 5 independent deformation modes are required to be active in order to accommodate plastic deformations. Magnesium unfortunately does not fulfill this criterion. The strongly anisotropic crystallographic structure causes major differences in the onset of different slip systems. For example, the Peierls stress of prismatic $\langle a \rangle$ slip is 40 times higher than that of basal $\langle a \rangle$ slip and the basal and prismatic slips can anyway only supply 4 independent slip modes. Therefore the non-basal modes ($\langle c+a \rangle$ slip or twinning) are important for arbitrary plastic deformation in Mg alloys.

In 1959 Couling *et al.* [9] investigated the mechanical properties of magnesium alloyed with rare-earth (RE) elements, and they found them more ductile than pure Mg. Their work shed light to the improvement of poor room temperature formability of Mg. Recent mechanical testing of pure bulk magnesium and of a single phase solid solution Mg-3-wt.-%-Y showed that the addition of yttrium increases the room temperature ductility about 5 times [6] (see Figure 1.1.1). Applying transmission electron microscopy (TEM), the densities of I_1 intrinsic stacking faults, non-basal dislocations and twins were found increased by yttrium additions. For example, $\{10\bar{1}1\}$ and $\{10\bar{1}2\}$ twins (also called double twins) are not only more often observed in Mg-Y alloys than in pure Mg but also more homogeneously distributed in the microstructure.

However, rare earth elements have recently become increasingly expensive due to their limited natural resources and environmental concerns related to their mining and production. Therefore, it is important to find alternative non-rare-earth elements to replace rare earth solutes. In order to achieve this goal we need to first obtain a deeper insight into the mechanisms by which rare earth additions ductilize Mg-alloys. In order to realize this objective, density functional theory (DFT) and the Embedded Atom Method (EAM) based molecular dynamics simulations have been performed. Quantum-mechanical approaches have the advantage of being parameter-free and thus independent on experimental data that may be difficult or even impossible to collect.

1.2 Physical Foundation of Magnesium and Magnesium Alloys

In simulations, the structures of materials are the most important parameter. So in this section the ground state crystallographic structures of magnesium and the relevant defects (e.g. dislocation, stacking fault and twin) are reviewed. The deformation mechanisms of materials (or more exactly polycrystals) include inter-granular grain boundary accommodation and intra-granular slip. Our current study is focused on intra-granular mechanisms.

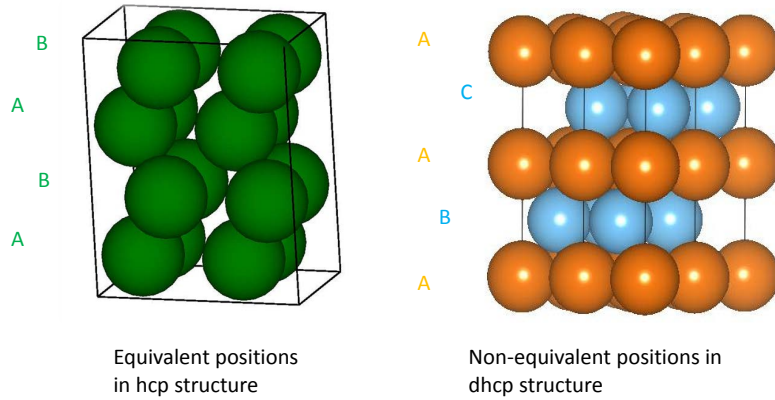


Figure 1.2.1:

Schematic view to sketch the equivalent and non-equivalent positions. Different colors represent non-equivalent positions (layers), and atoms with same color are in equivalent positions. In the dhcp structure, yellow A and blue B,C represent two non-equivalent positions (layers). In hcp green A and B represent the positions (layers) that are equivalent. The figure is created using VESTA [10].

1.2.1 Crystallographic Structures

At room temperature and standard pressure, magnesium atoms are bonded with each other in a hexagonal closed packed structure (hcp, see Figure 1.2.1) with a c/a ratio (1.624) that deviates marginally from the ideal value of 1.633. The hcp (0001) atomic layers repeat in alternate manner (...ABAB... A and B represent two different atomic layers). Apart from Mg, there are 19 elements that are of hcp crystallographic structure in nature.

In the hcp structure, every magnesium atom has the exactly same environment. Therefore in a limited system (e.g. a supercell), if one magnesium atom is replaced by a different atom to make a binary Mg alloy (e.g. $Mg_{15}Y$), there is only one choice. If a solute is put in an A-layer, its next neighbor layers are two B-layers (...BAB...); If the solute is put in a B-layer, its next neighbor layers are two A-layers (...ABA...). The two cases are geometrically equivalent (two A-layers). Just rotate ...ABA... by 60° around the c-axis going through B atom sites (c-axis is the axis perpendicular to the basal plane of hcp), the two geometries are exactly same.

In nature there exists another type of hexagonal close-packed crystallographic structure which is very similar to hcp, namely double hcp structure (dhcp, see Figure 1.2.1). In dhcp structure there are three different types of atom layers, denoted by A, B and C,

and the periodic stacking is ...ABAC

However, in the dhcp structure there are two non-equivalent atomic sites. If a solute is put in a B or C layer, its neighbor layers are A-layers (...ABA... or ...ACA...). B layer and C layer are equivalent by a translation and a rotation of 60° around the c-axis going through A atomic sites. The second non-equivalent position lies on a A layer, with neighbor layers B and C (...BAC... or ...CAB...). The different neighbor layers determine that the A and B/C layers are not equivalent.

1.2.2 Dislocations and Stacking Fault

Even though there is lack of dislocations to accommodate the deformation in hcp metals, the sorts of dislocations are abundant (see Table 1.2.1 and Figure 1.2.2). These dislocations can be put into three groups according to their slip directions: $\langle a \rangle$, $\langle c \rangle$ and $\langle c+a \rangle$. The easy slips are $\langle a \rangle$ types, e.g. basal $\langle a \rangle$, prismatic $\langle a \rangle$ and pyramidal $\langle a \rangle$ slips. The hard $\langle c \rangle$ and $\langle c+a \rangle$ slips can supply the necessary fifth slip, therefore they are very important. The $\langle c+a \rangle$ slips are frequently observed in experiment, so they play important role in improving the ductility of magnesium. According to the indices of a slip plane $\{hkil\}$, the $\langle c+a \rangle$ dislocations are also named by pyramidal I $\langle c+a \rangle$, pyramidal II $\langle c+a \rangle$, and so on.

Table 1.2.1:
Independent deformation modes in hcp crystals.

Slip Systems	Direction	Plane	Independent deformation modes
$\{0001\}\langle 11\bar{2}0 \rangle$	$\langle a \rangle$	basal	2
$\{10\bar{1}0\}\langle 11\bar{2}0 \rangle$	$\langle a \rangle$	prismatic	2
$\{10\bar{1}l\}\langle 11\bar{2}0 \rangle$	$\langle a \rangle$	pyramidal	4
$\{hki0\}\langle 0001 \rangle$	$\langle c \rangle$	-	-
$\{hkil\}\langle 11\bar{2}3 \rangle$	$\langle a+c \rangle$	prismatic	5

Based on dislocation theory the energy of a dislocation with Burgers vector \vec{b} is assessed approximately by [11]

$$E = \frac{1}{2}Gb^2 \quad (1.2.1)$$

where G is shear modulus. Since the energy is proportional to the square of the Burgers vector \vec{b} , a dislocation can reduce its energy by decomposing into partial dislocations. The preconditions for the dissociation of dislocations include (i) a geometrical condition and (ii) an energy condition.

The geometrical condition:

$$\vec{b}_0 = \vec{b}_1 + \vec{b}_2 \quad (1.2.2)$$

The energy condition:

$$E_0 > E_1 + E_2 \quad (1.2.3)$$

where

$$E_i = \frac{1}{2}Gb_i^2 \quad (i = 0, 1, 2), \quad (1.2.4)$$

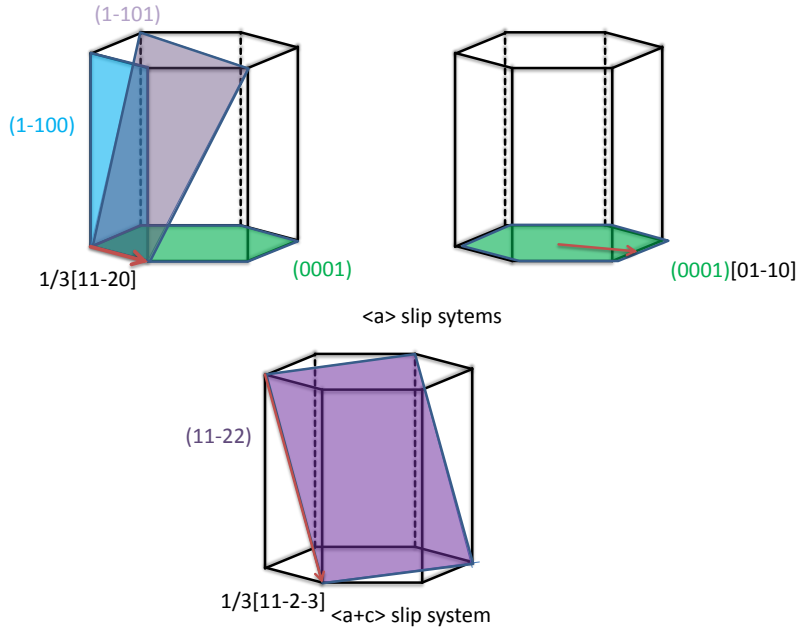


Figure 1.2.2:

Scheme of possible slip systems in hcp metals. The colored planes are the corresponding slip planes of the slip systems listed in Table 1.2.1, and the red arrows indicate their slip directions.

\vec{b}_i are the Burgers vectors of a perfect dislocation or of partial dislocations, E_i the corresponding energy of dislocation. Only if the two conditions are fulfilled simultaneously, the dislocation can dissociate. The area between two partial dislocations is a stacking fault. The formation energy of a stacking fault is supplied by the energy gain due to dislocation dissociation. Therefore the dissociation width is limited. In hcp metals, there are two intrinsic stacking faults (l_1 , l_2) and one extrinsic stacking fault.

Here we focus specifically on the l_1 stacking fault that is schematically shown in Figure 1.2.3 as the stacking fault has a simple structure which is frequently observed in experiment and also inexpensive in *ab initio* calculations. The l_1 stacking fault is characterized by a short dhcp stacking sequence separating two hcp sequences. The energy of the l_1 stacking fault can be derived from Eq. 6.2.2 by *ab initio* calculation.

Using experimental data the energy of the l_1 stacking fault (or stacking fault energy, denoted by γ^{SF}) can usually be calculated by Eq. 1.2.5 [12, 13, 14, 15]. The equation is a result of a balance between the repulsive force of the two partial dislocations and the stacking fault energy.

$$\gamma^{SF} = \frac{Gb^2}{8\pi d} \frac{2-\nu}{1-\nu} \left(1 - \frac{2\nu}{2-\nu} \cos 2\beta\right) \quad (1.2.5)$$

Here G is the shear modulus, ν Poisson's ratio, b the Burgers vector of the partials, β the angle between the partials, and d the spacing of the partials.

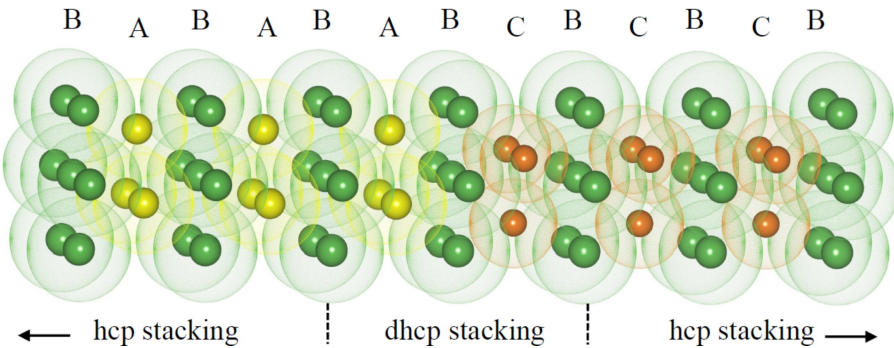


Figure 1.2.3:

Schematic drawing of the I_1 stacking fault characterized by a short double hexagonal close-packed (dhcp) ABCB stacking sequence separating two hcp sequences ABABAB (on the far left, green: atoms in B layers and yellow: atoms in A layers) BCBCBC (on the far right, green: atoms in B layers and orange: atoms in C layers). The transparent clouds around the cores have van der Waals radii. The overlap of two envelops indicates atomic bonding.

1.3 State of the Art of Magnesium Research: History and Methods

Experimentally, there are several processing ways that can improve the ductility of Mg alloys, e.g. refinement of grain size, utilization of lower strain rates, elevation of application temperature to activate more deformation modes (dislocations or twins). Finer grain size and increase of more active deformation modes can be accomplished by adding alloying elements. The present study is primarily focused on defects in hexagonal close-packed magnesium which are deformation modes (dislocations) or potential nucleation sites for the deformation modes (e.g., I_1 stacking faults).

In 1956 Hauser *et al.* firstly found that the addition of Li could dramatically increase the ductility of brittle magnesium [16]. Since their findings were reported, the investigation of Mg-Li alloys has become an active research area [17, 18, 19]. These investigations are not limited to the single α phase (hcp structure) but include also Li-rich β phase (bcc structure) which emerges when the concentration of Li increases. The underlying mechanism of enhanced ductility of α -solid solution Mg-Li alloys was studied by Agnew *et al.* [19] via transmission electron microscopy. By comparing the microstructure of pure Mg and Mg-15 at.-%-Li, they found a higher density and more uniform distribution of $\langle c+a \rangle$ dislocations which supply the necessary deformation. The β phase Mg-Li alloys were investigated by Counts *et al.* [20] systematically. They studied a dense set of solutes as the ternary elements in Mg-Li alloys but unfortunately ended up with no elements being able to increase both the strength and ductility [21]. The addition of Li can not increase the ductility of Mg without reducing the material's specific strength. However, these alloys are chemically unstable and easily oxidized at room temperature.

In 1959 Couling *et al.* first reported that the cold formability of Mg could be significantly

increased by adding rare earth (RE) elements in dilute concentrations [9]. Since that time numerous studies have been undertaken to understand the mechanism of increased ductility of Mg-RE alloys [22, 23, 6]. However the underlying mechanisms are still unclear. In a recent study of Sandlöbes *et al.* [6], the improvement of ductility in Mg-Y alloys is related to higher activities of $\langle c+a \rangle$ dislocations, in line with the finding of Agnew *et al.* in Mg-Li alloys. In contrast to Agnew *et al.*, Sandlöbes *et al.* also found twinning (pyramidal $\langle 10\bar{1}2 \rangle$ contraction and secondary twinning) also relevant for the enhanced ductility. These findings are basis and starting point of our present study.

Majority of macro-scale properties of materials (e.g. yielding stress) represent collective behaviors of defects at all relevant scales (e.g. dislocations). The multi-scale complexity of materials behaviors can not be directly assessed within the framework of density function theory due to limited computational resources. To go beyond these computational limitations, multi-scale models are being developed and used or other methods are used. These are either not based on electronic-structure calculations (such as atomistic methods) or they combine quantum-mechanical (QM) calculations with other non-QM approaches.

The modeling methods simulating dislocation can be classified as either direct and indirect. The direct methods construct dislocation structure (moving million atoms) and relax the structure by molecular dynamics. The main reason that we need a big supercell in simulation of dislocation is the long range interaction of dislocation stress field (the force vanishes in r^{-1} style, r is the distance from dislocation core). As these system sizes are impossible to assess fully quantum-mechanically, atomistic potentials are used to describe inter-atomic interactions. However it's not easy to generate good empirical potentials and their parametrization is time-consuming. The accuracy of the potential has to be checked before it's used to compute a specific physical property, since atomistic potentials are often parametrized so as to reproduce only rather limit set of specific physical properties and their applicability to predict other properties can be very limited. Specifically in case of elemental Mg, only a few parameterizations of, for example, so-called embedded atom method (EAM) potentials exist. Often used are those developed by Sun [24] and Liu [25], which were applied to study the basal and prismatic dislocations in pure Mg by Yasi *et al.* [26].

Next to increasing the size of computational supercells, another method is to apply flexible boundary condition (FBC) which was firstly proposed by Sinclair *et al.* in 1978 [27]. In the FBC method, the supercell consists of three regions. The first region is the core region which includes the core and its surrounding in which the force cannot be described by continuum elasticity due to the large distortions. The atoms in this region are allowed to fully relax using density functional theory and the region-boundary forces pass to the second region by using an elasticity model. The atoms in the second region change their position according to the calculated displacements. The outmost is the third region where atoms are fixed. The overall effect is that atoms in the core region move as if they are in an infinite space and there is no artificial force from the system boundary. The drawback of the method is its high computational costs.

Table 1.3.1:

The ladder of dislocation simulations: selected simulation methods and dislocation properties accessible by them.

Rung	Methods	Properties	Representative Work
First	SFE/ γ -surface	I_1 SFE (ductility), restoring force	our work [34, 37] Tsuru [38]
Second	PN/PF	Core, Peierls stress	Schoeck [39]
	MD-EAM/DFT-FBC	Core, Peierls stress	Nogaret [40], Yasi [26]
Third	PN+models	CRSS	Ma [41]
	MD-EAM/DFT-FBC+models	CRSS	Leyson [42]

The indirect methods are multi-scale models. Multi-scale models bridge the gap between atomic scale and micro-scale which is usually not accessible by either atomic simulations or experiments. The input parameters of these models are usually able to be computed directly by quantum-mechanical approaches; the outputs are the macro-scale properties which can be measured by experiments. When simulating dislocations, popular models are phase field (PF) models and Peierls-Nabarro (PN) model. From mathematical point of view, phase field model has one extra gradient term compared with the Peierls-Nabarro model, which is important for dislocations with compact cores. In our study Peierls-Nabarro model is employed since the dislocation cores in question are wide.

The input of Peierls-Nabarro model is so-called generalized stacking fault energies (GSFEs) or gamma surface, which has been introduced by Vitek in 1968 [28]. Gamma surface is a very useful method to find out the stable stacking fault and unstable stacking fault and their energies on a slip plane. These stacking fault energies are key quantities in determination of dislocation nucleation and mobility in metals with high symmetrical crystallographic structure, for example face-centered cubic. For metals with hexagonal close-packed structures, though the physical meaning of these quantities is unclear, many works has been accomplished in computation of these generalized stacking faults and connection between them and dislocation behaviors or even ductility of materials has been attempted [29, 30, 31, 32, 33, 34].

We believe it's more appropriate to use gamma surface as input of Peierls-Nabarro model in order to obtain the dislocation core structure and the Peierls barrier (or Peierls stress, the maximum gradient of the barrier), which are directly comparable to experimental ones. Many researchers have performed such computation for fcc metals. e.g. palladium [35], aluminum [36].

We briefly summarize all these methods and the accessible physical quantities by the methods in Table 1.3.1. The first rung is the calculation of GSFE. Special type of GSFE (I_1 SFE) is found to correlate with ductility of Mg. Although the underlying mechanism is unknown, it's still a good quantity to indicate ductility of Mg alloys and serves as guiding parameter for selection of solutes in ductile Mg alloys. In the second rung, Peierls-Nabarro (PN) model is necessary to calculate the core structures of dislocation

and Peierls stress. It's not the only pathway but there are two more parallel methods based on molecular dynamics (MD) [43, 44]. Peierls stress is the critical stress to move a single dislocation without consideration of other obstacles, for example, other dislocations and solutes. These external forces introduced by such obstacles are included in the experimentally measured critical resolved shear stress (CRSS). To compute CRSS, models (e.g. solute strengthening model) which describe the geometry of a dislocation and the concentration profile of solutes are proposed [42, 45]. These models employ the dislocation core structure and the solute volume as input information. This is the third rung of the dislocation ladder.

Chapter 2

Theoretical Background

This chapter introduces the theoretical background of methods employed in the simulations performed in the following chapters. Specifically, it includes the fundamentals of quantum mechanics and density functional theory (DFT) [46, 47]. Calculations based on DFT have been very successfully predicting materials properties and revealing atomistic phenomena with an unprecedented level of accuracy [48, 49].

Simulations based on DFT provide a solution to materials problems from an electronic-structure point of view. Due to the fact that fundamental laws of quantum mechanics are applied, and no experimental inputs are needed to run these simulations, these methods are referred to using the Latin term *ab initio*.

This chapter deals with only the general theory, not computational methods. The specific methods employed in each chapter will be described in the methodology section of the chapter.

2.1 Schrödinger Equation

The fundamental law in quantum mechanics is Schrödinger equation, which is a basic assumption that cannot be derived from other physical laws. Its role in quantum mechanics is similar as Newton's second law in classic mechanics. It applies to describe the behaviours of all quantum-mechanical systems. In principle, by solving the Schrödinger equation of a specific system all information can be accessed.

Materials systems from the "real world" usually consist of huge amount of atoms, and each atom with multiple electrons. These systems are referred to many-body or many-particle systems. The Hamiltonian of such a system reads

$$H = \sum_i^{N_e} \left[-\frac{1}{2} \nabla_i^2 \right] + \sum_I^{N_I} \left[-\frac{1}{2M_I} \nabla_I^2 \right] + \frac{1}{2} \sum_I^{N_I} \sum_{I'}^{N_I} \left[\frac{Z_I Z_{I'}}{|\vec{R}_I - \vec{R}_{I'}|} \right] - \sum_i^{N_e} \sum_I^{N_I} \left[\frac{Z_I}{|\vec{r}_i - \vec{R}_I|} \right] + \frac{1}{2} \sum_i^{N_e} \sum_{i'}^{N_e} \left[\frac{1}{|\vec{r}_i - \vec{r}_{i'}|} \right] \quad (2.1.1)$$

where N_e is the number of electrons, N_I the number of ions (or nuclei), M_I the mass

of the I^{th} ion, R_I and r_i represent the positions of the I^{th} ion and the i^{th} electron, respectively. In Eq. 2.1.1, relativistic effect is neglected and atomic units have been used (e.g. $e = 1$, $m_e = 1$, $h/2\pi = 1$ and $1/4\pi\epsilon_0 = 1$). The first term is the kinetic energy of the electrons and the second term the kinetic energy of the nuclei. So the first two terms together are the kinetic energy of the system. The third term corresponds to the Coulomb repulsion between nuclei. The fourth term represents the electron-nucleus Coulomb attraction. The fifth term is the repulsive Coulomb interaction between electrons. The last three terms together are the Coulomb interaction of all particles. Once the Hamiltonian of a system is defined, the static Schrödinger equation of the system is

$$H\Psi = E\Psi. \quad (2.1.2)$$

Ψ is the eigenfunction of the system which corresponds to the energy eigenvalue E . By solving the Eq. 2.1.2, the wavefunction and energy of the system can be determined firstly and all other physical properties can be produced based on them as well. Unfortunately, the exact analytical or even numerical solution of it is prohibitively complicated to reach. In realistic many-body systems, the number of particles is of the order of Avogadro's constant, $N_A = 6.023 \times 10^{23}$. It is impossible and impractical to solve a problem of this size by utilizing the state-of-the-art supercomputers. Therefore, some approximations are necessary. These methods of approximation will be introduced in the following sections.

2.2 Born-Oppenheimer Approximation

Born and Oppenheimer realized that the nuclei move so slowly (with respect to electrons) that the electrons at any time are able to fully adapt to ionic positions [50]. That is to say, the electrons can respond to the nuclei motion almost instantaneously. In this case the motions of electrons and ions can be decoupled and treated separately. The approximation of the wavefunction for the decoupled system is,

$$\Psi(\{\vec{r}_i\}, \{\vec{R}_I\}) = \psi_e(\{\vec{r}_i\}, \{\vec{R}_I\})\psi_{ion}(\{\vec{R}_I\}), \quad (2.2.1)$$

Here, $\psi_e(\{\vec{r}_i\}, \{\vec{R}_I\})$ is the electronic wavefunction and $\psi_{ion}(\{\vec{R}_I\})$ the ionic wavefunction. The coordinates of ions $\{\vec{R}_I\}$ are parameters of electronic wavefunction. In Eq. 2.2.1 it is assumed that electrons move in the stationary potential created by the nuclei. The electronic wavefunction $\psi_e(\{\vec{r}_i\}, \{\vec{R}_I\})$ satisfies the time-independent Schrödinger equation:

$$H_e\psi_e(\{\vec{r}_i\}, \{\vec{R}_I\}) = E_e\psi_e(\{\vec{r}_i\}, \{\vec{R}_I\}). \quad (2.2.2)$$

where the electronic Hamiltonian is

$$H_e = \sum_i^{N_e} \left[-\frac{1}{2} \nabla_i^2 \right] - \sum_i^{N_e} \sum_I^{N_I} \left[\frac{Z_I}{|\vec{r}_i - \vec{R}_I|} \right] + \frac{1}{2} \sum_i^{N_e} \sum_{i'}^{N_e} \left[\frac{1}{|\vec{r}_i - \vec{r}_{i'}|} \right]. \quad (2.2.3)$$

Here the electronic energy E_e is a function of ionic positions \vec{R}_I , namely $E_e = E_e(\{\vec{R}_I\})$.

Since ionic motion is much slower than electronic motion, the effect exerted by electrons on ions can be described by an effective potential $\langle E_e(\{\vec{R}_I\}) \rangle$. The total effect of electronic interaction on ions can be treated as a part of the electrostatic potential of the ions. Therefore one ion moves in a potential field created by the other ions and all electrons. The ionic Hamiltonian thus has the following form

$$H_{ion} = \sum_I^{N_I} \left[-\frac{1}{2M_I} \nabla_I^2 \right] + \frac{1}{2} \sum_I^{N_I} \sum_{I'}^{N_I} \left[\frac{Z_I Z_{I'}}{|\vec{R}_I - \vec{R}_{I'}|} \right] + \langle E_e(\{\vec{R}_I\}) \rangle. \quad (2.2.4)$$

In Born-Oppenheimer approximation energy contributions of two orders of magnitude of electronic energy ($\sqrt{m_e/M_I} \approx 10^{-2}$) are ignored, which are much smaller than the distances between electronic energy levels [51]. Although the approximation gives solutions that are exact enough in most cases, it can be invalid when the motion of ions and electrons may not be decoupled and thus the separation of electronic and ionic wavefunction is inappropriate (e.g., at high temperature that is close to the electronic Fermi temperature, the kinetic energy of the nuclei is important when compared with that of electrons). Such exceptional cases are not considered in the scope of this thesis.

2.3 The Electronic Problem

Born-Oppenheimer approximation allows us to divide the total Hamiltonian of a many-body system into electronic Hamiltonian and nucleus Hamiltonian. The two part of Hamiltonians can be treated separately. The key issue for studying and analyzing the structure of matter is to find the eigenvalues of the electronic Hamiltonian. However the electronic problem is still not easy to tackle.

The electronic Hamiltonian (see Eq. 2.2.3) embraces three terms: the kinetic energy of electrons, the Coulomb interaction between electrons and nuclei, and the Coulomb interaction between electrons. The first two terms can be separated and attributed to a single electron, but the two-body Coulomb force between electrons cannot. Therefore the many-electron Hamiltonian cannot be simplified into a single-electron Hamiltonian, and thus the wavefunction of a many-electron system cannot be the product of the wavefunctions of the individual electrons. This is the main difficulty in solving the electronic Schrödinger equation, which is so-called the many-body problem.

2.4 Density Functional Theory

In this section a method to solve the electronic Hamiltonian will be introduced. The method can transform many-electron Schrödinger equation into a single-electron equation, which can be solved self-consistently.

Density functional theory constructs the Hamiltonian of a system in question by using the electronic density $n(\vec{r})$ instead of the wavefunction $\Psi(\{\vec{r}_i\})$. Electronic density $n(\vec{r})$ is a function of space coordinates $\vec{r} = (x, y, z)$. That means, no matter how many particles

there are in a system, the number of the space coordinates in DFT is always 3. This greatly reduces the number of the space variables when compared with the many-body wavefunction, where the space coordinates are $3N$, N is the number of particles. The framework of DFT was firstly developed by Hohenberg and Kohn in 1964 [46], and further completed by Kohn and Sham [47]. J. A. Pople developed computational methods for the theory, therefore he shared the 1998 Nobel Prize in Chemistry with Kohn.

2.4.1 The Hohenberg-Kohn Theorems

The two Hohenberg-Kohn theorems [46] connect the electronic density of a system and the ground state energy of the system.

For convenience of the description of the theorems, we first transform the electronic Hamiltonian represented in $3N$ space variables $\{\vec{r}_i\}$ into \vec{r} . The Hamiltonian of electrons (Eq. 2.2.3) can be reformulated as (the influence of ions on electrons is treated as an effective potential $v(\vec{r})$),

$$H_e(\vec{r}) = T_e(\vec{r}) + U_{ee}(n(\vec{r})) + V(n(\vec{r})) = F_{HK}(\vec{r}) + V(n(\vec{r})) \quad (2.4.1)$$

where

$$F_{HK} = T_e + U_{ee}, \quad (2.4.2)$$

F_{HK} is the combination of the kinetic energy and Coulomb interaction of electrons. It is independent on the electronic number and any external potential of a specific system.

$$T_e(\vec{r}) = \frac{1}{2} \int \nabla \Psi^*(\vec{r}) \nabla \Psi(\vec{r}) d\vec{r}, \quad (2.4.3)$$

$$\begin{aligned} U_{ee}(n(\vec{r})) &= \frac{1}{2} \int \Psi^*(\{\vec{r}_i\}) \sum_i \sum_{i' \neq i} \frac{1}{|\vec{r}_i - \vec{r}_{i'}|} \Psi(\{\vec{r}_i\}) d\{\vec{r}_i\} \\ &= \frac{1}{2} \int \sum_i \sum_{i' \neq i} \frac{1}{|\vec{r}_i - \vec{r}_{i'}|} n(\{\vec{r}_i\}) d\{\vec{r}_i\} \\ &= \frac{1}{2} \int \int g(\vec{r}, \vec{r}') \frac{1}{|\vec{r} - \vec{r}'|} n(\vec{r}) n(\vec{r}') d\vec{r} d\vec{r}' \end{aligned} \quad (2.4.4)$$

$$V(n(\vec{r})) = \int v(\vec{r}) \Psi^*(\vec{r}) \Psi(\vec{r}) d\vec{r} = \int v(\vec{r}) n(\vec{r}) d\vec{r}. \quad (2.4.5)$$

The coordinate transform of kinetic energy $T_e(\vec{r})$ and ion-electron interaction $V(\vec{r})$ is straightforward. However the transform of electron-electron interaction requires a pair correlation function $g(\vec{r}, \vec{r}')$, which describes the exchange and correlation effects. This will be discussed in detail in this section later.

Theorem 1 : In a system consisting of identical fermions (neglecting spin of electrons), the ground state energy is a universal functional of the electronic density.

Theorem 2 : The total energy $E[n(\vec{r})]$ of a certain electronic density is always greater or equal to the true ground state energy E_0 .

The first theorem tells us that the energy of any electronic system is a unique functional of the electronic density $n(\vec{r})$. As the electron-electron interaction and electron-ion interaction are explicitly dependent on the electronic density $n(\vec{r})$, it is straightforward to prove that they are the functional of $n(\vec{r})$. However, some mathematical tricks are necessary to prove the unique dependence of kinetic energy T_e on electronic density. The details can be found in the famous paper of Hohenberg and Kohn [46].

The second theorem is actually the variational principle in DFT. According to the second theorem the following relation for a system holds:

$$H_e[n_{try}(\vec{r})] \geq E_0(n_0(\vec{r})) \quad (2.4.6)$$

where $n_{try}(\vec{r})$ and $n_0(\vec{r})$ represent a trial electronic density and the electronic density of ground state, respectively, which are subjective to the electron conservation $\int n(\vec{r})d\vec{r} = N_e$. Or more exactly,

$$F_{HK}[n_{try}(\vec{r})] + \int v(\vec{r})n_{try}(\vec{r})d\vec{r} \geq E[n_0(\vec{r})] \quad (2.4.7)$$

where E_0 is the total energy of the system at its correct ground state. The equal sign is obtained when $n_{try}(\vec{r}) = n_0(\vec{r})$.

In principle, using electronic density as the basic variable does not cause any inconvenience, since electron density and wavefunction can be transformed from each other in DFT: when Ψ is known, $n(\vec{r}) = |\Psi|^2$; when $n(\vec{r})$ is known, we can firstly construct $H[n(\vec{r})]$, and then solve the Schrödinger equation to find out the corresponding wavefunction Ψ .

Within the framework defined by the two theorems, the Hamiltonian of electrons is a functional of only the electronic density of the ground state and the electronic energy in an external potential could be numerically computed only if the functional $F_{HK}[n(\vec{r})]$ would be known. Unfortunately, the exact form of $F_{HK}[n(\vec{r})]$ is unknown. An approximation to $F_{HK}[n(\vec{r})]$ that can obtain rather accurate electronic density and the ground state energy has been introduced by Kohn and Sham.

2.4.2 The Kohn-Sham Equations

Hohenberg-Kohn theorems prove the ground state energy is a functional of the correct electronic density. But the theorems do not answer the question how the correct electronic density can be found out, which was solved by Kohn and Sham [47] in 1965. According to the Hohenberg-Kohn theorem, the ground state energy $E[n(\vec{r})]$ of an interacting inhomogeneous electron gas in a potential $v(\vec{r})$ can be written as

$$\begin{aligned}
 E[n(\vec{r})] &= T_e[n(\vec{r})] + V[n(\vec{r})] + U_{ee}[n(\vec{r})] \\
 &= T_e[n(\vec{r})] + V[n(\vec{r})] + \frac{1}{2} \int \frac{n(\vec{r})n(\vec{r}')}{|\vec{r} - \vec{r}'|} d\vec{r} d\vec{r}' + \frac{1}{2} \int (g(\vec{r}, \vec{r}') - 1) \frac{n(\vec{r})n(\vec{r}')}{|\vec{r} - \vec{r}'|} d\vec{r} d\vec{r}' \\
 &= T_e[n(\vec{r})] + V[n(\vec{r})] + J[n(\vec{r})] + E_{xc}[n(\vec{r})].
 \end{aligned} \tag{2.4.8}$$

where

$$J[n(\vec{r})] = \frac{1}{2} \int \int \frac{n(\vec{r})n(\vec{r}')}{|\vec{r} - \vec{r}'|} d\vec{r} d\vec{r}', \tag{2.4.9}$$

$J[n(\vec{r})]$ is the Hartree term that corresponds to the classical electrostatic repulsion.

$$E_{xc}[n(\vec{r})] = \frac{1}{2} \int \int (g(\vec{r}, \vec{r}') - 1) \frac{n(\vec{r})n(\vec{r}')}{|\vec{r} - \vec{r}'|} d\vec{r} d\vec{r}', \tag{2.4.10}$$

E_{xc} is the exchange and correlation energy of a system consisting of interacting particles. The density and kinetic energy of such a system can be written as the functional of single-particle wavefunctions $\psi_i(\vec{r})$:

$$n(\vec{r}) = \sum_i^{N_{occ}} \langle \psi_i(\vec{r}) | \psi_i(\vec{r}) \rangle, \tag{2.4.11}$$

$$T_e[n(\vec{r})] = \sum_i^{N_{occ}} \langle \psi_i(\vec{r}) | -\frac{1}{2} \nabla^2 | \psi_i(\vec{r}) \rangle. \tag{2.4.12}$$

assuming that the orbitals are orthonormal, namely $\langle \psi_i | \psi_j \rangle = \delta_{ij}$. N_{occ} is the number of the occupied states.

According to variation principle, the minimal value of $E[n(\vec{r})]$ (Eq. 2.4.8) can be obtained when the following requirements are fulfilled:

$$[-\frac{1}{2} \nabla^2 + v_{eff}] \psi_i = \sum_j^{N_{occ}} \lambda_{ij} \psi_j. \tag{2.4.13}$$

where λ_{ij} are the Lagrange multipliers due to the orthonormalization constrain, and v_{eff} is the single-electron effective potential,

$$v_{eff}(\vec{r}) = v(\vec{r}) + \frac{\delta J[n(\vec{r})]}{\delta n(\vec{r})} + v_{xc}. \tag{2.4.14}$$

Here, $v_{xc}(\vec{r})$ is the exchange-correlation potential given by the functional derivative of the exchange-correlation energy $E_{xc}[n(\vec{r})]$:

$$v_{xc}(\vec{r}) = \frac{\delta E_{xc}[n(\vec{r})]}{\delta n(\vec{r})}. \tag{2.4.15}$$

The matrix $\{\lambda_{ij}\}$ is Hermitian and thus can be diagonalized by a unitary transformation of the orbitals, and the eigenvalues of the matrix are $\{\epsilon_i\}$. Therefore a more simple expression of Eq. 2.4.13 is

$$[-\frac{1}{2}\nabla^2 + v_{eff}]\psi_i = \epsilon_i\psi_i. \quad (2.4.16)$$

Eqs. 2.4.11-2.4.12 and 2.4.14-2.4.16 are the Kohn-Sham (KS) equations. The solutions of KS equations are usually proceeded in two steps. First, start with a trial electronic density $n_{try}(r)$ (typically a linear combination of electronic densities of independent atoms) and calculate the exchange-correlation E_{xc} and the effective potentials v_{eff} using Eqs. 2.4.14 and 2.4.15. Second, solve the single-particle Schrödinger equation Eq. 2.4.16 in order to obtain new single-particle orbitals. The newly obtained electronic density mixed with the old electronic density is again used as the input electronic density for the next step. These two steps are iteratively repeated until the difference between the input density and output density is smaller than a certain threshold value.

The KS equations would supply an exact density and energy of the ground state if the exchange-correlation functional E_{xc} is known precisely. However, no analytical form has yet been identified, therefore a number of methods to evaluate E_{xc} have been developed, which will be introduced in the next section.

2.4.3 Approximations to E_{xc} : Climbing Jacob's Ladder

The many-body effect of electrons in Schrödinger equation is inherited in the exchange-correlation energy term E_{xc} (Eq. 2.4.17), which can be rewritten as

$$E_{xc}[n(\vec{r})] = \int n(\vec{r})v_{xc}(\vec{r})d\vec{r}, \quad (2.4.17)$$

where the exchange-correlation potential

$$v_{xc}(\vec{r}) = \int \frac{1}{2}(g(\vec{r}, \vec{r}') - 1) \frac{n(\vec{r}')}{|\vec{r} - \vec{r}'|} d\vec{r}' \quad (2.4.18)$$

Approximations to the exchange-correlation potential v_{xc} are necessary due to the unknown pair correlation function $g(\vec{r}, \vec{r}')$.

The simplest approach to find an approximation to v_{xc} is the local density approximation (LDA) [47, 52, 53], which employs the homogeneous electron gas of uniform electron distribution $n(\vec{r})$ to describe v_{xc} . That is,

$$v_{xc}^{\text{LDA}}(\vec{r}) = \epsilon_{xc}^{\text{hom}}[n(\vec{r})]. \quad (2.4.19)$$

Despite of its rather rough approximation, the LDA has been very successful in a wide variety of applications. But the approximation is not accurate enough for many chemical purposes, e.g., it usually overestimates inter-atomic interactions and consequently underestimates the lattice constants. Among others these deficiencies are known: (i)

Table 2.4.1:

Jacob's ladder of exchange and correlation approximations.

Ladder	Approximation	added ingredient
Fifth Rung	RPA-like [56]	exact correlation
Fourth Rung	hyper-GGA [57, 58]	exact exchange
Third Rung	meta-GGA [55]	positive kinetic energy density
Second Rung	GGA [54]	gradient of electronic density
First Rung	LDA [47, 52, 53]	local density

the description of alkali metals, (ii) the incorrectly predicted ground state of Fe, and (iii) the description of systems with very localized electrons. In order to fix these deficiencies the generalized gradient approximation (GGA) [54] that takes not only the local value of density $n(\vec{r})$ but also its gradient $\nabla n(\vec{r})$ into account have been developed, namely,

$$v_{xc}^{\text{GGA}}(\vec{r}) = \epsilon_{xc}^{\text{GGA}}[n(\vec{r}), \nabla n(\vec{r})]. \quad (2.4.20)$$

Typically the GGA is more accurate than the LDA, but this is not always the case. To further increase the accuracy, more ingredients are necessary to be added to GGA, e.g. in case of meta-GGA [55], the second order of density gradient $\nabla^2 n(\vec{r})$ is included in the exchange-correlation functional. The improvement procedure of exchange-correlation functionals is analogue to climbing a ladder. The higher accuracy one needs, the more rungs is to be climbed, which means the more computational cost and time. Such a ladder is known as Jacob's ladder with five rungs. (Table 2.4.1). The general characteristic of Jacob's ladder is: the first three rungs are empirical-parameter free; from the fourth rung empirical parameters are introduced. For more detail about the methods applied in each rung the readers are referred to the corresponding references.

2.5 Bloch Theorem

In an infinite system with periodic potential (e.g. crystal) where $V(\vec{r} + \vec{T}) = V(\vec{r})$, it is necessary to solve its Schrödinger equation not in the whole space of the system, but only in one minimal period of the space. The scheme, described by Bloch theorem, greatly simplifies the numerical solving procedure in question.

If the translation operator of one period of the system is denoted by T , λ is its eigenvalue, then

$$T\psi(\vec{r}) = \psi(\vec{r} + \vec{T}) = \lambda\psi(\vec{r}) \quad (2.5.1)$$

For a finite system that is \vec{N} ($=(N_x, N_y, N_z)$) times of period \vec{T} ($=(T_x, T_y, T_z)$), the periodic operator can be applied for each direction by the corresponding times of periods, therefore we have the following relation,

$$T^{\vec{N}}\psi(\vec{r}) = \lambda^{\vec{N}}\psi(\vec{r}) \quad (2.5.2)$$

It is very straightforward to prove that the Hamiltonian H of a periodic system is commutative with translation operator T , which means the eigenvalue and associated eigenfunction (or wavefunction) of T also apply to the Schrödinger equation of the system,

$$H\psi(\vec{r}) = E\psi(\vec{r}) \quad (2.5.3)$$

Therefore,

$$T^{\vec{N}} H\psi(\vec{r}) = HT^{\vec{N}}\psi(\vec{r}) = H(\lambda^{\vec{N}}\psi(\vec{r})) = E(\lambda^{\vec{N}}\psi(\vec{r})) \quad (2.5.4)$$

which means, if $\psi(\vec{r})$ is a solution to Schrödinger equation, then $\lambda^{\vec{N}}\psi(\vec{r})$ is its solution as well. Suppose both wavefunctions are normalized, then we can calculate the total energy of the system,

$$E = \langle \lambda^{\vec{N}}\psi | H | \lambda^{\vec{N}}\psi \rangle = |\lambda^{\vec{N}}|^2 \langle \psi | H | \psi \rangle = \langle \psi | H | \psi \rangle \quad (2.5.5)$$

Therefore,

$$|\lambda^{\vec{N}}|^2 = 1 \quad (2.5.6)$$

So the eigenvalue of the translation operator $\lambda^{\vec{N}}$ is just a phase factor of the wavefunction. That is, λ changes only the phase of wavefunction, not the wave amplitude. Its specific expression is,

$$\lambda = \exp(-i2\pi/\vec{N}) \quad (2.5.7)$$

The minimal periodic zone in one dimensional case is defined by $[-\pi/N_x, \pi/N_x]$ (or $[0, 2\pi/N_x]$), namely the first Brillouin zone. If the wavefunction in the first Brillouin zone is computed, the wavefunctions in the second, third and higher orders of Brillouin zone can be easily obtained by multiplying the wavefunction with the corresponding phase factor.

2.6 Introduction of Molecular Statics

Unlike electronic structure method, in molecular statics (or dynamics) method a molecule or an atom is coarse-grained as one object whose motion is dominated by a force field. The force field experienced by the object (e.g. one atom or molecular) and the velocity of the object is connected by Newton's second law. Since the motion of electrons is not considered in molecular statics this method is more efficient in computation and therefore can deal with problems with much larger sizes than DFT (e.g. several millions of atoms).

There are several different approaches to compute the force field employed molecular statics (or dynamics). If the force field is directly calculated by DFT approach using Hellmann-Feymann equation [43], the method is usually referred to ab-initio molecular dynamics [43, 44]. If the force field is obtained by an empirical potential of which the parameters are fitted to experimental data or DFT results, the method is called classical molecular dynamics [59]. Compared with ab-initio molecular dynamics method (limited

to several hundreds of atoms), the classic molecular statics/dynamics method can deal with larger size problem with satisfied lower accuracy.

Unlike electronic structure methods, atoms are considered as point objects in classical molecular statics (or alternatively dynamic) simulations. These coarse-grained objects interact by inter-atomic potentials, so-called force fields, and their motion is determined by Newton's laws. Since the electrons are not considered, simulations involving millions of atoms are computationally accessible. The inter-atomic potentials are, on the other hand, rather severe approximations to real inter-atomic interactions dominated by electrons governed by quantum-mechanics, and, consequently, the quality of force-fields must be carefully tested. In order to provide a description that would be as accurate as possible, parameters of force fields are fitted to either experimental data or results of quantum-mechanical calculations. Next to reference values, another very important aspect is an actual mathematical structure (type) of the force field. The simplest ones are pair-potentials (such as Lennard-Jones) but angular and many-body terms are often necessary to be added.

In order to overcome shortcomings of pair potentials, embedded atom method (EAM) potentials were proposed by Daw and Baskes [60, 61]. The EAM potentials consist of a pair-wise term and many-body terms that are expressed as functions of the electronic density n_i at each atom center:

$$V = \sum_{i>j} \Phi(r_{ij}) + \sum_i^N F(n_i) \quad (2.6.1)$$

where, $\Phi(r_{ij})$ is the pair potential and $F(n_i)$ represents the energy required for embedding an atom at a site i with electronic density n_i . The specific form of $F(n_i)$ is different for different EAM potentials. For example, in case of Finnis and Sinclair EAM potentials [62], $F_i = -\sqrt{n_i}$. The type of functional dependence (originally developed by Sun [24]) has been also employed in this thesis in the part about the Peierls-Nabarro model. The electronic density in the potential is computed by the superposition of electronic densities of surrounding atoms:

$$n_i = \sum_i^N \rho_j^{atom}(r_{ij}). \quad (2.6.2)$$

The initial input densities n_i are determined by solving the corresponding Hartree-Fock equation.

Chapter 3

Binary Mg Alloys

3.1 Introduction

Sandlöbes *et al.* observed decreased I_1 stacking fault energy and enhanced ductility in Mg-3wt%-Y alloy in experiment [6, 37]. Based on their experimental observations we proposed that there is a connection between these two physical quantities. In this chapter we firstly checked the decreased I_1 stacking fault energy in the framework of density functional theory. And then further evaluate the "connection". We believe if the "connection" that decreased I_1 stacking fault energy indicates improved ductility is reliable, it should be possible to predict more solutes which can also ductilize magnesium like yttrium.

3.2 Computational Methodology

In this section we firstly introduce the model that is employed in our calculation, which can reduce the computational cost. Following this we give more details on the important input parameters and then equation of state.

3.2.1 ANNNI Model for E_{SF1}

The axial next-nearest neighbor Ising (ANNNI) model was named by Fisher and Selke [63] in 1980. Its three-dimensional variant was already introduced by Elliott in 1961 [64]. The ANNNI model may be considered as a prototype to describe real systems with discrete Ising-type distributions of atomic planes and effectively short-range competing interactions where entropic effects are crucial in stabilizing a multitude of distinct spatially modulated patterns [65].

In lattice models, each lattice site, k , is occupied by a variable or spin, S_k . S_k can be a 1-dimensional vector (a discrete variable) or n-dimensional vector with scale length equal to 1. S_k is a discrete variable, $S_k = \pm 1$. Normally, the spins are assumed to interact through pairwise couplings of the form $-J_{kl}S_kS_l$. Here J_{kl} are interaction energy between spins S_k and S_l .

The construction of the Hamiltonian of such a spin system is illustrated by a simple example, the one-dimensional ANNNI model (see Figure 3.2.1). Assuming an Ising chain of equidistant spins with interaction energies J_1 , between nearest neighbors (NN) and J_2 , between next-nearest neighbors (NNN), its Hamiltonian can be written as,

$$H = -J_1 \sum_k S_k S_{k+1} + J_2 \sum_k S_k S_{k+2} + \dots \quad (3.2.1)$$

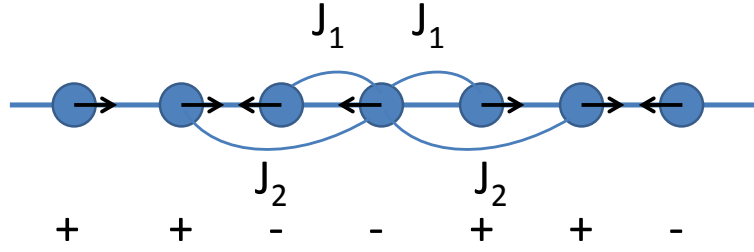


Figure 3.2.1:

Schematic view of the one dimensional ANNNI model consisting of an atom chain [65].

In the present study S_k represents different states of layers for A, B and C. Similarly to a 1-dimensional chain model, the total energy of a crystal system supplied by ANNNI model is

$$E = - \sum_n \sum_k J_n S_k S_{k+n}. \quad (3.2.2)$$

Apply Eq. 3.2.2 (consider only cases of $n \leq 2$) to different stacking of A, B and C, e.g. face-centered cubic(fcc), hcp, double hcp (dhcp) and I_1 stacking fault respectively, the corresponding energy per layer of N -layer system is obtained.

fcc stacking $(ABC)^{N/3}$:

$$E_{\text{fcc}} = J_0 - J_1 - J_2 - O(J_2) \quad (3.2.3)$$

hcp stacking $(AB)^{N/2}$:

$$E_{\text{hcp}} = J_0 + J_1 - J_2 + O(J_2) \quad (3.2.4)$$

dhcp stacking $(ABAC)^{N/4}$:

$$E_{\text{dhcp}} = J_0 + J_2 - O(J_2) \quad (3.2.5)$$

I_1 stacking fault $(AB)^m ABCB(CB)^n$ ($N = m + 4 + n$) :

$$E_{I_1} = J_0 + \frac{N-2}{N} J_1 - \frac{N-4}{N} J_2 + O(J_2). \quad (3.2.6)$$

Therefore the I_1 stacking fault energy (I_1 SFE) that uses the total energy of perfect hcp as the reference can be formulated as and calculated by,

$$E_{SF1} = \lim_{N \rightarrow \infty} N(E_{I_1} - E_{\text{hcp}}) = -2J_1 + 4J_2 + O(J_2). \quad (3.2.7)$$

Truncating the series behind the second-order term (the 2nd order approximation), the expressions for first two interaction parameters can be obtained from Eq. 3.2.3-3.2.5, namely,

$$J_1 = \frac{1}{2}(E_{\text{hcp}} - E_{\text{fcc}}), J_2 = \frac{1}{2}(E_{\text{dhcp}} - E_{\text{fcc}} - J_1), \quad (3.2.8)$$

Inserting Eq. 3.2.8 into Eq. 3.2.7,

$$E_{\text{SF1}} \approx -2J_1 + 4J_2 = 2(E_{\text{dhcp}} - E_{\text{hcp}}), \quad (3.2.9)$$

This means the stacking fault energy depends only on the energy difference between the hcp and dhcp crystallographic structures. As an intensive property, I₁SFE is independent on the stacking fault area A . Therefore, the I₁SFE is computed by

$$\gamma^{\text{SF1}} = \frac{2(E_{\text{dhcp}} - E_{\text{hcp}})}{A} \quad (3.2.10)$$

By employing the ANNNI model, DFT calculations of the stacking fault energy are greatly simplified. The stacking fault energy can be calculated directly from the total energies of magnesium (or alloys) with hcp and dhcp structures. Otherwise, a rather large supercell is needed in order to construct the stacking fault, which is a more expensive calculation compared to the calculations of total energy of hcp or dhcp structure. This model has been successfully applied to different metals, such as fcc iron [66]. For hcp Ti and hcp Re Hu *et al.* [67] performed full-potential augmented plane-wave (FP APW) calculations using the WIEN2K code [68] and demonstrated that the I₁SFEs from the ANNNI model agree with those from explicit supercell calculations.

3.2.2 Computational Parameters

The total energies of hcp, E_{hcp} , and dhcp, E_{dhcp} , of the respective materials systems are defined only by the atomic coordinates and the chemical nature of the atoms involved. With the atomic coordinates as the most important input information and other parameters, of which the values are able to be determined through convergent testing, the total energy of a periodic system can be obtained by DFT. The DFT calculations are performed in the VASP (Vienna Ab-initio Simulation Package) [69, 70, 71] using the projector augmented wave (PAW) method and the generalized gradient approximation (GGA), with the electron exchange-correlation described by the Perdew-Burke-Ernzerhof parameterization [72]. The cut-off energy is 350 eV for most of the calculation. A Gamma point scheme is employed for sampling Brillouin zone with safe k-mesh density. The total energy is convergent within 10⁻⁷ eV.

3.2.3 Murnaghan Equation of State

The Murnaghan equation of state [73, 74] describes the relation between the volume per unit cell, V , and the total energy $E(V)$ of the system. The relationship among them is

$$E(V) = E_0 + BV_0 \left\{ \frac{1}{B'(B' - 1)} \left(\frac{V}{V_0} \right)^{1-B'} + \frac{1}{B'} \frac{V}{V_0} - \frac{1}{B' - 1} \right\} \quad (3.2.11)$$

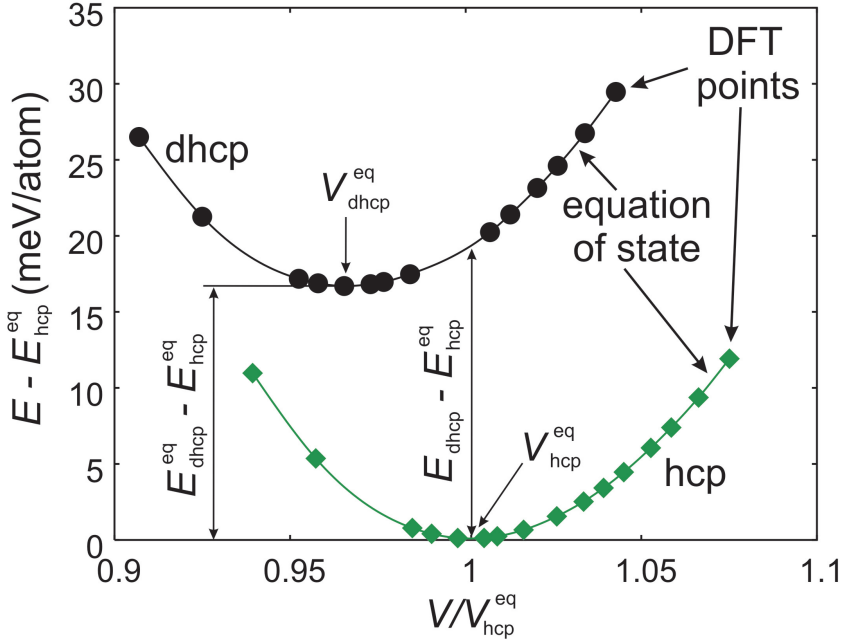


Figure 3.2.2:

Schematic figure of the energy-volume curves calculated for both hcp and dhcp phases. The solid lines are fitted to the *ab initio* results using the Murnaghan equation of state. The schematic sketch also illustrates the meaning of the various energy-volume-related parameters used in the ANNNI model.

Here, V_0 is the ground-state volume which minimizes the function, E_0 is the corresponding energy, B the bulk modulus and B' is its pressure derivative at the ground state. The parameters in the equation can be fitted to a series of (V, E) data points which are computed using first-principles method. Once these parameters are determined, the energy at any point of volume can be calculated.

As seen in Figure 3.2.2 depicting the energy-volume curves for both hcp and dhcp phases, the equivalent volumes of the hcp and dhcp phases are different, which means the cross section area of the I_1 stacking fault of the two phases is also different. This could be a problem when employing Eq. 3.2.10. To be mathematically strict, we define I_1 SFE at the equilibrium volume of hcp phase in this thesis.

Since the Murnaghan equation gives the relationship between the total energy and crystal volume, the total energy of dhcp phases at the equilibrium volume of hcp phases can be calculated. Therefore a more exact definition of I_1 SFE is the following:

$$\gamma^{SF1} = \frac{2(E_{dhcp} - E_{hcp})}{A} = \frac{2(E_{dhcp}(V_{hcp}^{eq}) - E_{hcp}^{eq})}{A_{hcp}^{eq}} \quad (3.2.12)$$

Actually, the I_1 SFE of Mg alloys is not sensitive to the change of volume.

Table 3.3.1:

Comparison of experimental data and data from theoretical calculation

Element	a (Å)	c/a	B (GPa)	data source
Mg	3.2094	1.6236	35.55	Experiment [75]
	3.1886	1.6261	36.33	this work
Y	3.6482	1.5711	41.43	Experiment [75]
	3.6466	1.5509	41.08	this work

3.3 Results and Discussion

3.3.1 Mg-Y Alloys

Mg-Y alloys are the model materials system for binary Mg alloys; for other binary Mg alloys the computational procedure of Mg-Y is replicated.

In the ANNNI model, the computation of l_1 stacking fault energy needs only the ground state total energies of Mg, Y and Mg-Y alloys in perfect hcp and double hcp structure respectively. The accuracy of computed stacking fault energy depends on the reliability of applied PBE pseudopotentials for Mg and Y which are firstly checked in any first-principles calculation procedure. The checking method is to compare the calculated bulk properties (lattice parameters and bulk modulus) with experimental values. If they are consistent in a certain acceptable error, then the potential is taken as of good quality and reliable. Usually there are more than one pseudopotentials generated for special chemical application purpose. We employed the one that has a closer bulk properties with experiment. For example, there are two versions of pseudopotentials for Mg, one with 2 3s valence electrons and the other with 6 more 2p valence electrons (the left electrons are frozen). Both potentials have very consistent bulk properties and are reliable. In present study the 2-electron one is employed. For yttrium pseudopotential, there is only one version with 11 valence electrons (4s4p5s4d) from outmost electron shells, which predicts bulk properties in good agreement with experimental values. The benchmark of the pseudopotentials are shown in Table 3.3.1. The optimized computational parameters are 16-atomic supercells for both pure Mg and pure Y, the cut-off energy 350 eV and the k-point mesh $(k_x, k_y, k_z) = (20, 20, 12)$.

Before we extend our calculations to Mg-Y alloys, the non-equivalent sites for one solute in a supercell is tested. It is clear that there are two different kinds of sites in the dhcp structure due to symmetry of the crystallographic structure. For hcp structure, all sites are equivalent (see Chapter 1.2.1 and Figure 1.2.1). More specifically, layers B and C in dhcp structure are equivalent, and layer A is different from B and C, which is proved by the first-principles calculations (see Table 3.3.2). The total energy difference between them is 3meV, which is not negligible. The bulk properties of the two cases are also slightly different. Since B or C are energetically more favorable for substituted solutes, solute should be put in B or C layers of magnesium in a dhcp supercell at 0 K. No matter

3.3. Results and Discussion

Table 3.3.2:
Calculated results for Mg₁₅Y with Y-atom in different positions

Position in Mg ₁₅ Y	<i>a</i> (Å)	<i>c/a</i>	<i>B</i> (GPa)	<i>E</i> ₀ per Atom (eV)
hcp-A/B	3.2550	1.5832	36.51	-1.857
dhcp-A	3.2550	3.1755	36.10	-1.852
dhcp-B/C	3.2506	3.1784	36.35	-1.855

what lattice parameters are, bulk moduli and total energies of positions A and B in hcp structures are identical, which again proves that all sites in the structure are equivalent. The calculation parameters provide satisfactory description of these alloys and will be used below also for other stoichiometries. In order to perform calculations on equal footing for supercells with different number of atoms, the k-point mesh is properly scaled. The computational parameters used for Mg-Y alloys with different Y-concentration are then listed in Table 3.3.3.

Table 3.3.3:

Supercell geometries, supercell size, simulated stoichiometries, and the corresponding Monkhorst-Pack k-point meshes used in the DFT calculations of Mg-Y alloys.

Structure	hcp	dhcp	hcp	dhcp	hcp	dhcp
stoichiometry	Mg ₁₅ Y	Mg ₁₅ Y	Mg ₃₁ Y	Mg ₃₁ Y	Mg ₁₀₇ Y	Mg ₁₀₇ Y
at.% Y	6.25	6.25	3.125	3.125	0.926	0.926
supercell	2x2x2	2x2x1	2x2x4	2x2x2	3x3x6	3x3x3
No. of Atoms	16	16	32	32	108	108
k-point mesh	18x18x12	18x18x12	18x18x6	18x18x6	12x12x4	12x12x4

Table 3.3.4:

DFT calculated I₁ stacking fault energies γ_{SF1} in elemental Mg and Y, as well as Mg-Y alloys.

alloy	Mg	Mg ₁₀₇ Y	Mg ₃₁ Y	Mg ₁₅ Y	Y
at.% Y	0	0.926	3.125	6.25	100
γ_{SF1} (mJ/m ²)	20 ± 1	19 ± 1	14 ± 1	8 ± 1	23 ± 1

Table 3.3.4 shows the results of the DFT calculations, which are drawn in Figure 3.3.1. It is seen that the I₁ stacking fault energies γ_{SF1} in alloys decrease with increasing concentration of Y, even though the I₁ stacking fault energy in pure yttrium is higher than that in pure Mg. Up to the solubility limit, the γ_{SF1} energy reduces nearly linearly with Y-concentration. Among the three considered alloys, the stacking fault energy

of Mg_{15}Y is the lowest, namely about 8 mJ/m^2 , 12 mJ/m^2 lower than that of pure magnesium. The trend of γ_{SF1} -Y concentration curve is in qualitative agreement with the experimental data, but the absolute values are higher than experimental data presented in [6]. Since our calculation is performed at 0 K, while the experimental value is obtained at finite temperature, the difference is expected. Another possible reason is, the solutes in real materials may exist locally in cluster, while in our calculation the solutes are equally distributed in the matrix. The formation of local solute cluster in or near I_1 stacking fault strengthens the effective influence of yttrium, which induces a stronger reduction of stacking fault energy by the same amount of yttrium in experiment than in our simulation.

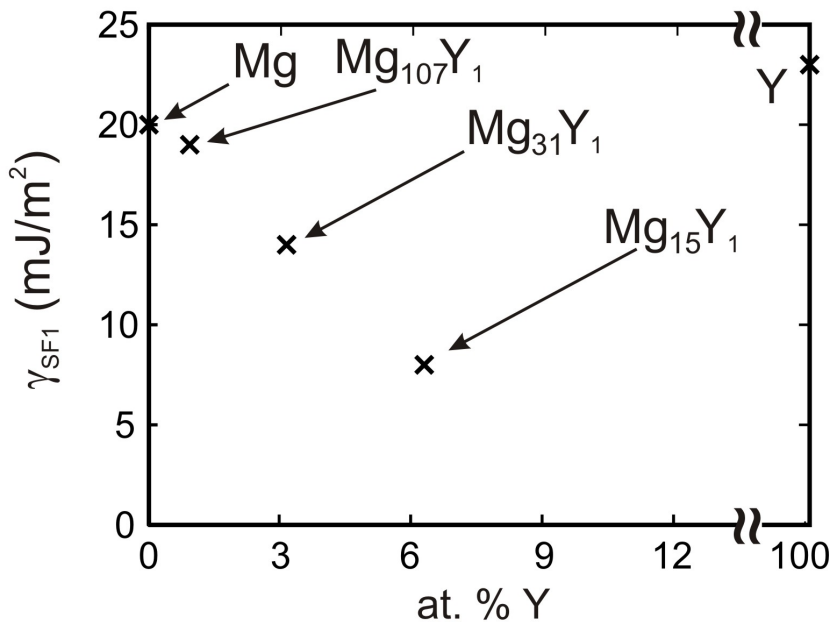


Figure 3.3.1:

Calculated compositional dependence of the I_1 stacking fault energy [37].

Figure 3.3.2 shows selected thermodynamic, structural and elastic parameters computed for Mg-Y alloys with both hcp and dhcp structures. Specifically, the energy difference between the dhcp and hcp structures, the ratio of lattice parameters c/a ($1/2c/a$ for dhcp), as well as the volumetric difference and bulk modulus difference between the two phases. With increasing Y-concentration, the cohesive energies of hcp and dhcp Mg_{15}Y approach gradually, which means hcp structure becomes more similar to dhcp from thermodynamics point of view. The c/a difference does not have obvious changes with concentration of yttrium, while the volumes of the two structures approach, which means the two phases become geometrically more similar. The bulk modulus difference becomes smaller, apart from a slightly increase at 3.125 at.%. From these data we can conclude that dhcp and hcp structures become more similar by adding more yttrium. The similarity makes the total energy differences between the two phases smaller which is a direct reason for reduced stacking fault energy in the ANNNI model.

3.3. Results and Discussion

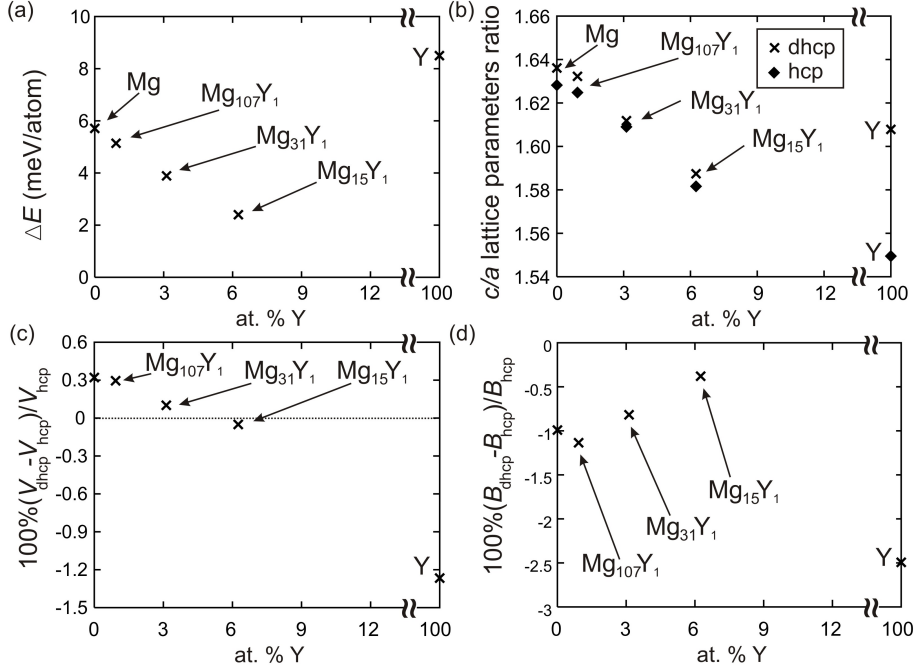
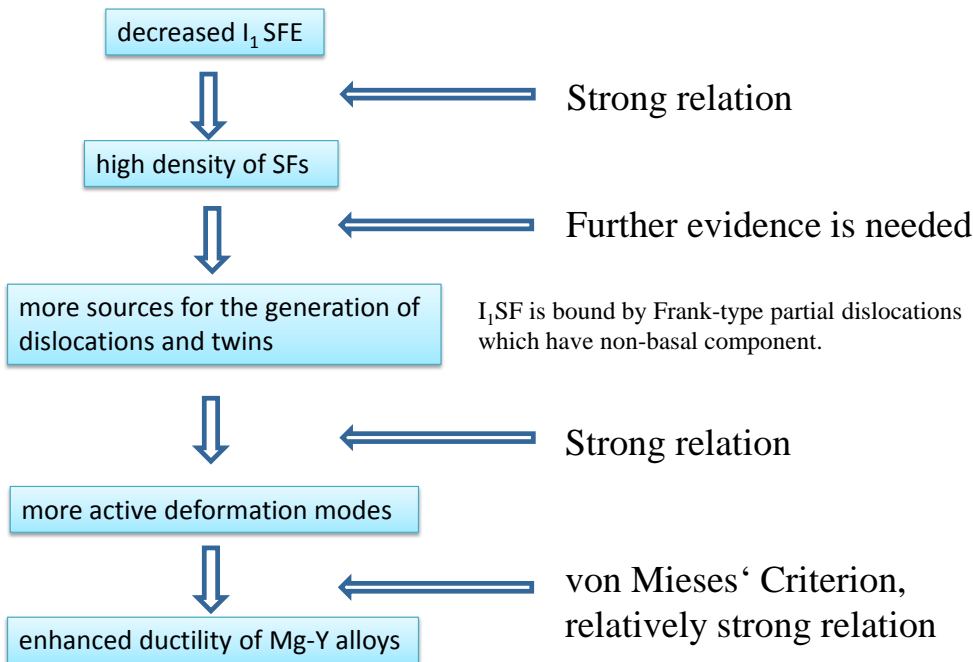


Figure 3.3.2:

Computed compositional trends of energy differences (a), the hcp and dhcp lattice parameter c/a ratios (b), and relative differences (in %) of volumes V (c) and bulk moduli B (d) between the hcp and dhcp phases [37].

We conclude that I_1 stacking fault energy decreases with increasing concentration of yttrium, and briefly discuss the reason of decrease. Based on these results we propose a connection between reduced I_1 stacking fault energy and enhanced ductility of Mg-Y alloys. The critical points are summarized and shown briefly in Figure 3.3.3. Both experimental and calculated I_1 stacking fault energies of Mg-Y alloys are lower than in pure Mg. The direct result of reduced I_1 stacking fault energy is the increased density of the stacking fault, which is validated by transmission electron microscopy (TEM) observation [37]. On another hand, under Electron Backscatter Diffraction (EBSD) measurement, the texture of Mg-Y alloys is less pronounced basal-type (characterized by a splitting of the basal poles around the transverse direction) than pure Mg [6], which means there are non-basal deformation modes activated. Among the non-basal deformation modes, non-basal dislocations are frequently observed under TEM. To connect both ends we suppose the I_1 stacking fault is the nucleation source for such non-basal dislocations. For more detail please refer to our joint publication with Sandlöbes [37]. The relative weak connection still needs fourth evidence. Very recently Agnew *et al.* discussed the possibility of I_1 SF being nucleation source of $1/3\langle 11-23 \rangle$ dislocation [76], and concluded the process is energetically conceivable in a wide range of I_1 SF geometries.

**Figure 3.3.3:**

The connection between decreased I_1 stacking fault energy and enhanced ductility of Mg-Y alloys.

3.3.2 Mg-RE Alloys

Mg-Y alloys are not economically suitable to be massively produced in industry because yttrium is expensive. Therefore in this section we continue our search for alternative solutes. The searching scope is limited to elements crystallizing in either hcp or dhcp structure at room temperature (see Table 3.3.5). The materials properties (e.g. I_1 SFE, bulk moduli) of Mg alloyed with these selected elements are calculated applying the same computational method as for Mg-Y. The rare earth elements were investigated in this section, and non-rare earth elements were studied in next section.

Table 3.3.5:
Chemical elements considered in this chapter as solutes for Mg

Group	Chemical elements	Structure
Rare Earth Elements	Y,Sc,Gd,Tb,Dy,Ho,Er,Tm,Lu	hcp
	Pr,Nd	dhcp
Non-Rare Earth Elements	Be,Ti,Co,Zr,Ru,Re,Os,Tl,Tc,Zn	hcp

When selecting the different solutes, our choice of hcp and dhcp elements is motivated by following reasons. First, in case of hcp elements, it is possible that the crystal structure matching that of pure Mg may help to enhance the solubility of these elements in Mg.

3.3. Results and Discussion

Second, solutes preferring the hexagonal closed-packing structure may have the tendency to locally stabilize the dhcp stacking sequence of the I_1 SF.

Among the hcp and dhcp elements, not all of them are considered as possible solutes as a few of them are excluded for rather pragmatic reasons. First, there is no pseudopotential file describing properties of elements like Am and Cm in the database of VASP. Therefore, alloys of Mg with such elements were not considered here. Second, radioactive elements (except Tc) were excluded due to their nature preventing their practical use. The calculation of Tc is just out of curiosity. The results of all other solutes are summarized below.

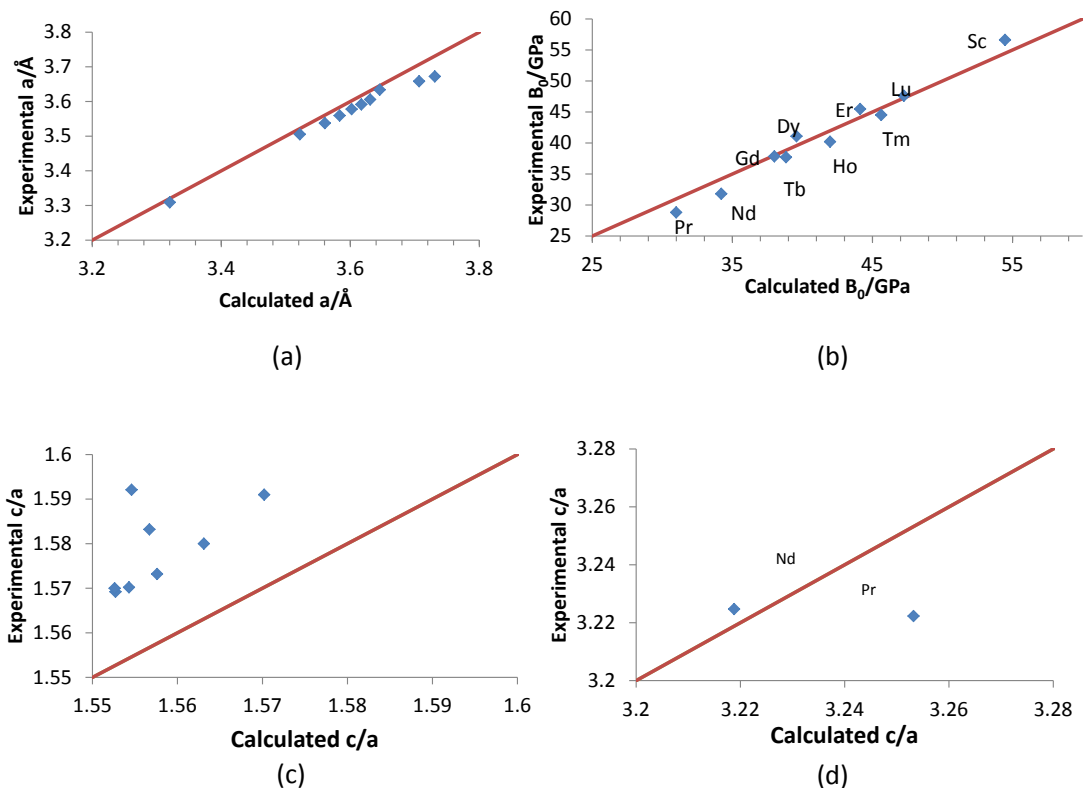
Using the computational parameters in Table 3.3.6, Mg-Pr, Mg-Nd, Mg-Gd, Mg-Dy, Mg-Tb, Mg-Ho, Mg-Er, Mg-Tm, Mg-Lu and Mg-Sc alloys were studied. Sc belongs to the IIIB group and the 4th period in the periodic table of elements but due to its similarities to RE elements, it is often considered as one of the RE element. For the ten RE elements, $Mg_{15}X$ supercell size is employed. Additionally, $Mg_{31}X$ is considered for X= Ho,Tm.

Table 3.3.6:

Supercell geometries, supercell size, simulated stoichiometries, and the corresponding Monkhorst-Pack k-point meshes used in the DFT calculations (rare earth elements)

Structure	hcp	dhcp	hcp	dhcp	hcp	dhcp
stoichiometry	Mg(X)	Mg(X)	$Mg_{31}X$	$Mg_{31}X$	$Mg_{15}X$	$Mg_{15}X$
at.% X	0(100)	0(100)	3.125	3.125	6.25	6.25
supercell	2x2x2	2x2x1	2x2x4	2x2x2	2x2x2	2x2x1
No. of Atoms	16	16	32	32	16	16
k-point mesh	10x10x6	10x10x6	10x10x3	10x10x3	10x10x6	10x10x6

In order to test PBE pseudopotentials of selected RE elements in the VASP database, the lattice constants a , c/a and the bulk moduli B_0 of these RE elements in their elemental form were calculated and compared with available experimental data. As seen in Figure 3.3.4, our theoretical values are in excellent agreement with experimentally measured values. For lattice parameter a , the experimental and calculated values are very close. The overall agreement between calculated and measured lattice parameters and bulk moduli is very good. The c/a ratio of hcp structures lies between 1.55-1.6. Generally, the experimental values of c/a are a little bit larger than the calculated values. Nd and Pr are of dhcp structure and their experimental and calculated c/a values are in agreement lying between 3.2-3.25. All these results validate the selected PBE pseudopotentials. Actually, the PBE pseudopotential database contains usually more than one pseudopotential for each element. Different potentials for the same element are differentiated by a subscript after the name of element. These subscripts are included in the following tables and figures. Calculations using all available pseudopotentials were performed, and experimental values were used as validation criteria to choose the best PBE pseudopo-

**Figure 3.3.4:**

Comparison of experimental values and calculation values of (a) lattice parameter a , (b) bulk modulus B_0 , (c) c/a of hcp, and (d) c/a of dhcp. The purple line indicates experimental value equals to theoretical value. Experimental data are taken from [75].

Table 3.3.7:

DFT calculated I_1 stacking fault energy of Mg-RE alloys (in mJ/m^2). The subscripts "sv" and "3" are nothing but denotes of pseudopotentials used in the calculations.

(a) alloying element of hcp structure				
X	Mg	Mg_{31}X	Mg_{15}X	X
Dy_3	19.6	—	7.1	-16.2
Er_3	19.6	—	8.5	19.2
Gd_3	19.6	—	5.2	-43.6
Ho_3	19.6	12.4	7.82	1.3
Lu_3	19.6	—	9.8	59.7
Sc_sv	19.6	—	16.2	76.5
Tb_3	19.6	—	6.2	-31.2
Tm_3	19.6	13.3	8.96	36.6

(b) alloying element of dhcp structure				
X	Mg	Mg_{15}X	X	
Nd_3	19.6	0.3	-70.77	
Pr_3	19.6	-1.7	-70.78	

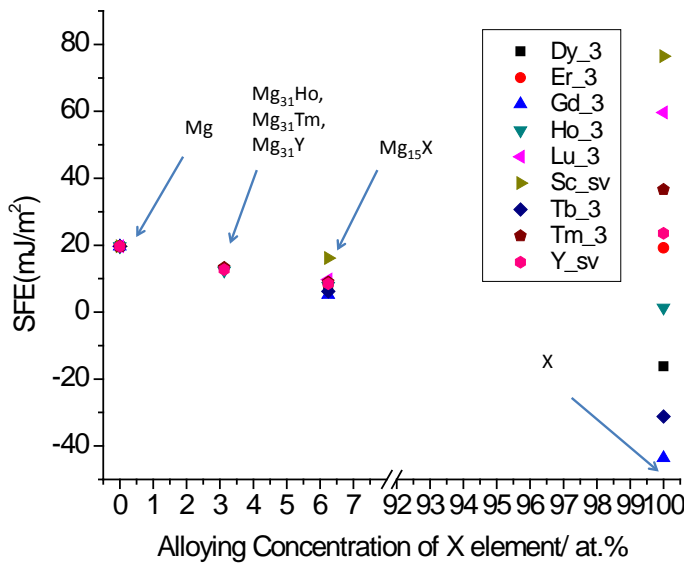
tentials. Those pseudopotentials were chosen which provide the better agreement with experimental values. Some pseudopotentials which have convergent problems (e.g. after a long time no convergent trend is observed) were not considered.

Stacking fault energies for different Mg-X alloys are listed in Table 3.3.7 and shown in Figure 3.3.5 (elements with hcp structure) - Figure 3.3.6 (elements with dhcp structure). Generally all considered rare earth elements exhibit a similar impact to yttrium. In rare-earth-element-containing Mg alloys stacking fault energies are lower than that in pure Mg regardless of the elemental stacking fault energies. But there are differences among the eight Mg_{15}X alloys. The stacking fault energy of Mg_{15}Sc is the highest among all studied alloys. The stacking fault energies of all other alloys with the same concentration are very close to each other. The SFE of Mg_{15}Gd is the lowest. The stacking fault energy of Mg_{31}Tm is between pure Mg and Mg_{15}Tm , and the SFE of Mg_{31}Ho and Mg_{31}Y are in the same range.

The stacking fault energies of elemental Dy, Tb, Gd is negative. According to our method, the negative sign is introduced by term $(E_{\text{dhcp}} - E_{\text{hcp}})$. Therefore, dhcp phase of these elements is more stable than hcp phase at 0 K. That is, the ground states predicted by these pseudopotentials at 0 K are different from at room temperature.

The theoretical I_1 SFE of Ho is very close to 0 (1mJ/m^2). This is very interesting, because theoretically the SFE equal to 0 corresponds to an infinite width of I_1 stacking fault.

Figure 3.3.6 shows stacking fault energies of Mg-X alloys with dhcp X (Nd, Pr). The stacking fault energies of Mg_{15}Nd and Mg_{15}Pr are almost the same and very close to 0

**Figure 3.3.5:**

Ab initio determined I_1 stacking fault energies of Mg-X alloys with different X concentrations. X represents the 9 rare earth elements of hcp structure. Four different concentrations are shown in the figure: pure magnesium, 3.125 at.% X (Ho, Tm), 6.25 at.% X and pure X. The corresponding data of Mg-Y alloy are also shown in the figure as a reference.

mJ/m^2 (Mg_{15}Nd , 0.3 mJ/m^2 ; Mg_{15}Pr , -1.7 mJ/m^2). Interestingly, the stacking fault energies of pure Nd and pure Pr are nearly identical (-70.8 mJ/m^2). For crystals of dhcp structure, the negative values come naturally. If we compare the stacking sequences of I_1 SF ($\dots \text{ABAB}|\text{ABAC}|\text{ACAC} \dots$) and dhcp ($\dots \text{ABAC}|\text{ABAC}|\text{ABAC} \dots$), it is easy to conclude that the four-layer periodic structure dhcp is essentially the core segment of the I_1 stacking fault (ABAC).

The structural, elastic and thermodynamic properties of RE Mg-X alloys are computed and listed in Table 3.3.8 and graphically shown in Figure 3.3.7. They all reduce the cohesive energy difference between the two phases. They increase the anisotropy of hcp Mg alloys by decreasing the c/a ratio which drops further away from ideal 1.633 (the trend is exactly same for dhcp case). They reduce the volume difference of hcp and dhcp phases and make them more similar. The difference of bulk moduli are also reduced from about -2.0% to within -1.0%. With these it is concluded that rare earth elements make hcp and dhcp Mg alloys structurally, elastically and thermodynamically similar, which finally enable the reduction of I_1 stacking fault energy. All rare earth elements change these computed properties in a consistent way which is similar as yttrium. The consistent chemical behaviors originate in essence from their similar electronic structures.

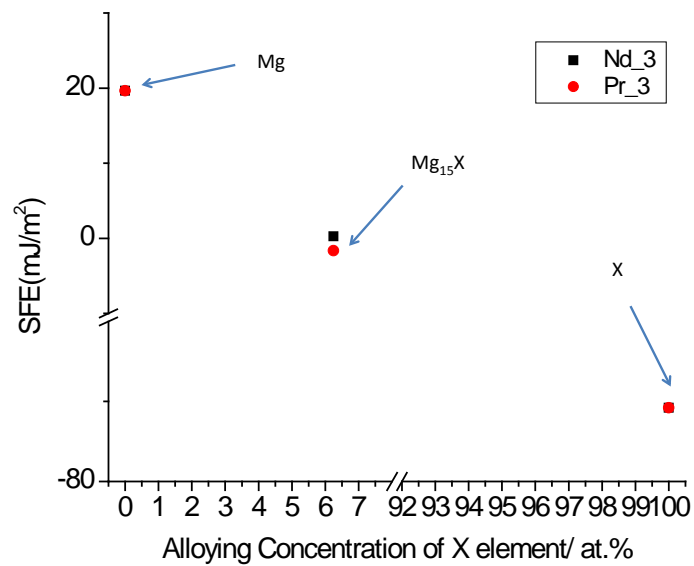


Figure 3.3.6:

Ab initio determined I₁ stacking fault energies of Mg-X alloys with different X concentrations. X represents the 2 rare earth elements of dhcp structure, Nd and Pr.

Table 3.3.8:

Ab initio calculated structural, elastic, and thermodynamic parameters of hcp and dhcp phases of $Mg_{15}X$ crystals with X being lanthanide, Sc and Y. Listed are total energy differences $E_{dhcp} - E_{hcp}$ (meV/atom) between $Mg_{15}X$ crystals with dhcp and hcp stackings; volumes per atom V ($\text{\AA}^3/\text{atom}$); bulk moduli B (GPa) for both hcp and dhcp crystals together with their relative ratios. Crystals of $Mg_{15}X$ are described by the c/a ratios (or half) in case of hcp (dhcp) structures.

solute	$E_{dhcp} - E_{hcp}$ (meV/atom)	V_{hcp} ($\text{\AA}^3/\text{atom}$)	V_{dhcp} ($\text{\AA}^3/\text{atom}$)	$(V_{dhcp} - V_{hcp})/V_{hcp}$ %	B_{hcp} (GPa)	B_{dhcp} (GPa)	$(B_{dhcp} - B_{hcp})/B_{hcp}$ %	$(c/a)_{hcp}$	$1/2(c/a)_{dhcp}$
Mg	5.4	22.85	22.93	0.34	36.3	35.6	-1.95	1.626	1.645
Sc	4.5	22.99	23.01	0.09	37.8	37.5	-0.72	1.594	1.602
Pr	-0.5	24.14	24.09	-0.22	35.5	35.3	-0.55	1.571	1.577
Nd	0.1	24.05	24.01	-0.18	35.8	35.5	-0.91	1.572	1.578
Gd	1.5	23.77	23.75	-0.07	36.6	36.5	-0.30	1.580	1.587
Tb	1.8	23.71	23.70	-0.05	36.8	36.7	-0.30	1.582	1.588
Dy	2.0	23.66	23.65	-0.03	36.9	36.8	-0.39	1.584	1.590
Ho	2.2	23.61	23.61	-0.02	37.0	36.9	-0.45	1.586	1.592
Er	2.4	23.56	23.56	0.00	37.1	36.9	-0.52	1.587	1.593
Tm	2.5	23.52	23.52	0.02	37.2	37.0	-0.57	1.589	1.595
Lu	2.8	23.44	23.45	0.04	37.3	37.1	-0.51	1.593	1.599
Y	2.4	23.71	23.70	-0.05	35.9	35.8	-0.38	1.582	1.587

3.3. Results and Discussion

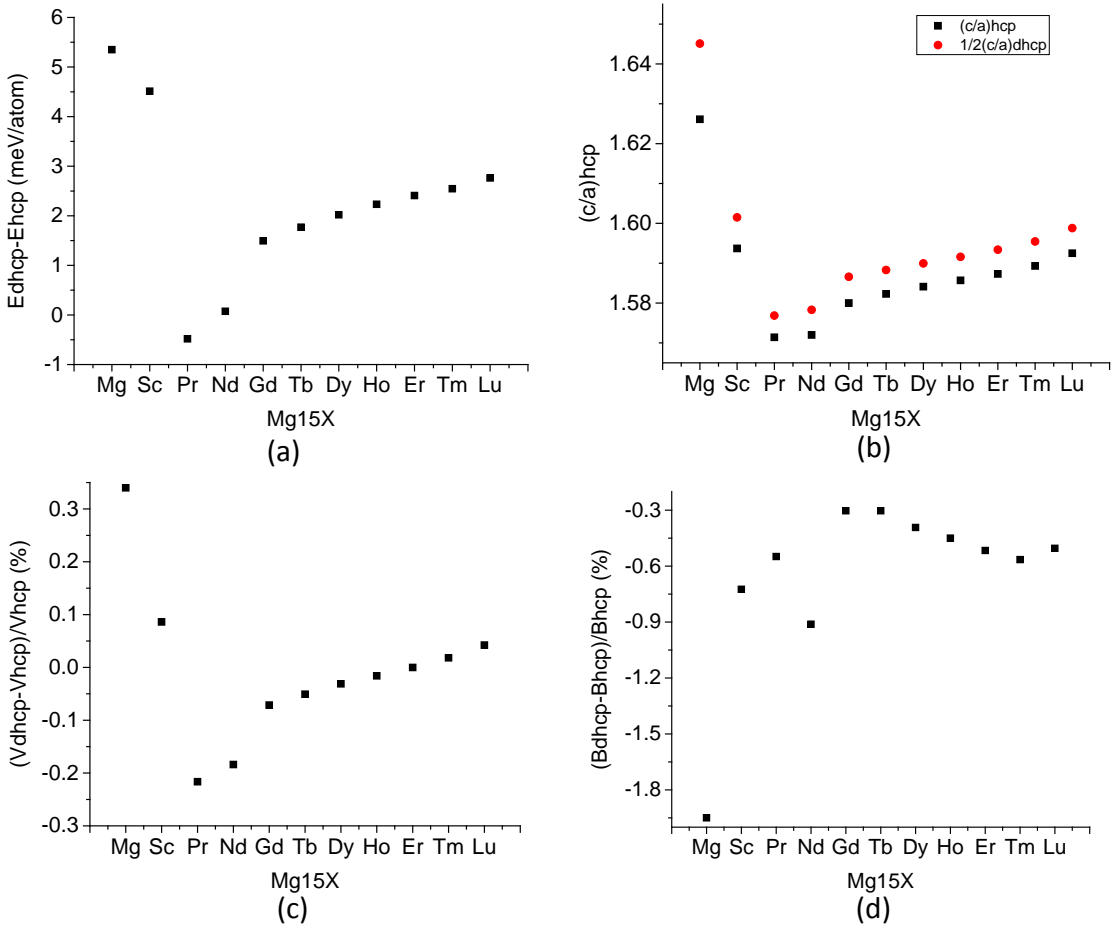


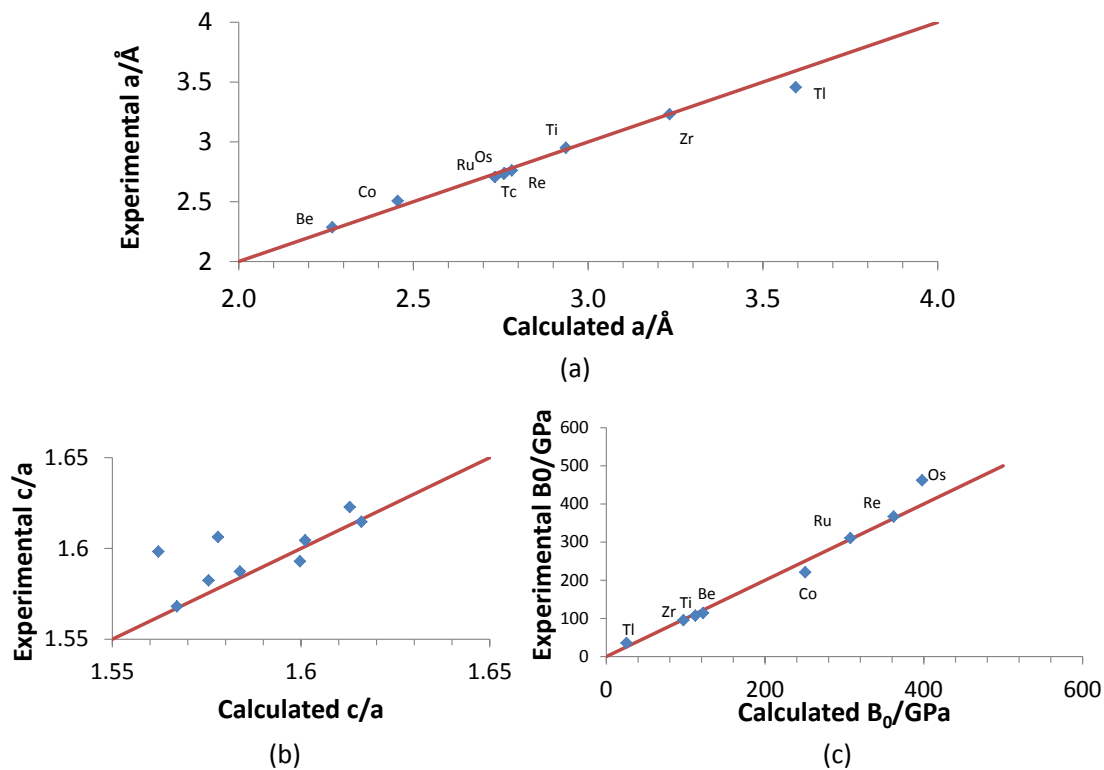
Figure 3.3.7:

Theoretically predicted differences of energetic, structural and elastic parameters of $Mg_{15}X$ crystals with X belonging to the lanthanide series (see also the values in Tab. 3.3.8) [77].

3.3.3 Mg-non-RE Alloys

Employing the same methodology as in the previous section, the stacking fault energies of magnesium alloyed with non-rare earth elements are studied. Alloys of magnesium containing 10 non-rare earth elements are considered. 8 of these solutes are transition metals, except Be and Tl.

As far as computational parameters are concerned, the same conditions as listed in Table 3.3.6 are used to ensure convergence of the calculated results of non-rare earth elements. Another reason to use these computational conditions is to enable the calculated results are directly comparable to Mg-RE alloys. Similarly as in the case of RE elements, different PBE pseudopotentials are tested in terms of the computed lattice parameters and bulk moduli of the pure metals. The theoretical results were compared with the corresponding experimental values of lattice parameter a , c/a ratio and bulk modulus in Figure 3.3.8. The lattice parameters of the pure elements are very close to the experimental values.

**Figure 3.3.8:**

Comparison of experimental and calculated values of lattice parameter a (a), c/a of hcp (b) and bulk modulus B_0 (c). The purple line indicates experimental value equals to theoretical value. The experimental data of rare earth elements are taken from [75].

The theoretically predicted c/a values are in good agreement with the experimental values, all around 1.6. The experimental values of bulk moduli of Os and Co deviate slightly from the calculated values but they are still satisfactory and the pseudopotentials are accurate for our computation. The bulk moduli of other considered elements are in very good agreement with the experimental values. Therefore the PBE potentials of the selected 10 elements are reliable.

The stacking fault energies for Mg-X alloys are summarized in Table 3.3.9, and shown in Figure 3.3.9. The stacking fault energies of Mg-non-RE alloys are higher than that of pure magnesium. Therefore it can be concluded that magnesium alloyed with the tested set of 10 non-rare earth elements seems not to improve its ductility. An interesting phenomenon is that the stacking fault energy of a pure Re crystal is much lower than that of $Mg_{15}Re$. This trend indicates that Re atoms have a different (or even opposite) effect as compared with Y atoms.

Table 3.3.9:
DFT calculated stacking fault energy of Mg-Non-RE alloys (in mJ/m^2)

X-element	Mg	Mg_{31}X	Mg_{15}X	X
Co	19.6	—	37.6	30.3
Os_pv	19.6	—	38.5	509.7
Tc_pv	19.6	—	36.2	33.5
Tl_d	19.6	—	22.1	46.6
Be	19.6	—	23.5	230.2
Re_pv	19.6	26.4	35.4	5.1
Ru_pv	19.6	—	40.5	398.7
Ti_pv	19.6	—	24.4	184.6
Zr	19.6	—	22.2	171.5
Zn	19.6	—	21.0	38.6

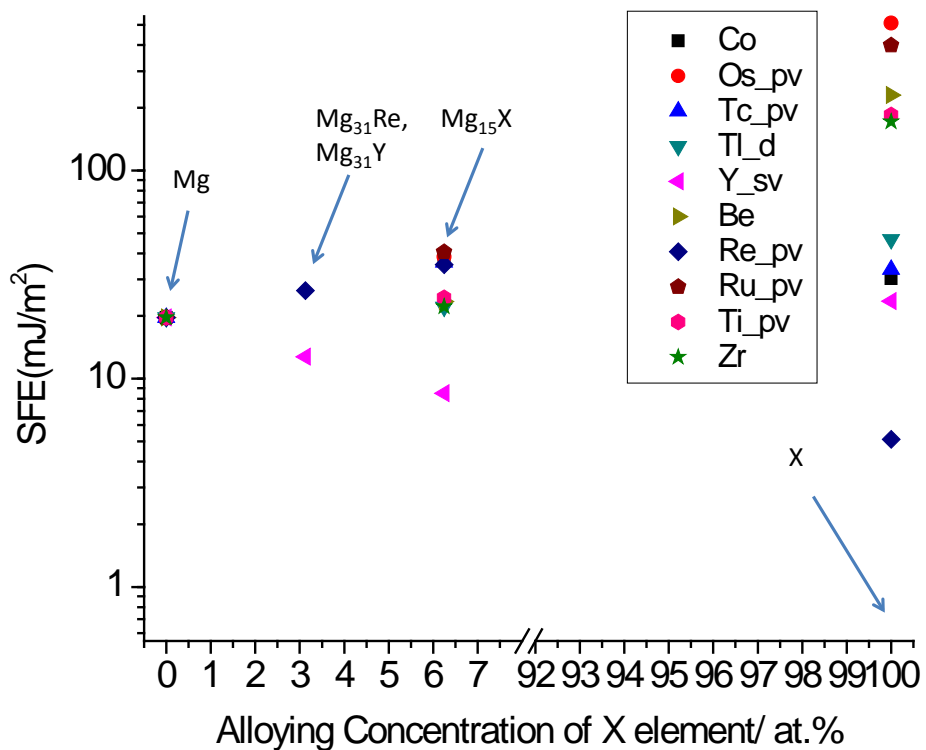


Figure 3.3.9:

Ab initio determined I_1 stacking fault energies of Mg-X alloys with different X concentrations. X represents the 8 non-rare earth elements of hcp structure.

Table 3.3.10:

Ab initio calculated structural, elastic, and thermodynamic parameters of hcp and dhcp phases of $Mg_{15}X$ crystals with X being non-lanthanide elements. Listed are total energy differences $E_{dhcp} - E_{hcp}$ (meV/atom) between $Mg_{15}X$ crystals with dhcp and hcp stackings, and volumes per atom V ($\text{\AA}^3/\text{atom}$) and bulk moduli B (GPa) for both hcp and dhcp crystals together with their relative ratios. Crystals of $Mg_{15}X$ are also described by the c/a ratios in case of hcp crystals and its half in case of dhcp ones.

solute	$E_{dhcp} - E_{hcp}$ (meV/atom)	V_{hcp} ($\text{\AA}^3/\text{atom}$)	V_{dhcp} ($\text{\AA}^3/\text{atom}$)	$(V_{dhcp} - V_{hcp})/V_{hcp}$ %	B_{hcp} (GPa)	B_{dhcp} (GPa)	$(B_{dhcp} - B_{hcp})/B_{hcp}$ %	$(c/a)_{hcp}$	$1/2(c/a)_{dhcp}$
Mg	5.4	22.85	22.93	0.34	36.3	35.6	-1.95	1.626	1.645
Be	6.2	21.87	21.95	0.34	37.0	36.7	-0.84	1.634	1.636
Ti	6.7	22.29	22.31	0.09	40.6	40.3	-0.87	1.592	1.604
Zr	6.2	22.73	22.73	0.03	39.6	39.3	-0.89	1.588	1.597
Tc	9.6	21.39	21.40	0.04	42.5	42.1	-0.95	1.598	1.616
Re	9.3	21.33	21.37	0.17	43.3	42.8	-1.18	1.608	1.625
Co	10.0	21.46	21.45	-0.05	38.5	38.4	-0.26	1.597	1.609
Ru	10.8	21.31	21.34	0.16	42.9	42.4	-1.18	1.589	1.609
Os	10.2	21.13	21.16	0.13	43.8	43.4	-0.93	1.598	1.618
Zn	5.7	22.26	22.33	0.31	36.8	36.5	-0.87	1.650	1.648
Tl	6.1	23.04	23.11	0.30	35.6	35.4	-0.55	1.640	1.648

3.3. Results and Discussion

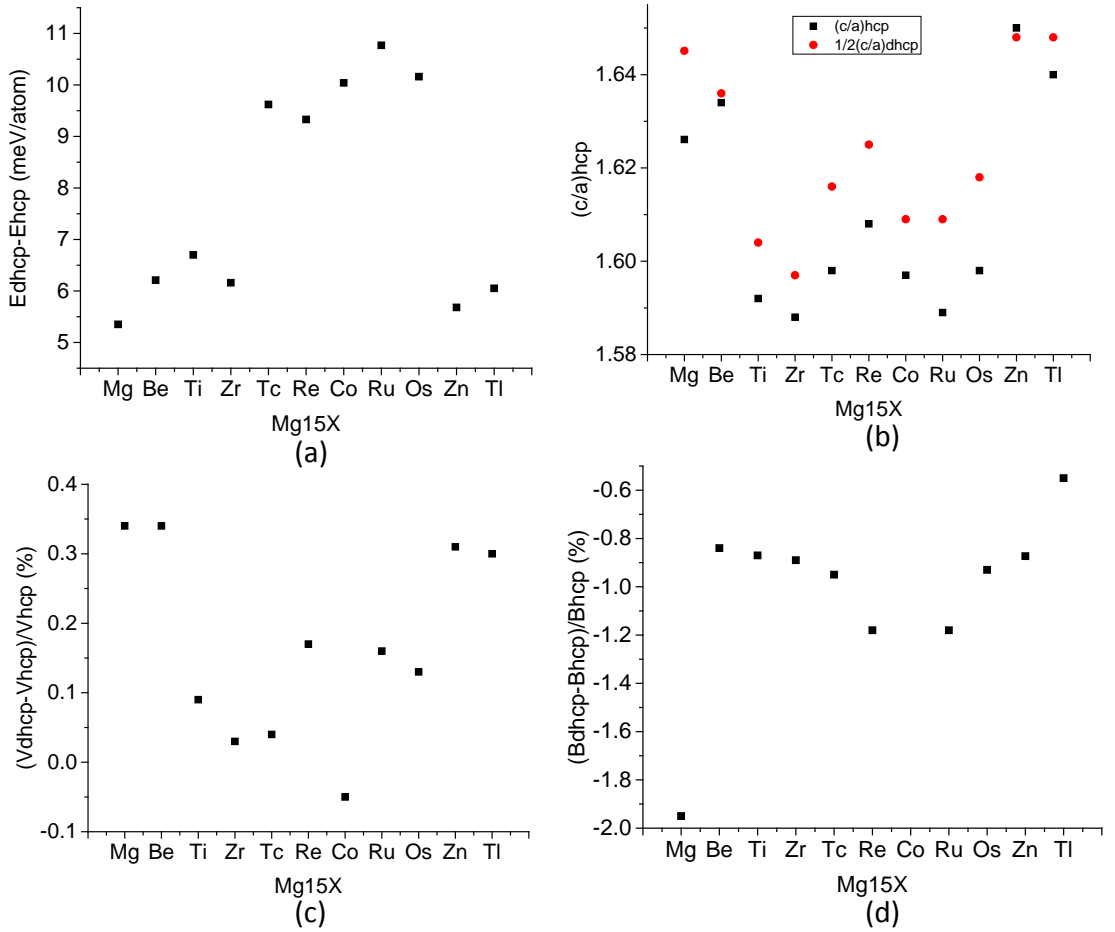
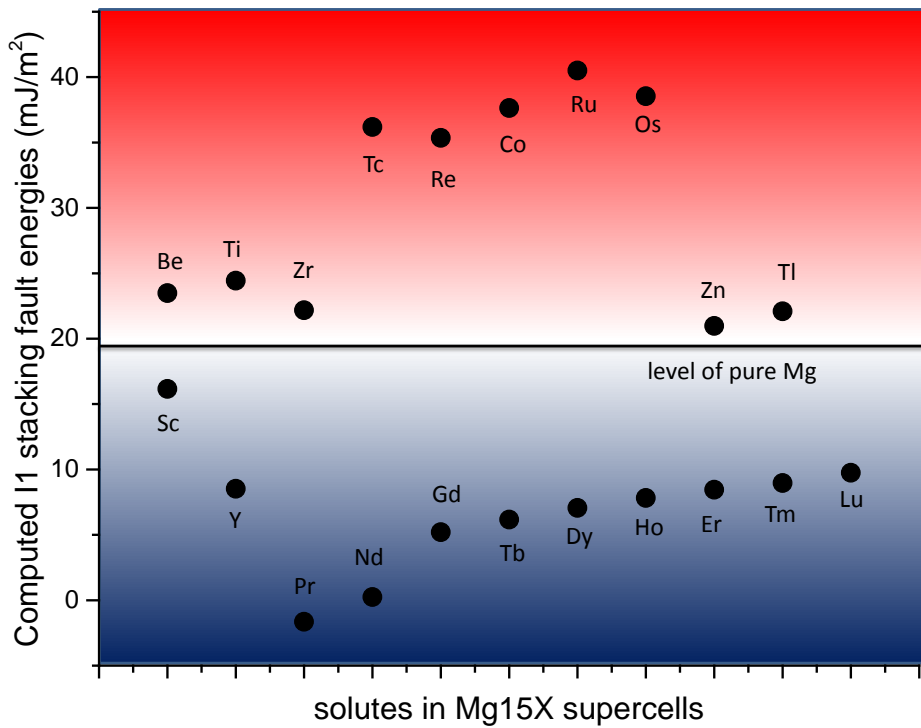


Figure 3.3.10:

Theoretically predicted differences of energetic, structural and elastic parameters of $Mg_{15}X$ crystals with hcp and dhcp stacking sequences with X being non-lanthanide atoms (see also in Tab. 3.3.10) [77].

The structural, elastic and thermodynamic properties of non-RE Mg-X alloys are computed which are listed in Table 3.3.10 and graphically shown in Figure 3.3.10. The non-RE elements change these computed properties in individual ways which are different from yttrium. They all increase the cohesive energy difference between the two phases by amount of 0.3-5.4 meV/atom. Except Be, Zn and Tl, the others increase the anisotropy of hcp Mg alloys by decreasing the c/a ratio which drops further away from ideal 1.633 (the trend is somehow similar for dhcp case). Beryllium does not change the volume difference of the two phases and all others reduce the volume difference and make them more similar. The difference of bulk moduli are also reduced from about -2.0% to within -0.55% to -1.18%. The inconsistent changes of the considered properties are expected since these non-RE elements are from different groups and periods, which indicates their obvious different chemical properties. The strong increases of cohesive energy difference together with the weak variance of volume difference determine the increased I_1 stacking fault energies.

**Figure 3.4.1:**

DFT computed values of the I_1 intrinsic stacking fault energy in $Mg_{15}X$ crystals ($X = Dy, Er, Gd, Ho, Lu, Sc, Tb, Tm, Nd, Pr, Y, Be, Ti, Zr, Zn, Tc, Re, Co, Ru, Os, Tl$) with respect to the value for pure magnesium [77].

3.4 Conclusions

In this chapter the impact of solutes on the I_1 SFE of magnesium alloys was studied employing density functional theory. The theoretical calculations verify that the I_1 intrinsic stacking fault energy of Mg-Y alloys is lower than that of pure magnesium, causing a ductility improvement in Mg-Y alloys. Besides Mg-Y alloys, magnesium alloys containing elements with hcp or dhcp structure (room temperature) are studied. Except for those that are not in the VASP database or are radioactive (except technetium), the selected elements are divided into two different groups- (i) group of rare earth elements and (ii) group of non-rare earth elements. All elements of the first group can reduce the I_1 stacking fault energy when alloying with magnesium. That indicates that all rare earth studied here can theoretically improve the room temperature ductility of magnesium. However, the stacking fault energy of magnesium alloys containing elements from the second group increases. These primary results are summarized in Figure 3.4.1.

Chapter 4

Inter-relations between SFE and Properties of Elemental Solutes

In the last chapter a scale-bridging connection between an increased macroscopic ductility with a solute-induced reduction of the I_1 intrinsic stacking fault energies (I_1 SFE) was identified. Quantum-mechanical calculations, that we earlier used, are reliable, accurate and versatile but computationally too demanding for a rapid theory-guided alloy prototyping. Therefore, in order to identify a method allowing for a fast solute assessment without lengthy *ab initio* calculations, we will analyze correlations and anti-correlation between the I_1 SFEs and materials parameters of the elemental solutes in this chapter.

4.1 Introduction

Since rare earth (RE) elements are expensive due to environmental and health-risk issues, it is desirable to identify alternatives solutes that ductilize Mg similarly as RE elements do. In our previous study [77], we selected 21 elements from the periodic table that crystallize in their pure form under ambient conditions in either hcp or double hcp (dhcp) structure. Then we performed *ab initio* calculations of the I_1 stacking fault energies of binary Mg alloys containing these elements in solute solutions. We found that all rare earth elements reduce the I_1 SFE while all other studied non-rare earth (Non-RE) elements increase the I_1 SFE. As RE elements are known to increase the ductility in Mg, we connect the fact that (i) RE elements reduce the I_1 SFE with the enhanced ductility in Mg alloys. Our proposed scale-bridging linked was confirmed experimentally for four Mg alloys containing selected RE elements (Tb, Dy, Er and Ho).

The present work extends the connection between the I_1 stacking fault and the ductility. Our approach is complementary to other scale-bridging explanations of ductility in Mg alloys. To name a few examples, Yasi and co-workers [26] simulated the core structures of basal and prismatic dislocations by the flexible boundary condition method and later developed different models to calculate the critical resolved shear stresses (CRSS) of basal dislocations [78] and cross-slip stresses of prismatic screw dislocations [79] in Mg alloys. As a result of these studies, low concentrations of yttrium were predicted to significantly

reduce the cross-slip stress in Mg-alloys, which indicates an improved ductility of the material in agreement with our previous findings. As another example, Shin *et al.* [80] developed so-called orbital-free density functional theory (OFDFT) method and applied it to dislocation core structures and subsequently also Peierls stresses [81] in pure Mg. Stacking fault energies are among the key materials properties affecting a macroscopic mechanical behavior of metallic alloys. The I_1 , I_2 as well as unstable stacking faults have been intensively studied in Mg [29, 30, 31, 32, 33, 34]. Their simulation by quantum-mechanical methods is, however, computationally rather demanding and lengthy. A faster approach, which does not require explicit *ab initio* SFE methodology, would be desirable for a future rapid alloy design and quick selection of solutes. Therefore, we here systematically study inherent inter-connection between stacking fault energies in Mg alloys and properties of elemental solutes that are known and tabulated. Specifically, we analyze the relations between the I_1 SFE in Mg-X binaries and five different physical quantities of pure solutes: (i) their atomic volume, (ii) atomic number, (iii) I_1 SFE, (iv) electronegativity, and (v) the bulk modulus. We also analyzed the volume per atom in $Mg_{15}X$ alloys. As we find the atomic volume, electronegativity and the bulk modulus of elemental solutes clearly related to the I_1 SFE in Mg-X binaries, we propose a single numerical parameter containing these relations and suggest that this new figure of merit can be used as an indicator of stacking fault energy changes, and thus the ductility, in Mg alloys.

4.2 Computational Methodology

The computational methods of I_1 stacking fault energies of Mg alloys are same as in previous chapter, so we do not describe them here. In addition, we define some relative quantities employed in this chapter only for convenience. The relative volume change due to alloying is defined as:

$$\Delta V(Mg_{15}X) = V(Mg_{15}X) - V(Mg16) \quad (4.2.1)$$

and the relative change of the stacking fault energy due to alloying as:

$$\Delta I_1SFE(Mg_{15}X) = I_1SFE(Mg_{15}X) - I_1SFE(Mg). \quad (4.2.2)$$

Here, Mg is taken as the reference ($\Delta V(Mg) = 0$ and $\Delta I_1SFE(Mg) = 0$).

The I_1 SFEs of 18 different Mg alloys were calculated including 8 rare earth solutes (RE=Er, Ho, Lu, Sc, Tm, Nd, Pr, Y) and 10 non-RE elements (non-RE= Co, Os, Tc, Ti, Be, Re, Ru, Ti, Zr and Zn). As the applied method based on the ANNNI model was validated particularly for hcp and dhcp metals, lanthanides with other crystal structures (Ce, Pm, Sm, Eu, and Yb) were not considered. Since the PAW pseudopotentials available in the VASP database cannot correctly predict the ground state of Gd, Tb and Dy, we have not considered them either.

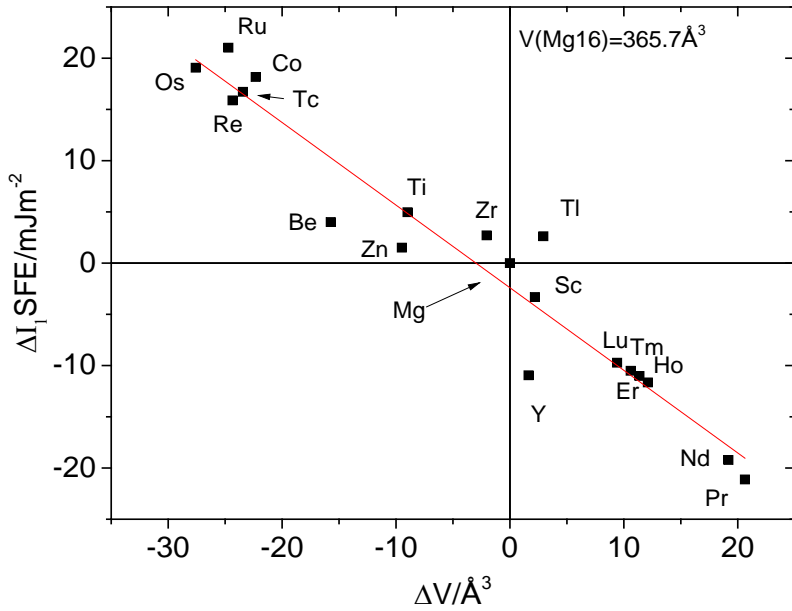


Figure 4.3.1:

Relative change of the stacking fault energy $\Delta I_1\text{SFE}$ of Mg_{15}X as a function of the change of volume per atom in a Mg-alloy $\Delta V(\text{Mg}_{15}\text{X})$. The data-points can be divided into two groups by the atomic volume of pure Mg (365.7\AA^3). All RE-elements increase the volume of Mg_{15}X alloys. Almost all Non-RE elements reduce the Mg_{15}X volumes, with Tl being an exception.

4.3 Results

4.3.1 Relation between $\Delta I_1\text{SFE}(\text{Mg}_{15}\text{X})$ and Volumes

First we analyze the relation between the I_1 stacking fault energy and the volume per atom in Mg_{15}X alloys. Figure 4.3.1 shows the computed $\Delta I_1\text{SFE}$ s as a function of the relative atomic volumes of these alloys. Generally, the $I_1\text{SFE}$ is lower when the volume of the alloy is larger. This strong anti-correlation between $\Delta I_1\text{SFE}(\text{Mg}_{15}\text{X})$ and $\Delta V(\text{Mg}_{15}\text{X})$ can be mathematically expressed by a Pearson's correlation coefficient $r = -0.97$. Mg-RE alloys have a larger atomic volume than pure Mg, and thus they lower the $I_1\text{SFE}$ with respect to pure Mg. The $\Delta I_1\text{SFE}(\text{Mg}_{15}\text{X})$ values for elements of the lanthanide series are very close to each other, probably because they share a similar electronic structure. Mg-Y deviates from this pronounced trend. When comparing Y and Sc, Mg-Y has a larger volume than Mg-Sc, but a lower $\Delta I_1\text{SFE}(\text{Mg}_{15}\text{X})$ than Mg-Sc (that is 50% higher). One origin of this difference may lie in their electronic structures. Scandium and yttrium belong to the same group (IIIB group) as the lanthanide series elements, but they are in different periods and, consequently, have different outer electron shells. The electrons in these atomic shells may account for the differences in the $I_1\text{SFE}$. The relation between the $I_1\text{SFE}$ and the period number will be discussed in detail below.

Almost all Mg-alloys containing Non-RE solutes have negative $\Delta V(\text{Mg}_{15}\text{X})$ values and

positive $\Delta I_1 \text{SFE}(\text{Mg}_{15}\text{X})$ values. The only exception is Tl; Mg_{15}Tl has a larger volume than Mg and also higher I_1 stacking fault energy than Mg. As the Non-RE elements are from different groups and periods, they share hardly any similarity in their electronic structures, therefore the data points of Mg-Non-RE alloys are more scattered around the interpolating line. Importantly, we can conclude that the volume per atom in Mg alloys is strongly anti-correlated with its I_1 SFE and the atomic volume of alloys is a reliable indicator of the stacking fault energy changes.

Having the stacking fault energy in Mg-alloys related to atomic volume in these alloys, we further analyze the latter as a function of the atomic volume of elemental solutes. Figure 4.3.2 shows the relation between the atomic volume of a solute X and the average atomic volume V of Mg_{15}X alloys. It is worth mentioning that DFT methods usually predict the lattice parameters very accurately with only very small deviations from experimental data. Here both volumes are derived from *ab initio* calculation. The values follow a rather intuitive trend: when a larger atom X is put into Mg_{15}X supercell, the average atomic volume of the alloy increases. Most of the considered elements follow this trend. The high Pearson's correlation coefficient $r = 0.95$ indicates a strong correlation between the elemental volume and the alloy volume. Nevertheless, there are exceptions from this rule. For example, elemental zirconium (Zr) is larger than Mg, but the atomic volume of Mg_{15}Zr is smaller than the volume of both pure Zr and Mg. Another exception is Tl. The volume of Tl is 30% larger than Mg, but when incorporated into the Mg matrix it changes less than 1% of the average volume of Mg_{15}Tl . We assume that strong chemical bonds are formed between Mg atoms and these solutes (e.g.. Zr, Tl) and subsequent electron transfers lead to this anomaly. In the Non-RE group, Tc, Ru, Re and Os deviate slightly from this linear trend. These four transition metals have approximately the same volume and all significantly reduce the atomic volume of Mg_{15}X (which is even smaller than that in Mg_{15}Be). The contracted volumes also indicate formation of strong chemical bonds.

4.3.2 I_1 Stacking Fault Energies in Pure Solutes and Mg Alloys

Figure 4.3.3 shows the relation between the I_1 SFEs in (i) Mg_{15}X alloys and (ii) pure solutes X. The stacking fault energy of Mg_{15}X increases slowly with the SFE of pure X but a clear linear trend is not evident. Still, the increasing trend can be interpreted such that if an I_1 SF is energetically difficult to form in a metal X, so it is in the Mg_{15}X alloy. The points can be fitted to a linear relation but the corresponding correlation coefficient, $r = 0.67$, is rather low. The linear fit equation reads (unit in mJm^{-2})

$$\gamma(\text{Mg}_{15}\text{X}) = (0.061 \pm 0.015) \gamma(\text{X}) + (12.96 \pm 2.45). \quad (4.3.1)$$

Interestingly, the slope is $0.061 \pm 0.015 \approx 0.0625 = 1/16$, which is exactly the atomic concentration of element X in Mg_{15}X . However an approximation based on the fractional concentrations is only roughly indicative. Among the studied elements, Re, Co, and

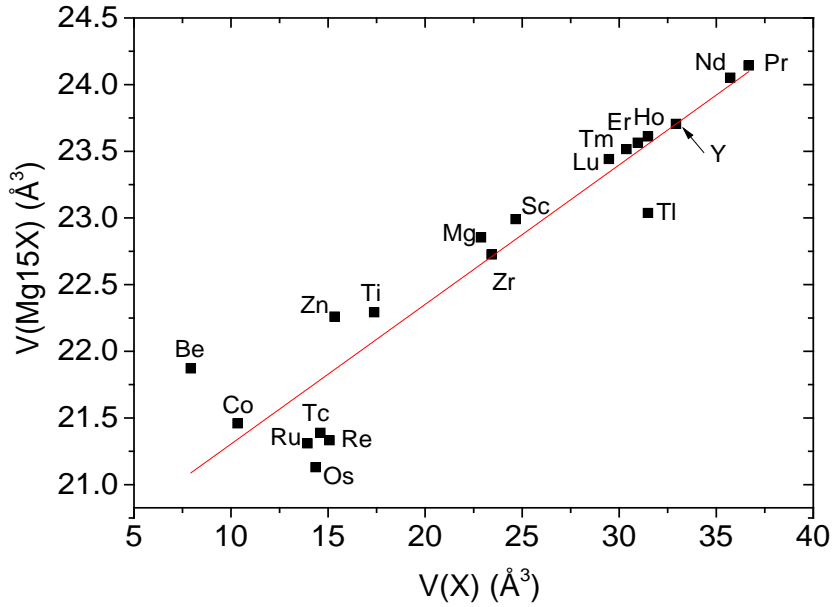


Figure 4.3.2:

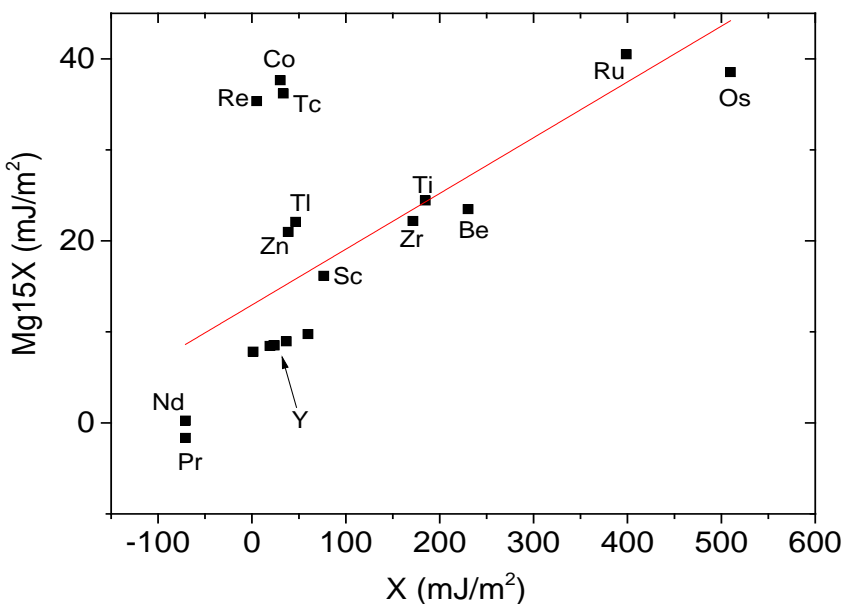
Relation between $V(Mg_{15}X$, per atom) and $V(X$, per atom). The data-points mostly follow a linear trend: a larger atomic volume of X correlates with a larger averaged atomic volume of $Mg_{15}X$.

Tc possess medium-level stacking fault energies but when added into $Mg_{15}X$ supercells, the corresponding alloys have rather high stacking fault energies ($\approx 35 \text{ mJm}^{-2}$). In an opposite manner, the stacking fault energy of rhenium is significantly lower (5 mJm^{-2}) than that in $Mg_{15}\text{Re}$ (35 mJm^{-2}).

The negative stacking fault energies of $Mg\text{-}X$ alloys ($X\text{=Nd, Pr}$) can be understood in such a way that the $I_1\text{SF}$ can form energetically spontaneously, and there is no extra energy needed to obtain $I_1\text{SF}$ in the alloys. In ANNNI model, the $I_1\text{SFE}$ is proportional to term $(E_{\text{dhcp}} - E_{\text{hcp}})$, i.e., the total energy difference between the phases with hcp and dhcp stacking sequences. When $I_1\text{SFE}$ is negative, $E_{\text{dhcp}} < E_{\text{hcp}}$, the alloy is more energetically stable in a dhcp structure than in the hcp one. It should be noticed that, if we compare the stacking sequences of $I_1\text{SF}$ ($\dots \text{ABAB}|\text{ABAC}|\text{ACAC} \dots$) and dhcp ($\dots \text{ABAC}|\text{ABAC}|\text{ABAC} \dots$), it is easy to conclude that the four-layer periodic structure dhcp is essentially the core segment of the I_1 stacking fault (ABAC).

4.3.3 I_1 Stacking Fault Energies and the Atomic Number of Solutes

The lanthanide elements have similar affinities and chemical properties which is a result of similar atomic and electronic structures, and they are often visualized in the periodic table of elements as a single element. Therefore we have defined an average $I_1\text{SFE}$ for the considered lanthanide elements. The $I_1\text{SFEs}$ as a function of period are shown in Figure 4.3.4(a) and (b). The $I_1\text{SFEs}$ of elemental RE and Non-RE solutes decrease with

**Figure 4.3.3:**

Relation between the I_1 SFE of $Mg_{15}X$ alloy and the I_1 SFE of elemental X.

increasing atomic numbers, but the slope levels down for higher atomic numbers. A similar trend is predicted also for the respective $Mg_{15}X$ ($X=RE$) alloys but with a smaller slope.

All ten considered Mg-non-RE alloys, which belong to three different periods, are shown as function of group number (see Figure 4.3.4(c)). The I_1 SFEs of $Mg_{15}X$ of these alloying elements increase when moving from group IVB to VIIIB and decrease from group VIIIB to IIIA (see the values for periods 4 and 6). Figure 4.3.4(d) shows the I_1 SFE of five RE elements and four non-RE elements in Period 6. From Pr to Os, the I_1 SFE values increase with the atomic number but then they decrease (see the data point for Tl). The increasing rate from Lu to Os is higher compared to that from Pr to Lu.

If we do not collapse all lanthanides into a single data point but visualize them separately, the I_1 SFEs of lanthanides are shown in Figure 4.3.5. The I_1 SFE values grow as a function of the atomic number within the lanthanide series in case of both elemental solutes and Mg-alloys containing them. The two trends in I_1 SFEs as a function of the atomic number (lanthanides and Mg-alloys) are different and, therefore, they are individually depicted in Figures 4.3.5 (a) and (b). The I_1 SF energies in pure solutes grow in a concave manner as a function of the atomic number (Figure 4.3.5(a)) while for $Mg_{15}X$ alloys, the I_1 SFE values first increase in a convex manner and then increase in a concave manner for higher atomic numbers (Figure 4.3.5(b)).

4.3.4 I_1 Stacking Fault Energies and Electronegativity

The I_1 stacking fault energies computed for different binary Mg alloys as a function of the electronegativity of the individual alloying elements are depicted in Figure 4.3.6. The

4.3. Results

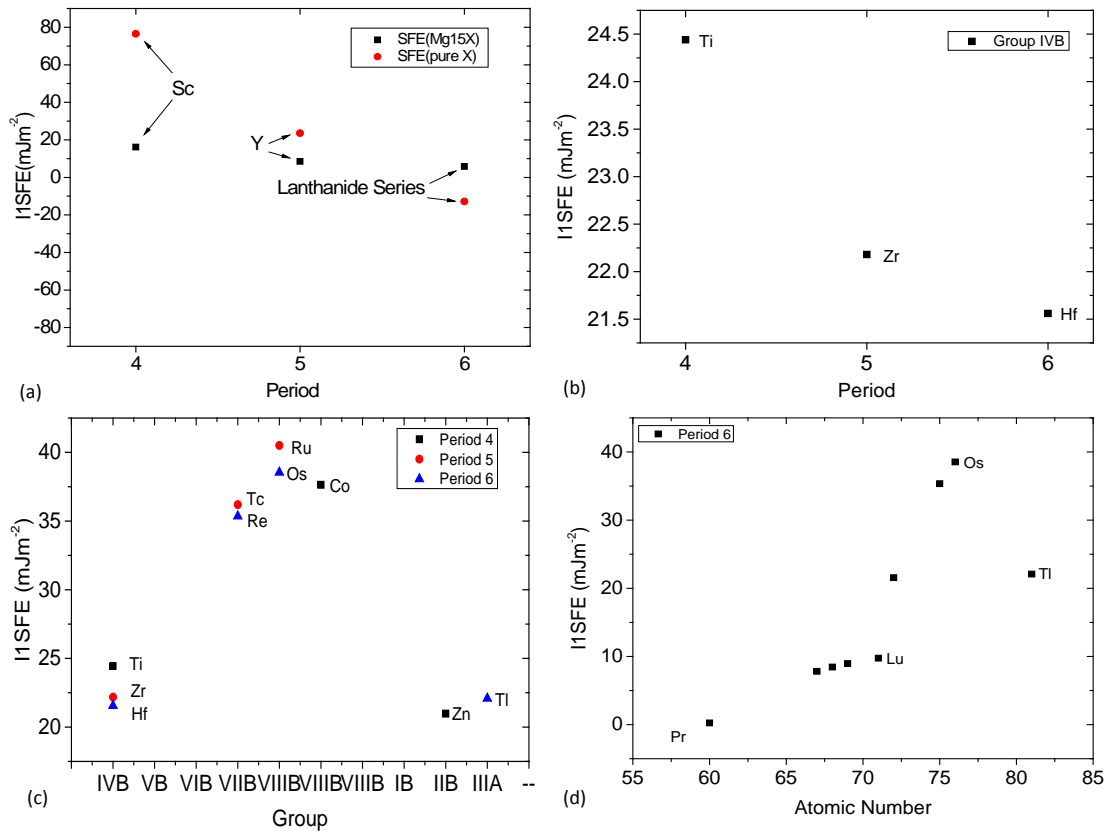


Figure 4.3.4:

The I₁SF energies as functions of the period number (a,b), the group number (c) and the atomic number (d).

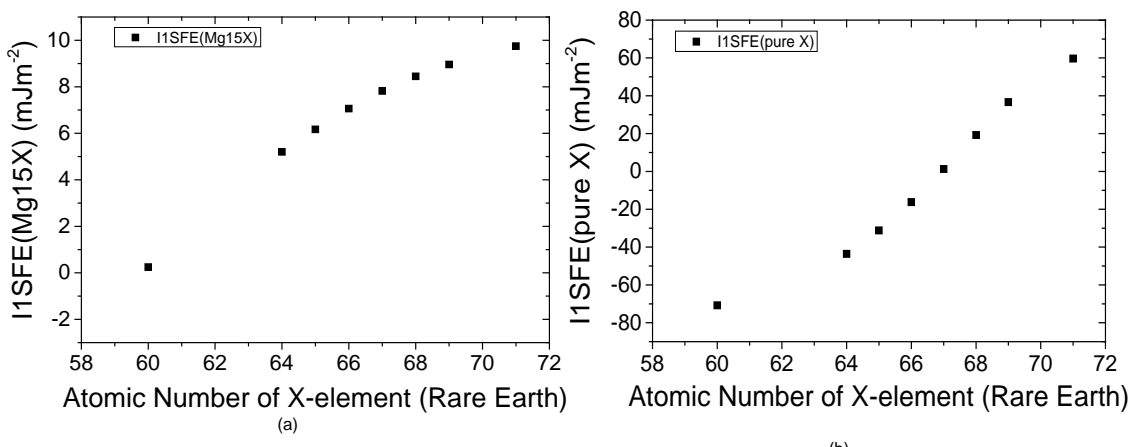
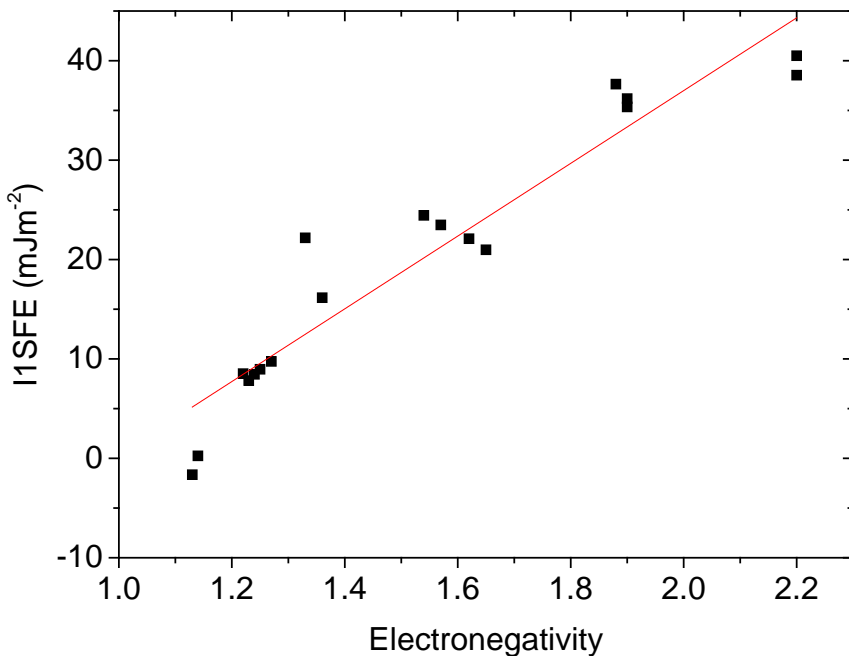


Figure 4.3.5:

Computed I₁SFE in (a) Mg₁₅X alloys (X=RE elements) and (b) elemental Sc, Y and lanthanides as function of the atomic number of element X.

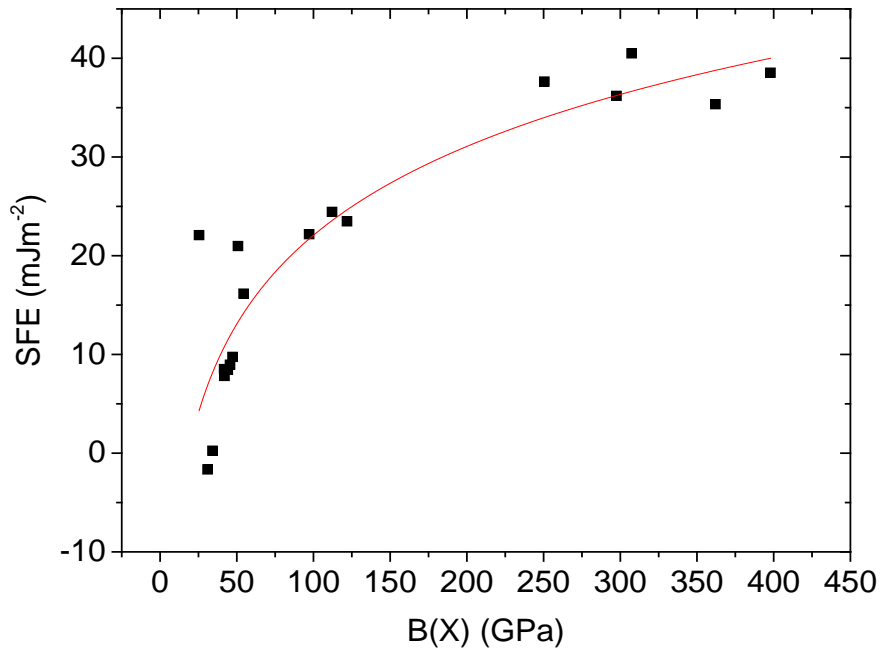
**Figure 4.3.6:**

Relation between the computed I_1 SFE in $Mg_{15}X$ alloys and the electronegativity of different solute elements X from [82].

data for the electronegativity have been taken for all considered solutes (both rare earth and others) from Ref. [82]. The values of I_1 SFE in $Mg_{15}X$ increase with increasing electronegativity of elemental solutes. The data points seem to be strongly correlated and the corresponding Pearson's correlation coefficient, $r = 0.95$, is very high. The electronegativity is an excellent linear indicator of stacking fault energy changes induced by alloying.

4.3.5 I_1 Stacking Fault Energies and Bulk Modulus

Figure 4.3.7 shows the relation between the I_1 SF energies in $Mg_{15}X$ alloys and the value of the bulk modulus of solute elements. The bulk moduli are calculated for all considered metals at their ground state structure, i.e. dhcp crystal in the case of Pr and Nd and hcp for all other considered metals. The I_1 SF energies in $Mg_{15}X$ alloys clearly grow as a function of the bulk modulus computed for the elemental solutes but the trend visible in Figure 4.3.7 is not a simple linear function. We propose a logarithmic relation between both quantities, as it seems to fit better and gives a rather high correlation coefficient $r= 0.90$. The bulk modulus is thus a good logarithmic indicator of I_1 stacking fault energy changes upon alloying.

**Figure 4.3.7:**

Relation between the computed I_1 SFE($Mg_{15}X$) and the bulk modulus of element X from [82] and [83].

4.4 Discussion

We have studied five separate dependencies between the I_1 stacking fault energies of Mg alloys on the one hand and various materials characteristics of elemental solutes on the other. We find that three of them possess strong (anti-)correlations with the I_1 SF energies, specifically, (i) the atomic volume; (ii) electronegativity; and (iii) the bulk modulus. The corresponding Pearson's correlation coefficients are -0.97, 0.95 and 0.90, respectively. Interestingly, the I_1 SF energies are found to be (anti-) correlated to (i) the volume, i.e., a structural characteristic, (ii) the electronegativity that is an electronic structures property, and (iii) the bulk modulus, one of the elastic parameters. Similar mutual (anti-) correlations were previously found also in other systems. For example, in the case of body-centered-cubic Fe-Ti alloys, their thermodynamic stability (expressed by their formation energies) were found to be strongly related to their density of state at the Fermi level (an electronic structure characteristic) and, furthermore, each of these properties (the formation energy and the density of states) were found to be strongly (anti-) correlated with the polycrystalline Young's modulus of these alloys [84]. Other (anti-) correlations between the thermodynamic stability and elastic parameters were found in face-centered-cubic alloys e.g. Ni-W [85] or Ni nitrides [86]. Apparently, such relations between the atomic-scale electronic structure parameters and macro-scale properties are rather independent on the actual crystal structure and material system. A comparison of the above discussed parameters is presented in Figure 4.4.1, where all elements are sorted according to their (a) atomic radius, (b) electronegativity and (c)

bulk modulus. From Figure 4.4.1 it is evident that all elements which reduce the I_1 SFE in Mg (lanthanides, Y, Sc) have (i) large atomic radii of ≥ 184 pm (Mg: 145 pm), (ii) electronegativity values close to that of Mg (1.1 - 1.3) and (iii) bulk moduli close to Mg (32 - 56 GPa). A more detailed analysis of these parameters shows that Sc, which only moderately reduces the I_1 SFE in Mg, fulfills all three criteria but its values are a bit away from those of Y and the lanthanides. Additionally, it was revealed that none of the other elements (i.e. others than lanthanides, Y and Sc) fulfills all three criteria.

Having all these above discussed findings we see that there are three critically important parameters of solutes (the atomic volume, electronegativity, and the bulk modulus) that should be considered. As it is rather inconvenient to simultaneously consider multiple criteria, we below attempt to provide a single evaluation factor integrating all three parameters. Due to the fact that we aim at ductility improvements, we use yttrium as a reference below because Y is known to improve the ductility of Mg alloys [9, 23, 6]. Below we thus compare properties of other solutes with those known for Y. Based on the above summarized relations we define an yttrium similarity index (YSI), a new numerical indicator which combines the atomic volume, electronegativity and the bulk modulus. We define the YSI as follows

$$YSI_i = 1 - \sqrt{w_v(v_i - v_Y)^2 + w_\nu(\nu_i - \nu_Y)^2 + w_B(B_i - B_Y)^2} \quad (4.4.1)$$

where $i = \text{H, Li, Be, ... Bi}$. The quantities v , ν and B represent the atomic volume, electronegativity and the bulk modulus of an element, respectively, and w_v , w_ν and w_B are the weights of the three components. Their values are determined by the slopes of their linear fitting equations and normalized by setting the maximal YSI_i as 1. Under these conditions, $(w_v, w_\nu, w_B) = (1.887, 1.777, 0.511)$. The three components enter this equation normalized by the largest values of the selected 76 elements from the periodic table of elements, namely the atomic volume of Cs ($1.175 \times 10^{-28} \text{ \AA}^3$), the electronegativity of F (3.98), and the bulk modulus of Os (462 GPa). As the reference, the atomic volume, electronegativity and bulk modulus of yttrium are $5.53 \times 10^{-29} \text{ \AA}^3$, 1.22 and 41 GPa. The YSI parameter defines a specific metric or "distance" between an element and yttrium in a property space. The larger YSI is, the more similar it is to yttrium.

The YSI values computed for 76 elements from the periodic table of elements are shown in Figure 4.4.2 as three different color-coded maps, projections on the planes with different pairs of property combinations, (i) the atomic volume and electronegativity; (ii) the atomic volume and bulk modulus; and (iii) the electronegativity and bulk modulus. In all three projected figures, yttrium is located in the centers of ellipses surrounded with lanthanides. For the lanthanide series (from Ce to Lu), the YSI values are very large and close to each other. By using the YSI we can identify the lanthanide elements as the most similar elements to yttrium (see Table 4.4.1). That matches the above discussed I_1 stacking fault energies which are low for Mg-RE binaries. The non-RE elements with the highest YSI values (0.84-0.86) are Na, Ca, Zr, Tl, and Li. Judging from their YSI values which are very close to Mg (0.84), these non-RE elements do not guarantee a reduction of

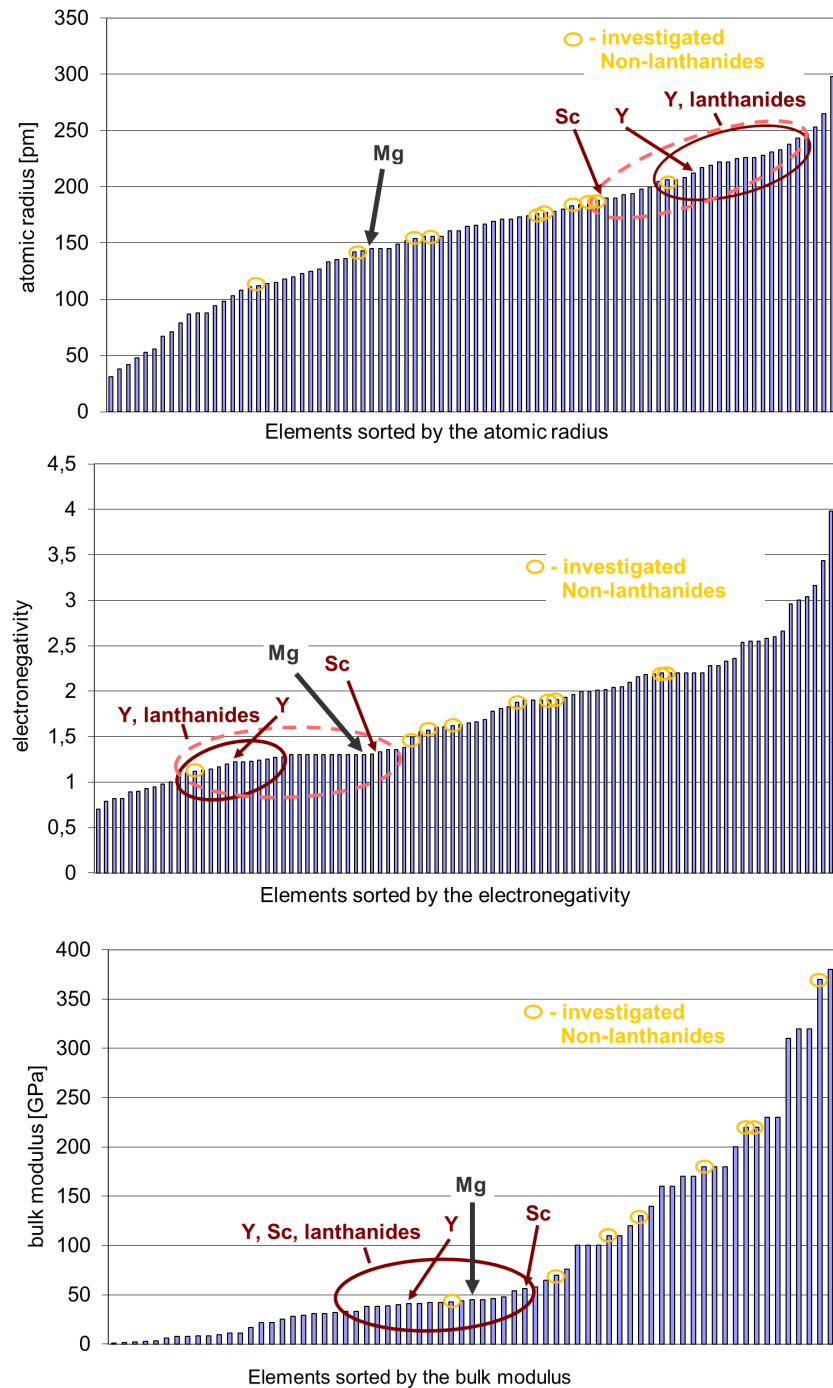


Figure 4.4.1:

Selected 76 elements from the periodic table sorted by their (a) atomic radius, (b) electronegativity and (c) bulk modulus [82] (see also Appendix); the lanthanides, Y and Sc have (i) large atomic radii of ≥ 184 pm (Mg: 145 pm), (ii) electronegativity values close to the that of Mg (1.1 - 1.3) and (iii) bulk moduli close to Mg (32 - 56 GPa); none of the other elements have all three parameters in the same range; the elements which were considered in the present study and calculated to increase the I_1 SFE are shown by yellow circles. The pink dash-line circles the lanthanide series and Sc, Y.

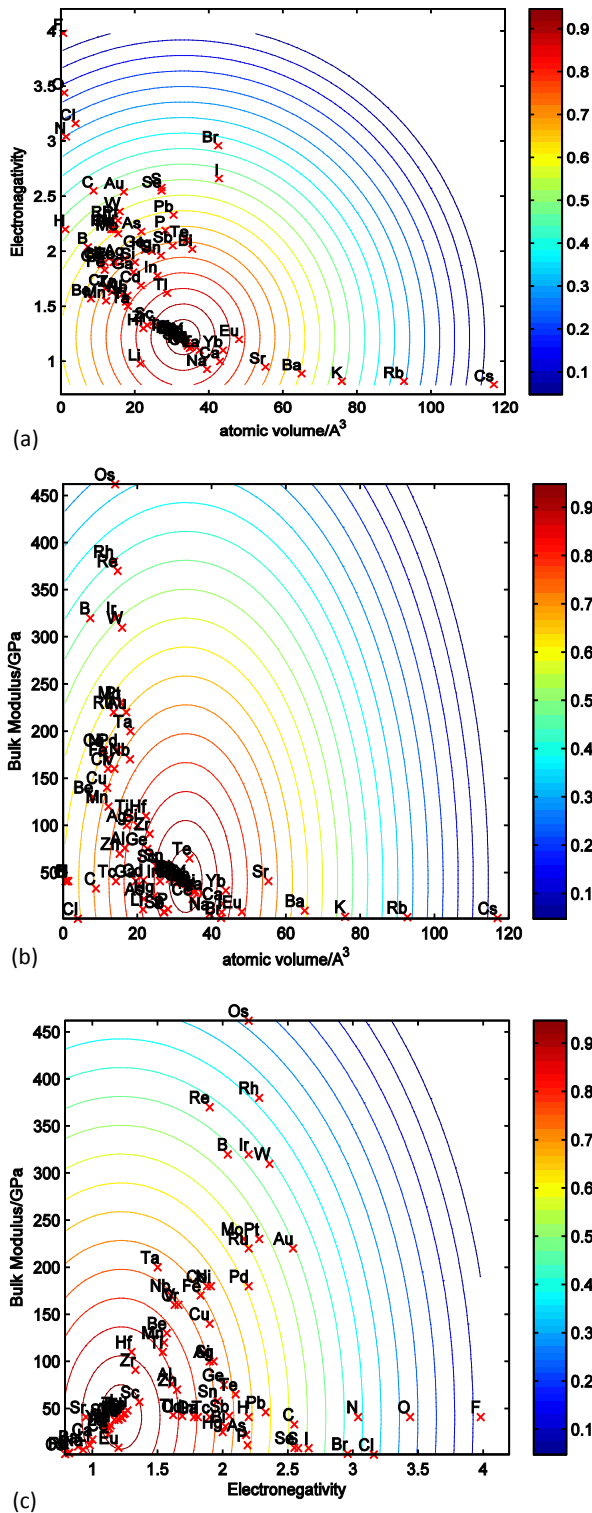


Figure 4.4.2:

The elements and their YSI values projected onto planes with different property pairs: (a) atomic volume and electronegativity; (b) atomic volume and bulk modulus; and (c) electronegativity and bulk modulus. The atomic volume, electronegativity and bulk modulus are obtained from the website [82, 83]. Yttrium is located in the centers of all three ellipses.

Table 4.4.1:

Statistical data of YSI values. Y has the maximum values of YSI and Cs the minimum one.

Average YSI	0.66
Maximum YSI	1
Minimum YSI	0
Top ten elements	Y, Gd, Tb, Dy, Sm, Ho, Er, Nd, Tm, Pr
Lowest ten elements	Cs, F, O, Os, Cl, N, Rb, Rh, W, Re
Top five of non-RE	Na, Ca, Zr, Tl, Li

the I_1 SFE in Mg alloys since our model is based on an approximation of three correlation relationships. Ca was found to decrease the elongation of Mg up to concentration of 3 wt% [87]. Salahshoor *et.al.* performed a more dense set of experiments on samples with 0-4.0 wt% of Ca [88]. They found Ca could increase the elongation of Mg by 4% up to ≈ 0.5 wt% and thereafter decrease the elongation for higher concentration. To the best knowledge of us, there are, unfortunately, no experimental data for Mg-Na alloys available. But the solubility of Na in Mg is very low (apparent in Mg-Na phase diagram), therefore Na is not promising solute of interest. Zirconium has a too low solubility in Mg, so it is used as a grain refiner by grain boundary pinning [89]. No data for Mg-Tl alloys are available. Li is a well-known solute that can improve the ductility of Mg [16, 17, 18, 19] by enhanced activity of $\langle c+a \rangle$ dislocations [19], which is consistent with our prediction.

There are no bulk modulus data available for H, N, O, F, Ga, Tc and In. The bulk modulus term in the YSI determination is then ignored by setting $B_i=B_Y$, $B_Y=41$ GPa. However, it was found that these elements possess rather low YSI values, i.e. low similarity to Y (see Table 4.4.1) and we do not expect them to reduce the energy of I_1 SF in Mg.

We show the relation between the I_1 SFE and YSI for 18 Mg alloys in Figure 4.4.3. The SF energies decrease with increasing YSI. At low YSI values the I_1 SFE decreases slowly then the falling slope of the I_1 SFE increases and finally the I_1 SFE drops very sharply for high YSI values. This relation can be fitted to a rather simple exponential function as

$$\gamma = 42.11(1 - \exp\{4(YSI - 1)\}) \quad (\text{mJ/m}^2) \quad (4.4.2)$$

which is characterized by a high Pearson's correlation coefficient $r=0.93$. The exponential character of the trend in Fig. 4.4.3 is partly due to the logarithmic relation between the bulk moduli and the I_1 stacking fault energies. In our definition of YSI, we use linear functions to describe this relation in order to keep YSI as a concept of generalized distance between the properties of elements. By using this exponential function we can easily find the lowest values of the YSI parameter that leads to a reduction of the I_1 SFE in Mg alloys (compared with elemental Mg). This critical value is associated with the I_1 stacking fault energy of pure Mg (19.47 mJ m^{-2}), and the threshold value of YSI is 0.84

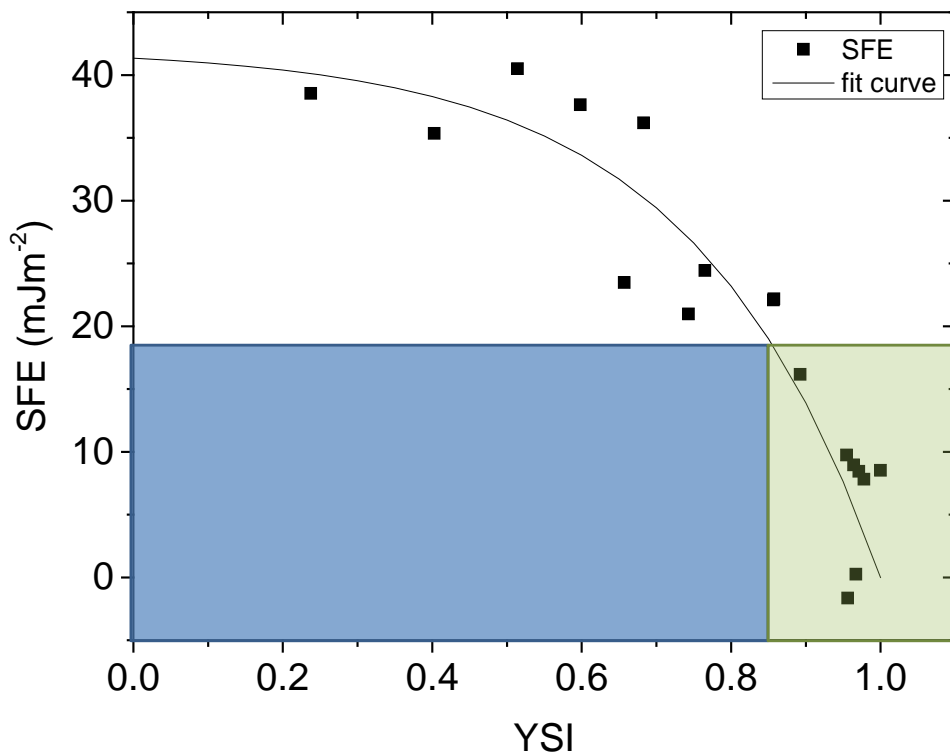


Figure 4.4.3:

Relationship between computed I₁SFE and YSI parameter with the horizontal border line indicating the I₁ stacking fault energies value in pure Mg. Elements decreasing the I₁ stacking fault energy in Mg alloys are in the part with a greenish background.

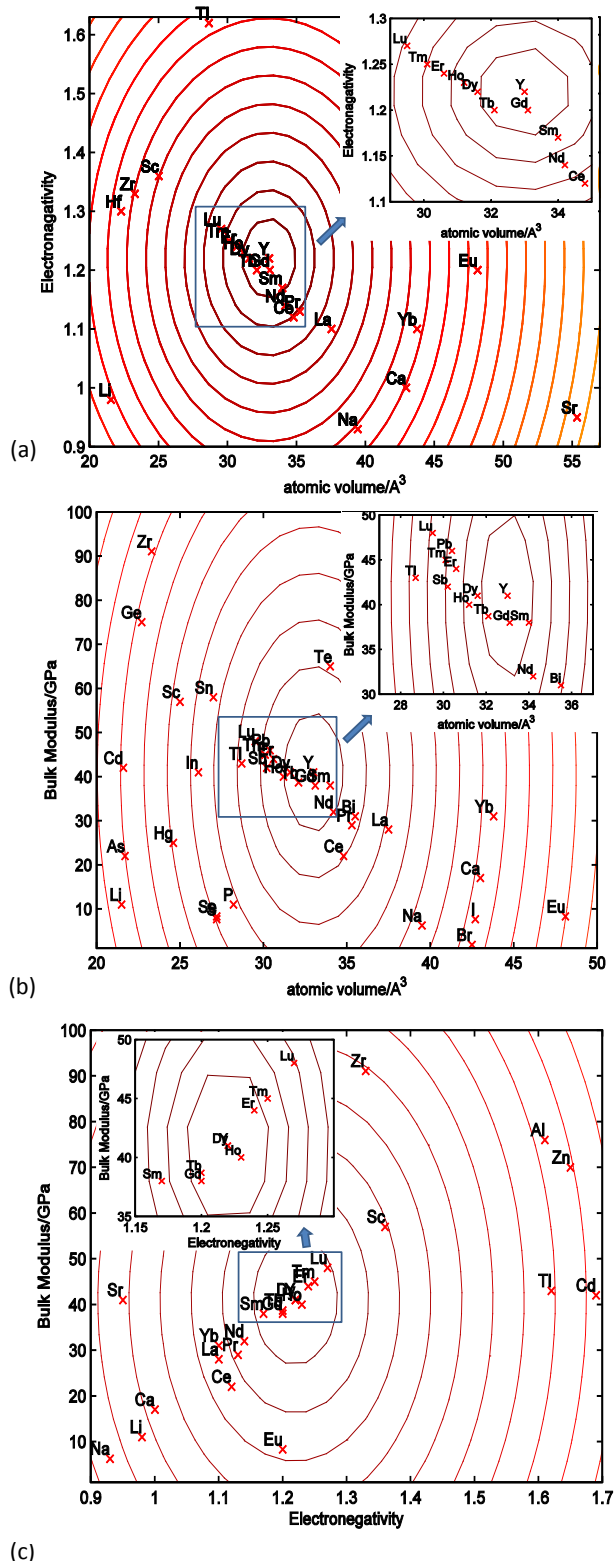


Figure 4.4.4:

The elements and their YSI values projected onto plane with different property pairs: (a) atomic volume and electronegativity; (b) atomic volume and bulk modulus; and (c) electronegativity and bulk modulus. Compared to Figs. 4.4.2, these sub-figures are primarily visualizing the most promising elements with $\text{YSI} \geq 0.84$.

($\approx 1 - 1/4 \ln 2$). In Figure 4.4.3, the shadow area is below the line of 19.47 mJm^{-2} . The elements which are possible to reduce I_1 stacking fault energies are expected in the greenish area. For elements with $\text{YSI} \geq 0.84$, their locations in the properties space are shown in Figure 4.4.4 (some elements with YSI smaller than 0.84 are also shown). Our findings represent sever fundamental limitation in any search for alternative solutes ductilizing magnesium (there is only a single non-rare-earth element, Li, having a $\text{YSI} \geq 0.84$). Consequently, alloy-design strategies should be rather focused on higher-order alloying concepts (e.g., ternary or quaternary Mg-alloys) that can potentially provide a necessary reduction of the I_1 SFE as yttrium by combining more than one solute. In order to pave this way, we below extend our searching space of solutes from binaries to ternaries and demonstrate the performance of our searching method.

4.5 Conclusions

We have used quantum-mechanical calculations in order to find relations between the I_1 stacking fault energy and fundamental atomic properties of elemental solutes. Our analysis showed that the I_1 SFE is (i) strongly anti-correlated to the atomic volume (Pearson's correlation coefficient $r = -0.97$), (ii) correlated to the electronegativity ($r = 0.95$) and (iii) logarithmically related to the bulk modulus ($r = 0.90$). Based on these relations, we propose an yttrium similarity index (YSI) that combines all three criteria and rationalizes the complexity of prediction of I_1 stacking fault energies. As this new numerical indicator matches excellently the trends of quantum-mechanically computed stacking fault energies for Mg_{15}X with 18 different solutes, we evaluate it for 76 elements from the periodic table of the elements. The newly introduced numerical quantifier allows the identification of the most promising solutes in a fast manner and without computationally expensive and lengthy *ab initio* calculations. We have found only one non-rare-earth element, lithium, that we predict to have reduced I_1 stacking fault energies. Seeing this limited options in the case of binary Mg alloys, we propose that the newly introduced parameter is used in high-throughput theory-guided rapid prototyping of new multi-component Mg-alloys with increased ductility. This will be thoroughly discussed in the next chapter.

Such numerical methods, e.g. yttrium similarity index, are useful and efficient when considering the contradiction between materials science and material engineering. Materials scientists have been struggling to develop different theories to explain the underlying mechanism of observed phenomena in experiment. Although our insight of these materials phenomena are always deepening, application of such theories to direct design of new materials is still not very practical. The predictability and computational efficiency of materials science theories is far from satisfactory. On another hand, our demand of novel materials is increasing all the time, where we need some direct (e.g.. the possible solute candidates for magnesium with enhanced ductility as structural materials) in order to save money and time in experiment. This is the contradiction between materials science and materials engineering.

Actually it's not necessary to understand all the underlying mechanisms before we start to design new materials. If we know the inputs and outputs of a system, we can treat the mechanism as a black box. We can adjust the inputs in order to obtain wanted outputs. For example, a general rule that similar elements usually has similar chemical effect in a system. We do not need to know the mechanism immediately, but we can apply the rule in our materials design. Even though there is no solid theoretical foundation, the rules usually work effectively. Such rules can direct us in our search for solutes and thus in design of new materials.

2850

Chapter 5

Ternary Mg Alloys

In this chapter we will extend the yttrium similarity index of single solute to that of two solutes in order to design ternary Mg alloys.

5.1 Introduction

In the last two chapters we have systematically discussed binary Mg alloys. The Mg-Y alloys are found to be more ductile than pure Mg and importantly the alloys have comparative strength with pure Mg. Following this idea that similar solute has similar chemical effect, all other potential elements that have same or similar crystallographic structure with yttrium (hcp or double hcp structure) are considered in our electronic structure calculation. All these considered rare-earth (RE) elements turn out to be able to reduce I_1 stacking fault energy which indicates these elements are able to ductilize magnesium [37]. For some of these RE solutes, e.g. Gd, Dy, Tb and Er, tensile tests support our theoretical finding. But the RE element resources are limited and environmental problems arise from mining these resources, therefore such elements are rather expensive, application of these elements in Mg industry is not economic. Bearing the idea that similar elements have similar effect in mind, we continue to search all the possible ductile solutes in the Periodic Table of Elements. The employed criterion is yttrium similarity index (YSI), which is based on the correlations between stacking fault energy and electronegativity, bulk modulus and atomic volume. The application of YSI again identifies the RE elements (except Eu) to be the most similar solutes with yttrium. Except RE elements other elements cannot reduce I_1 stacking fault energy. Therefore we cannot find a suitable non-RE element that can ductilize Mg in the framework of binary Mg alloys.

The conclusions of our previous investigation direct us to the design of ternary Mg alloys. So we need a new criterion that allow us to select combination of two solutes. Here we inherit the idea of YSI and extend the index of one solute to that of two.

5.2 Computational Methodology

5.2.1 Yttrium Similarity Index of Ternary Mg Alloys

The YSI concept introduced above (see Eq. 4.4.1) is based on comparing selected materials properties of individual solutes to corresponding materials properties in yttrium and it is a figure of merit assign to individual solutes. In case of Mg-based ternaries containing two different solutes at once, we would like to assign a single numerical evaluator to a pair of solutes, each of them having different elemental materials properties. In order to extend the YSI concept to higher-order alloys, we propose to use solute-ratio weighted averages of materials parameters of individual solutes, i.e., averages of materials properties of both individual participating solutes in case of two solutes with an equal atomic-percent amount (see the cases discussed below). In the ternary case we then re-write the YSI formula for a single solute (Eq.4.4.1) and extend the YSI concept to ternary Mg alloys as follows

$$YSI_{ij} = 1 - \sqrt{w_v(v_{ij} - v_Y)^2 + w_e(\nu_{ij} - \nu_Y)^2 + w_B(B_{ij} - B_Y)^2}, i \neq j. \quad (5.2.1)$$

$i, j = \text{H, Li, Be, ... Bi}$, using averaged materials parameters, the atomic volume $v_{ij} = (v_i + v_j)/2$, the bulk modulus $B_{ij} = (B_i + B_j)/2$, and the electronegativity $\nu_{ij} = (\nu_i + \nu_j)/2$, weighted by the same weights w_v , w_e and w_B as in Eq.4.4.1. The total number of solutes pairs (containing two different solutes) is $76 \times 75/2 = 2850$.

5.2.2 Computational Detail

Density functional theory (DFT) [46, 47] calculations of I₁SFE were carried out using the projector augmented wave (PAW) method [90] and electronic exchange-correlation effects were described by the generalized gradient approximation (GGA) [54] as implemented in the Vienna Ab-initio Simulation Package (VASP) [70, 72]. A cut-off plane wave energy of 350 eV was used for all calculations. In order to keep the similar solute concentration of both solutes in ternary Mg alloys with that of binary alloys, a 36-atom supercell 3x3x4 (Mg34-X1-X2) is applied, in which there are 34 Mg atoms, one solute X1 and one solute X2. Solute X1 is positioned at one corner of the supercell, and solute X2 at its center (Figure 5.2.1). The advantage by doing so is, such a configuration is seemingly most possible to keep the symmetry of hcp, since our YSI is based on hcp Mg alloys. The Brillouin zones were sampled using dense Gamma-point-based 7x7x6 k-point meshes to ensure the convergence of total energies within 1 meV per atom. Atoms were relaxed until the energy converged to 10^{-4} eV. The lattice parameters of pure Mg is employed in the calculation of ternary Mg alloys, which is a good approximation proved by our test.

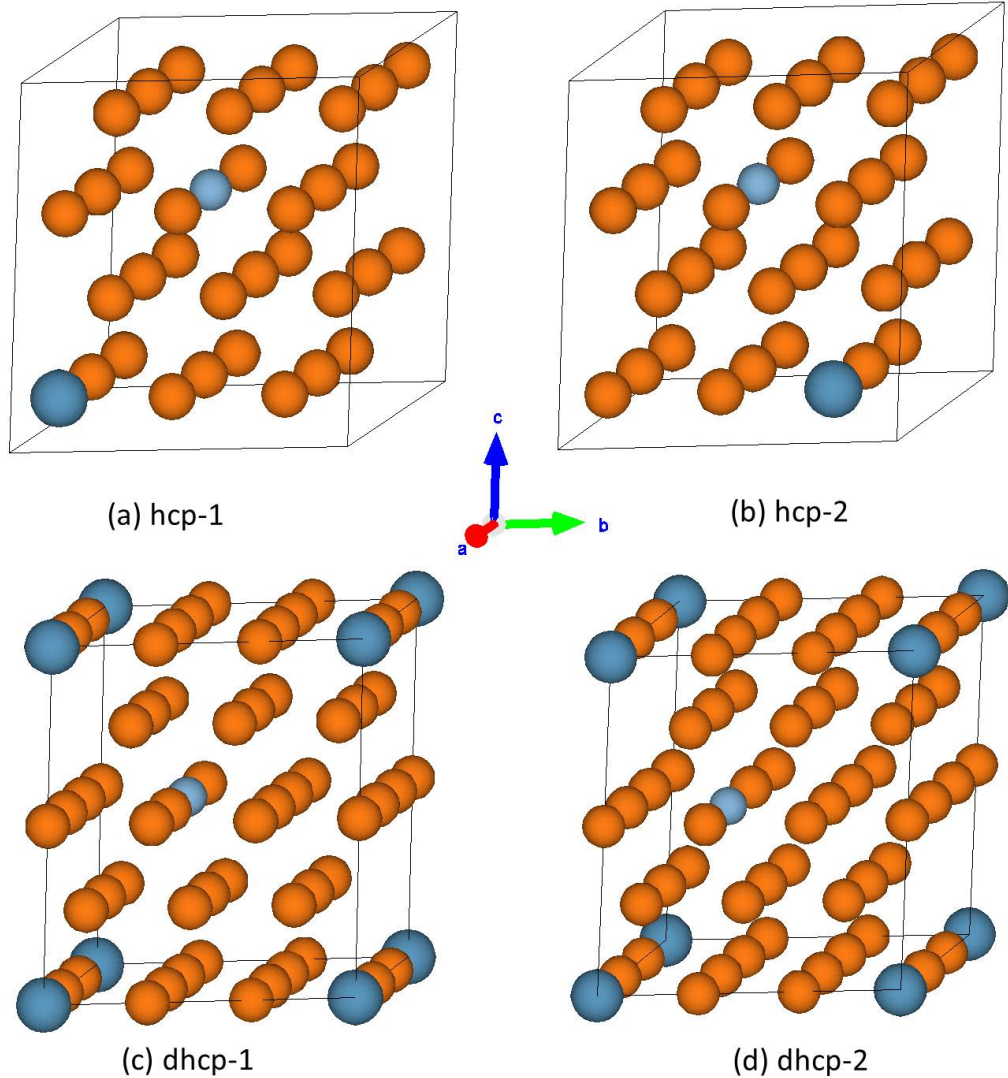


Figure 5.2.1:

Schematic figure of supercells for hexagonal-close-packed (hcp) structure and double hcp (dhcp). In both hcp and dhcp there are two symmetrically nonequivalent sites for solutes X1 and X2. For convenience of description in the following text, these supercells are denoted as hcp-1, hcp-2, dhcp-1 and dhcp-2.

Table 5.3.1:

The statistic data of YSI values computed for Mg-based ternaries. Since our aim is to find non-RE solute pair that have high YSI, only data for pairs that do not contain RE elements are listed.

YSI	No. of combination
$0.85 \leq \text{value} < 0.95$	122
$0.95 \leq \text{value} < 0.98$	11
$0.98 \leq \text{value}$	0

5.3 Results

5.3.1 Yttrium Similarity Index

Applying Eq.5.2.1, the YSI values of all 2850 combinations were calculated. Since our aim is to find out solute pair that consists of non-RE elements but is also able to reduce I_1 SFE like yttrium, the RE elements are excluded from our discussion of results below. No non-RE candidates possess YSI higher than 0.98. The statistic data of the matrix are listed in Tab. 5.3.1. There are 133 non-RE solute pairs with YSI larger than 0.85. These solute candidates along with their YSI are listed in Table 5.3.2 ordered according their YSI value from the lowest to the highest. The last 11 solute pairs in Table 5.3.2 have the YSI larger than 0.95. Except (Sr,Zn), ten of these pairs contain either Ca, Na or Al. Among these ten pairs, five solute pairs contain Ca, three include Na and two contain Al.

5.3.2 Ab Initio Computed Stacking Fault Energies

In order to determine the I_1 SFEs of 11 solute pairs from the ANNNI model, quantum-mechanical calculations have been used to determine the energies of supercells that are shown in Figure 5.2.1. As shown in Figure 5.2.1 there are two non-equivalent configurations for the two solutes X1 and X2 in both hcp and dhcp supercells. For the four supercells we denote the total energies as E_{hcp-1} , E_{hcp-2} , E_{dhcp-1} and E_{dhcp-2} . According to the ANNNI model, there are four different values of the I_1 SF energies, which we, for the sake of simplicity, denoted as "11", "12", "21", and "22" in Table 5.3.3. The notion "11" means that the stacking fault energy is calculated from the energy difference $E_{dhcp-1} - E_{hcp-1}$; in case of "12" the I_1 SFE is computed as $E_{dhcp-1} - E_{hcp-2}$; for "21" it is as $E_{dhcp-2} - E_{hcp-1}$; and lastly in case of "22" it is as $E_{dhcp-2} - E_{hcp-2}$. The "22" of (Zr,Ca) is negative, because the energy of the (Zr,Ca) pair in case of the dhcp-2 supercell is even lower than that in case of the hcp-2 supercell (that would indicate that the stacking faults would form very easily, in fact spontaneously, if allowed by surrounding crystal matrix in this particular case).

At $T = 0$ K, the solutes choose their lattice position so as to minimize the energies of

Table 5.3.2:

Yttrium similarity index (YSI) for 133 non-RE solute pairs with YSI larger than 0.85. Among them 11 solute combinations possess YSI larger than 0.95.

Solute	YSI								
Fe,K	0.851	Te,Ca	0.872	Bi,Li	0.888	Sr,Cr	0.903	Sr,Be	0.928
Ba,Ge	0.852	Zr,Li	0.873	Sb,Ca	0.888	Sb,Na	0.904	Tc,Sr	0.929
Sb,Sr	0.852	Ba,Si	0.873	Ba,H	0.888	V,Ca	0.904	Zn,Na	0.930
Zn,K	0.853	Sr,Co	0.874	Nb,Sr	0.890	Ge,Ca	0.904	Ga,Na	0.930
Cu,K	0.857	Tl,Zr	0.875	Cr,Na	0.890	Ba,Cr	0.905	Ga,Ca	0.932
Cr,K	0.857	Fe,Na	0.875	Ta,Ca	0.891	Tc,Ca	0.905	Sr,Ti	0.932
Cd,Li	0.859	P,Na	0.875	Sr,Li	0.891	Ag,Sr	0.906	Sr,Mn	0.937
Pb,Na	0.859	Ba,Nb	0.875	Ba,Fe	0.891	Ag,Ca	0.907	In,Ca	0.938
Ta,Ba	0.860	Ba,Cd	0.875	Te,Na	0.892	Hf,Sr	0.908	Ba,Be	0.939
Ni,Na	0.861	Sn,Sr	0.876	Ta,Na	0.892	Ag,Na	0.908	Al,Na	0.939
Ni,Ca	0.862	Bi,Ca	0.876	Tl,Sr	0.893	Hg,Na	0.908	Ti,Na	0.941
Co,Na	0.864	Te,Li	0.876	Na,Li	0.894	Ba,Al	0.909	Zn,Ca	0.942
Ca,Na	0.864	Fe,Ca	0.877	Bi,Na	0.894	Mn,Na	0.909	In,Na	0.947
Hf,Li	0.864	As,Na	0.877	Cr,Ca	0.896	Nb,Ca	0.910	Hf,Na	0.949
Ca,P	0.864	In,Li	0.877	Sr,Cu	0.897	Sn,Ca	0.910	Ti,Ca	0.950
Ba,Zr	0.864	K,H	0.880	Ca,Be	0.897	Nb,Na	0.910	Cd,Na	0.951
Co,Ca	0.865	Ba,Ga	0.881	In,Sr	0.898	Ca,Li	0.912	Sr,Al	0.952
Hf,Ba	0.866	Hg,Sr	0.881	Ba,V	0.898	Zr,Sr	0.913	Ca,Al	0.952
Mn,K	0.867	Cu,Na	0.881	Tc,Na	0.899	Ge,Na	0.913	Tl,Ca	0.952
Sr,As	0.867	Ba,Ni	0.882	Ba,Ti	0.899	Ba,Zn	0.915	Cd,Ca	0.954
Sn,Li	0.867	Cu,Ca	0.884	Ba,Cu	0.899	Ca,Si	0.916	Sr,Zn	0.956
Sb,Li	0.869	Na,Be	0.884	V,Na	0.899	Mn,Ca	0.922	Hf,Ca	0.958
Sr,H	0.869	Ba,Co	0.884	Hg,Ca	0.901	Si,Na	0.922	Zr,Na	0.962
Tl,Hf	0.869	Sr,Fe	0.885	Ba,Tc	0.901	Sn,Na	0.923	Tl,Na	0.966
Ta,Sr	0.870	Ba,Ag	0.885	Tl,Li	0.901	Ba,Mn	0.925	Zr,Ca	0.973
As,Ca	0.871	Sr,Ge	0.885	Sr,Si	0.901	Sr,Ga	0.925		
Sr,Ni	0.871	K,Be	0.887	Sr,V	0.903	Cd,Sr	0.928		

Table 5.3.3:

The computed I_1 SFEs of ternary Mg alloys with solutes consisting of only non-RE elements with YSI larger than 0.95. The unit of the numbers is mJm^{-2} . The last column contains a verbal evaluation of the potential of listed solute pairs with respect to the reduction of I_1 SFE in Mg-based ternaries.

Solutes (i, j)	YSI	11	12	21	22	MIN	MEAN	potential
Ti,Ca	0.950	26.9	16.4	17.8	7.3	7.3	17.1	very promising
Cd,Na	0.951	18.2	21.1	20.0	23.3	18.2	20.7	promising
Sr,Al	0.952	9.1	18.2	17.5	26.2	9.1	17.8	very promising
Ca,Al	0.952	14.6	19.3	20.0	24.7	14.6	19.6	promising
Ca,Al ^a	0.952	13.8	18.6	19.3	24.0	13.8	18.9	very promising
Tl,Ca	0.952	15.6	18.9	16.7	20.0	15.6	17.8	very promising
Cd,Ca	0.954	15.6	20.0	18.6	22.9	15.6	19.3	promising
Sr,Zn	0.956	13.1	18.9	18.6	24.7	13.1	18.9	very promising
Hf,Ca	0.958	31.3	15.6	17.1	1.5	1.5	16.4	very promising
Zr,Na	0.962	24.7	16.0	17.5	8.7	8.7	16.7	very promising
Tl,Na	0.966	17.5	19.3	17.8	19.3	17.5	18.6	very promising
Zr,Ca	0.973	40.0	27.7	7.3	-5.1	-5.1	17.5	very promising

^a computed with the optimized lattice parameters $a = 3.199\text{\AA}$, $c/a = 1.626$ (see the text for details).

dhcp and hcp structures. The corresponding computed values of I_1 SFE are in Table 5.3.3 in the "MIN" column (the "MIN" values are the smallest values among "11", "12", "21" and "22" combinations of energies). At finite temperature, the solutes have non-zero probabilities to occupy also other positions, not only those that minimize the energy. Assuming, for the sake of simplicity, an equal probability for all crystal sites, we compute an average value of the four I_1 SFE and list them in Table 5.3.3 in the column marked "MEAN". We expect realistic values would be somewhere between "MIN" and "MEAN" values. Therefore, we sort the solute pairs as follows. If both "MIN" and "MEAN" values are smaller than 19.47 mJm^{-2} (the value found in the elemental Mg), the corresponding solute pair is considered as "very promising" with respect to reducing the I_1 SFE in Mg ternaries. If only one of these two quantities is smaller than 19.47 mJm^{-2} , the solute combination is considered as "promising" to reduce I_1 SFE and if both quantities are larger than 19.47 mJm^{-2} , the candidate is evaluated as "not promising" to reduce I_1 SFE.

Following this criterion, eight solute combinations, (Ti,Ca), (Sr,Al), (Ti,Ca), (Sr,Zn), (Hf,Ca), (Zr,Na), (Ti,Na) and (Zr,Ca), are very promising with respect to reducing the I_1 SFE in Mg alloys. Three other solute pairs, (Cd,Na), (Ca,Al) and (Cd,Ca), are promising to reduce I_1 SFE of Mg. As seen, no solute pair was found "not promising", i.e. not able to reduce the I_1 SFE in Mg alloys. That means an excellent agreement between our YSI-based prediction and benchmarking I_1 SFE quantum-mechanical calculations. The stacking fault energies discussed above were computed using lattice constants of pure Mg ($a = 3.1886 \text{ \AA}$, $c/a = 1.6261$). To assess an error introduced by this way of calculating the energies, the lattice constants of Mg-(Al,Ca) were fully optimized and found equal to $a = 3.199 \text{ \AA}$, $c/a = 1.626$. The subsequent use of the optimal lattice constants in our quantum-mechanical calculations resulted in the stacking fault energies of Mg-(Al,Ca) altered by only $0.7\text{--}0.8 \text{ mJm}^{-2}$ and the use of the Mg lattice constant is thus shown to be a good approximation. It should be nevertheless noted that our approach does not include more complicated thermodynamic aspects of ternary alloys that are related to e.g. ternary phase diagrams where intermetallics and other phases appear and influence, for example, the solubility of solute(s) or thermodynamics stability of ternary alloys.

5.4 Conclusions

We extend our YSI analysis to ternary Mg alloys assuming that the physical properties of two solutes can be represented by average values of their individual materials parameters (atomic volume, the electronegativity and the bulk modulus). Out of 2850 solute combinations tested, 133 solute pairs (not including any rare-earth elements) possess YSI larger than 0.85 and 11 of them have YSIs higher than 0.95. Subsequent quantum-mechanical calculations of these 11 solute combinations resulted in lower I_1 stacking fault energies (compared with the elemental Mg) in case of all of them. Our proposed YSI parameter thus proved to be 100 % effective in identifying promising solute candidates.

Importantly, the newly introduced numerical quantifier allows the identification of the most promising solutes in a very fast manner and without computationally expensive and lengthy *ab initio* calculations.

Chapter 6

Generalized Stacking Fault Energies in Mg and Mg-Y Alloys

We proposed that I_1 stacking faults are nucleation sources for non-basal dislocations, which explains the increased density of non-basal dislocations and the enhanced ductility of Mg-Y alloys (see Figure 3.3.3). In the last three chapters we thoroughly discussed the properties of I_1 stacking fault in Mg and Mg alloys; in the following two chapters we will discuss dislocations. More specifically, the present chapter will investigate so-called generalized stacking fault energies of Mg and Mg-Y alloys, which are indication of dislocation mobility.

6.1 Introduction

The poor room temperature ductility of magnesium, which is caused by limited available deformation mechanisms, can be improved by addition of yttrium through higher activity of non-basal slip systems and thus texture weakening [6]. Nucleation and mobility energies of dislocations, both perfect and dissociated dislocations, are related to the stable and unstable stacking fault energies which are available via atomistic calculations.

Different slip mechanisms in Mg have been intensively studied both experimentally [6, 91, 19] and theoretically [92, 93, 94]. Theoretical studies generally focused on calculating so-called generalized stacking fault energy (GSFE) profiles obtained by sliding one half of a crystal over the second half across a given glide plane. As shown by Vitek [28], these energy profiles are closely connected with the motion of dislocations and the plasticity of materials in general. GSFEs of important planes along different slip directions were calculated employing both density functional theory (DFT) and the embedded atom method (EAM) for pure Mg [95, 40, 96, 26, 80]. It was shown, for example, that maxima occurring along GSFE profiles, so-called unstable stacking fault energies (USFEs), determine the behavior of slip modes and thus the ductility in fcc metals [97]. Our study is motivated by the fact that rather little is known about GSFEs in Mg-Y alloys, especially in the case of non-basal deformation modes (see e.g. Table 1.2.1). Therefore, we study and compare the influence of Y additions on the behavior of both

basal and non-basal slip systems. Our aim was to provide results that will contribute to the understanding of enhanced room temperature ductility of Mg-Y alloys [6] and to the design of ductile Mg-based materials in future.

6.2 Computational Methodology

6.2.1 Concept of Gamma Surface

Employing theoretical methods, slip deformation modes can be studied by calculating generalized stacking fault energies (gamma surface) [28]. Key properties of slip deformation modes such as the Peierls barrier as well as stacking fault energies can be deduced from the gamma surface. We determine the generalized stacking fault energies by incrementally shifting the upper half crystal along the slip direction (Figure 6.2.1) and calculating the total energy of the system as a function of the applied shift vector. Specifically, the shift vector \vec{f} is usually defined by

$$\vec{f} = x\vec{a} + y\vec{b} \quad (0 \leq x \leq 1, 0 \leq y \leq 1). \quad (6.2.1)$$

Here x and y define two shift coordinates varying from 0 to 1. \vec{a} and \vec{b} are two vectors in the plane defined usually by the shortest lattice distances and they are not parallel (or mathematically, $\vec{a} \neq \lambda\vec{b}$, λ is a scalar-quantity constant). In the case of the gamma surface for the $\{11\bar{2}2\}$ plane, two perpendicular vectors ($1/3\langle 11\bar{2}3 \rangle$ and $\langle 10\bar{1}0 \rangle$) are selected on the plane. With continuous changes of x and y , all possible configurations of stacking fault can be accessed which correspond to the shadowed area in Figure 6.2.2. For each vector \vec{f} , the energy of the generalized stacking fault is defined by [28]

$$\gamma_{GSF} = \frac{E - E_0}{A}. \quad (6.2.2)$$

Here E_0 is the energy of the perfect lattice, E the energy of the crystal with defect, A is the area of shifting crystallographic plane. E varies with changes of x and y . The total energy of a perfect crystal (represented by a supercell) usually has the lowest energy compared to that of supercell with a generalized stacking fault, so $\gamma > 0$. gamma surface of a plane can be employed to search for stable stacking faults, which are represented by local minimal points. A stable stacking fault indicates the dissociation a perfect dislocation and a more stable configuration than perfect dislocation exists. The dissociated dislocation can avoid the high energy barrier along its Burgers vector during its moving which reduces its Peierls stress and increases its mobility.

In order to facilitate the consideration of a single stacking fault, and so allow us to reduce the required supercell size, we added the applied shift vector to the lattice vector along the glide plane normal (in our case the glide plane normal is denoted as the z-direction). The original supercell and its image together actually construct a new supercell with a single stacking fault. For the minimization after each incremental shift, atomic positions are constrained along the inclusive dimensions of the glide plane, but atoms can reduce

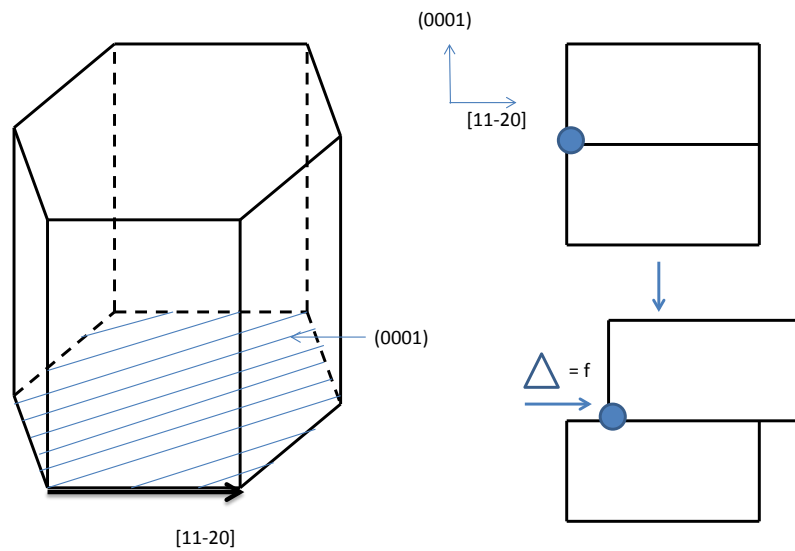


Figure 6.2.1:

Schematic figure of a stacking fault with slip plane $\{0001\}$ and slip direction $\langle 11\bar{2}0 \rangle$. The left figure shows the geometrical location of the slip system. The right figure is a scheme of the shifting process which is controlled by vector \vec{f} . The cross section of the gamma surface on this plane in this direction is calculated.

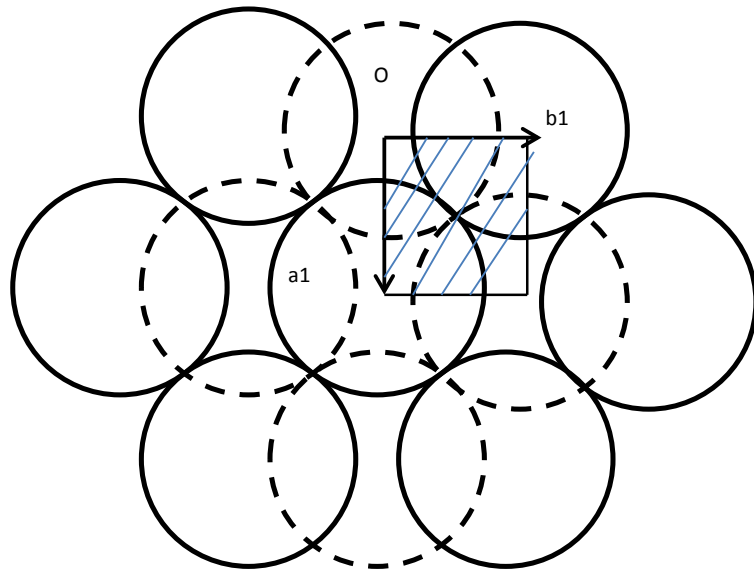


Figure 6.2.2:

Schematic view of possible \vec{f} vectors in plane $\{hkl\}$. All points in the shaded area correspond to \vec{f} vectors of the generalized intrinsic stacking faults on the plane.

the total energy of the system by relaxing in the direction perpendicular to the studied glide plane.

In order to eliminate any spurious interactions between the interface (i.e. the glide plane) and its periodic images, the supercell size must be sufficiently large. We therefore converged the GSFE with respect to the number of atomic planes parallel to the fault plane. For example, in order to determine an optimum number of atomic planes for the $\{0001\}\langle 11\bar{2}0 \rangle$ slip system, supercells with 2, 4, 6, 8 and 12 layers along the $\langle 11\bar{2}0 \rangle$ direction, the z-direction (parallel to the plane normal), were used to calculate GSFEs (Figure 6.2.3). The GSFE difference between 6-layer (2x2x6, 24 atoms) and 12-layer (2x2x12, 48 atoms) supercells is less than 1%. Therefore, supercells with more than six layers are considered large enough. All the tests are performed on pure Mg. In our case, on top of convergent condition, a 48-atom supercell was employed to obtain a realistically low Y concentration. Converged supercell sizes of all the other slip systems considered were determined similarly (see Table 6.2.1). In calculations of Mg-Y alloys, one Mg atom is replaced by a Y atom on the gliding plane. Therefore, in Mg_{55}Y the concentration of Y is 1.82 at.% and 2.08 at.% for Mg_{47}Y in all the other considered slip systems.

Table 6.2.1:

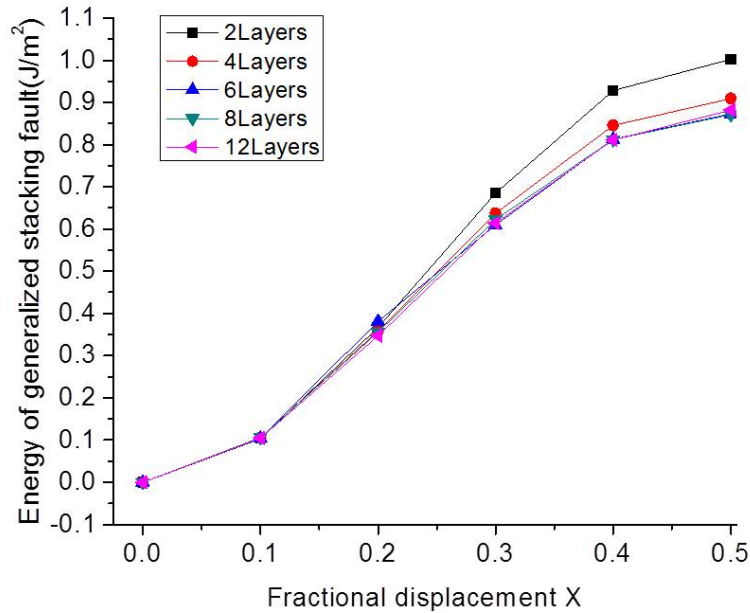
DFT-computed lattice parameters for pure Mg and Mg-Y alloys with different stoichiometries with corresponding supercell sizes and slip systems.

Stoichiometry	a (Å)	c/a	Supercell Size	Atom No.	Slip Systems
Mg	3.1886	1.6261	2x2x12 (14)	48(56)	all slip systems (56 for $\{10\bar{1}0\}\langle 11\bar{2}0 \rangle$)
Mg_{55}Y	3.2004	1.6253	2x2x14	56	$\{10\bar{1}0\}\langle 11\bar{2}0 \rangle$
Mg_{47}Y	3.2064	1.6215	2x2x12	48	$\{0001\}\langle 11\bar{2}0 \rangle$, $\{0001\}\langle 10\bar{1}0 \rangle$, $\{10\bar{1}1\}\langle 11\bar{2}0 \rangle$, $\{11\bar{2}2\}\langle 11\bar{2}3 \rangle$

6.2.2 Computational Detail

Our DFT calculations were carried out using the projector augmented wave method [98] and the electronic exchange-correlation effects were described by the generalized gradient approximation [54] as implemented in the Vienna Ab initio Simulation Package (VASP) [70, 72]. A plane wave cut-off energy of 350 eV is used for both pure Mg and the Mg-Y alloys. The Brillouin zone was sampled using dense gamma-centered scheme k-point meshes that were chosen to ensure a convergence of the total energy to within 1 meV per atom. Atomic relaxations were performed until the energy converged to 10^{-7} eV. To test our computational parameters, we have calculated the lattice parameters of pure Mg. The results, $a = 3.1886$ Å and $c/a = 1.6261$ (Table 6.2.1), are in good agreement with experimental data suggesting $a = 3.21$ Å and $c/a = 1.624$ [99].

As a secondary method, GSFEs are also calculated by molecular dynamics modeling using EAM potential developed by H. Sheng [34] in the framework of open source code LAMMPS [100]. Some calculation detail is listed in Table 6.2.2. In the supercells some


Figure 6.2.3:

The calculated cross section of gamma surface using a series of supercells with different numbers of atomic layers ($\{0001\}\langle 11\bar{2}0 \rangle$).

of Mg atoms are replaced by Y atoms, keeping the concentration of Y same with the respective DFT supercells, as well as the planar concentration of Y on the plane. In the large supercells used in EAM the Y atoms are evenly distributed. The accuracy of EAM potential are firstly benchmarked against the more accuracy DFT and then used to calculate the gamma surface of the non-basal slip system.

Table 6.2.2:

Different stoichiometries with corresponding supercell sizes and slip systems in EAM calculations.

Slip Systems	Supercell Size	Atom No.
$\{0001\}\langle 11\bar{2}0 \rangle$	2x2x6	48
$\{10\bar{1}0\}\langle 11\bar{2}0 \rangle$	2x2x7	56
$\{0001\}\langle 10\bar{1}0 \rangle$	4x4x6	192
$\{10\bar{1}1\}\langle 11\bar{2}0 \rangle$	4x4x3	192
$\{11\bar{2}2\}\langle 11\bar{2}3 \rangle$	12x6x2	1728

6.2.3 Development of Mg-Y EAM Potential

Empirical potentials provide a means of exploring the physics of systems of atoms on length- and time-scales currently inaccessible to more computationally expensive *ab initio* techniques. Such potentials seek to approximate the energy of a system of atoms, and the forces between those atoms, as a classical function of the relative positions of the

Table 6.2.3:

Physical properties of Mg predicted by the present EAM model and other EAM models. E_c is the cohesive energy, E_ν^f is the relaxed vacancy formation energy, E_ν^m is the migration energy of vacancy, ^aRef. [24], ^bRef. [25], ^cRef. [101], ^dRef. [102], ^eRef. [103], ^fRef. [104], ^gaverage of basal plane and prism plane surface energies, ^hfirst-principles results as a part of this work, ⁱRef. [105].

	Exp./Theory	present model	Sun ^a	Liu ^b
a (Å)	3.21 ^c	3.21 (300 K)	3.206	3.206
c/a ratio	1.623 ^c	1.623	1.623	1.623
E_c (eV/atom)	1.510 ^d	1.510	1.516	1.516
C_{11} (GPa)	59.5 ^e	59.5	69.6	61.8
C_{12} (GPa)	26.1 ^e	25.7	25.3	25.9
C_{13} (GPa)	21.8 ^e	20.9	16	21.9
C_{33} (GPa)	61.6 ^e	62.7	69.5	67.5
C_{44} (GPa)	16.4 ^e	15.8	12.8	18.2
E_ν^f (eV)	0.59 \approx 0.89 ^b	0.62	0.88	0.87
E_ν^m (eV)	0.39 ^b	0.47	0.64	
E_{surface} (mJ/m ²)	680 ^f	480 ^g		495
$E_{\text{fcc-hcp}}$ (eV)	0.011 ^b , 0.007 ^h	0.006	0.012	0.015
$E_{\text{bcc-hcp}}$ (eV)	0.028 ^b	0.024	0.014	0.018
T_m (K) (hcp)	923 ⁱ	850		

atoms treated as point particles. The key attributes of such potentials are: i) The level of physics they aim to capture, i.e. whether they are simple pair potentials or attempt to capture many-atom effects and whether they are functions only of atomic separations or also of bond angles; ii) The nature of the functions used in the fitted potential, which is to say, the extent to which those functions have a (perhaps physically-motivated) prescribed form versus being, say, piecewise spline fitted; and iii) The data to which those functions are fitted, which may be energies and elastic properties from experiment and *ab initio* calculations or individual atomic forces from *ab initio* calculations for a set of atomic configurations. The key issue for empirical potentials, especially when they are to be used to explore systems beyond the reach of *ab initio*, is their *transferability*: it is one thing to correctly reproduce the properties to which a potential is fitted and quite another to provide accurate predictions of "unseen" data.

In this study, an embedded-atom-method (EAM) interatomic potential was developed to describe the Mg-Y system, which has the following formalism [61, 106]: $E_{\text{tot}} = \sum_{i,j} \phi(r_{ij}) + \sum_i F(n_i), \rho(r_{ij})$ where $n = \sum_j$, and $\phi(r)$, $\rho(r)$, and $F(n_i)$ are the pair, density, and embedding functions. In this work, the three functions $\phi(r)$, $\rho(r)$, and $F(n_i)$ are represented with quintic spline interpolations [107]. We used 15 equidistant spline knots for both the pair and the density functions (in the fitting range of 0.5 - 6.5 Å), and 6 spline knots for the embedding function. For the Mg-Y binary system, a total

Table 6.2.4:

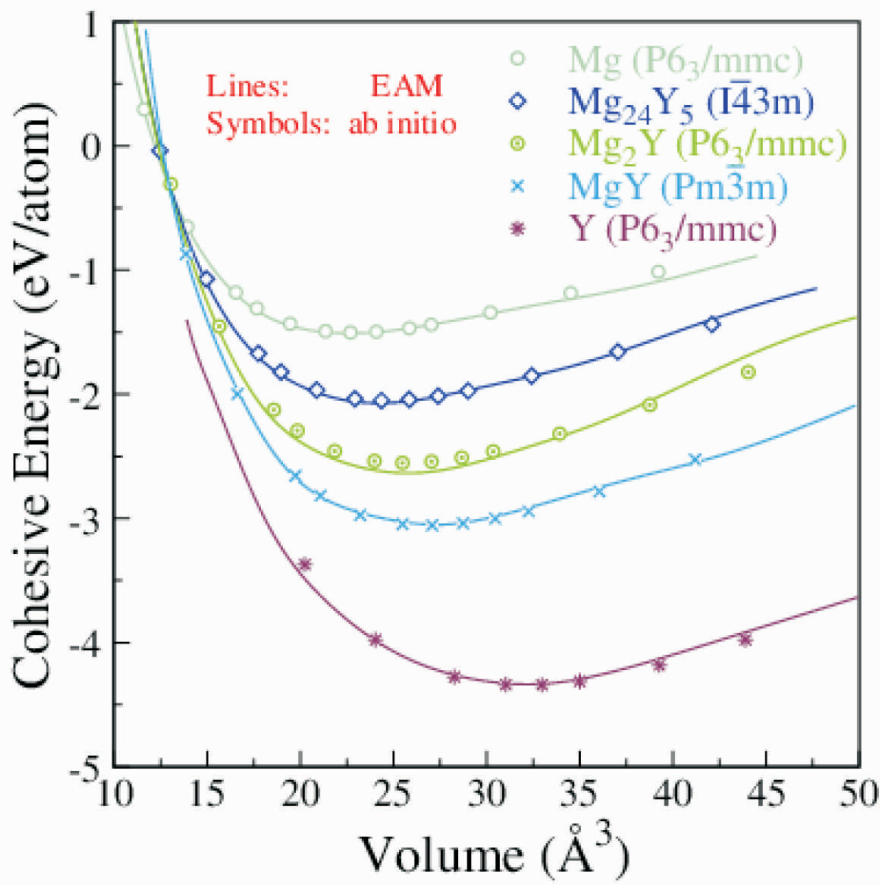
Physical properties of Y predicted by the present EAM model and other EAM models. E_c is the cohesive energy, E_ν^f is the relaxed vacancy formation energy, E_ν^m is the migration energy of vacancy, ^cRef. [101], ^dRef. [102], ^eRef. [103], ^fRef. [104], ^hfirst-principles results as a part of this work, ⁱRef. [105], ^jRef. [108], ^kRef. [109].

	Exp./Theory	Present model	Hu ^j	Baskes ^k
a (Å)	3.65 ^c	3.65 (300 K)	3.65	3.65
c/a ratio	1.57 ^c	1.57	1.57	1.57
E_c (eV/atom)	4.37 ^d	4.37	4.37	
C_{11} (GPa)	77.9 ^e	78.3		
C_{12} (GPa)	28.5 ^e	26.8		
C_{13} (GPa)	21.0 ^e	21.9		
C_{33} (GPa)	76.9 ^e	77.2		
C_{44} (GPa)	24.3 ^e	21.7		
E_ν^f (eV)	1.50 ^f	1.70	1.22	1.25
E_ν^m (eV)		0.66	0.59	
E_{surface} (mJ/m ²)	1125 ^f	830	868	625
$E_{\text{fcc-hcp}}$ (eV)		-0.03		
$E_{\text{bcc-hcp}}$ (eV)	0.022 ^h	0.020		
T_m (K) (hcp)	1796 ⁱ	1810		

number of 83 parameters were fitted.

The EAM potential was developed based on the force-matching method [107, 110] as implemented in the POTFIT package [111]. To this end, a first-principles database was first established to provide a coarse-grained potential energy surface (PES) of the Mg-Y system. The database was constructed to encompass a wide range of atomic configurations, including all crystalline phases in this alloy system, as well as their derivative structures such as defects, crystal equations of state, deformation paths, melting and cooling trajectories etc. In addition to six crystal structures of Mg and Y (i.e., hcp, bcc, fcc, 9R, diamond and sc structures), three crystallographic types of Mg-Y intermetallic compounds [112] are considered in this work, including Mg_{24}Y_5 ($I\bar{4}3m$), Mg_2Y ($P6_3/mmc$) and MgY ($Pm3m$).

Ab initio molecular dynamics simulation [113] was conducted to obtain liquid structures as well as their trajectories along the heating and cooling processes. Altogether, around 700 configurations (with each configuration typically containing 100 atoms) were selected and subjected to density-functional theory (DFT) calculations using the pseudopotential and plane wave method implemented in the Vienna Ab-initio Simulation Package (VASP) [70, 72]. The derived potential energy surface (the potential energy and stress tensors of each configuration, forces on each atom and elastic constants of two reference structures) was further modified to match the experimental values of the lattice parameter and cohesive energy of Mg and Y, and was then utilized to parameterize

**Figure 6.2.4:**

Comparison of *ab initio* and EAM calculations of the cohesive energies of Mg-Y alloys at different volumes.

the EAM potential for the Mg-Y system. A similar practice can be found in Ref. [107]. During potential fitting, *ad hoc* EAM potentials were employed in classical MD to probe deeper potential basins on the PES, with new configurations added to the previously built potential database for a new round of EAM parameterization. Several iterations were performed until the self-consistency between *ab initio* and EAM calculations was reached.

To demonstrate the overall performance of the as-developed EAM potential, we compare the present EAM model with previous models for Mg and Y in terms of the accuracy of predicting a set of materials properties, as shown in Tables 6.2.3 and 6.2.4. The performance of the EAM potential for Mg-Y alloys can be seen from Figure 6.2.4, where the equations of state of the crystalline phases derived from the EAM model and the *ab initio* treatment are provided. The cohesive energies of the intermetallic compounds, with tabulated lattice parameters, are listed in Table 6.2.5 for comparison. The general agreement between EAM and *ab initio* calculations is satisfactory. The as-developed EAM potential is available from Ref. [114].

Table 6.2.5:

Cohesive energies of Mg-Y intermetallic compounds predicted by EAM and *ab initio* calculations. The lattice parameters are taken from Ref. [112].

Compound	Lattice Parameter	Cohesive energy ab initio (eV/atom)	Cohesive Energy EAM (eV/atom)
MgY (<i>Pm3m</i>)	$a = 3.790 \text{ \AA}$	3.06	3.05
Mg ₂ Y (<i>P6₃/mmc</i>)	$a = 6.037 \text{ \AA}$ $c = 752 \text{ \AA}$	2.55	2.64
Mg ₂₄ Y ₅ (<i>I</i> ₄ <i>3m</i>)	$a = 3.790 \text{ \AA}$	2.05	2.07

6.3 Results and Discussion

Our quantum-mechanical and atomistic calculations of GSFE profiles include five slip systems for both pure Mg and Mg-Y. Specifically, we consider the three $\langle a \rangle$ -type slip systems ($\{0001\}\langle 11\bar{2}0 \rangle$, $\{10\bar{1}0\}\langle 11\bar{2}0 \rangle$ and $\{10\bar{1}1\}\langle 11\bar{2}0 \rangle$), and the second order pyramidal slip system ($\{11\bar{2}2\}\langle 11\bar{2}3 \rangle$), which contributes to shear deformation out of the basal plane, as well as the $\{0001\}\langle 10\bar{1}0 \rangle$ slip system, which is related to the intrinsic stacking fault I_2 (I_2 SF). The I_2 stacking fault is formed when the $[0001]$ -vector is altered by addition of $1/3\langle 10\bar{1}0 \rangle$. If we assign letters A, B and C to three possible stacking configurations of (0001) planes (in analogy to the stacking order of (111) planes in face-centered cubic lattices), the normal alternating hcp stacking ($\dots ABABABAB \dots$) is locally changed to an ($\dots ABABCACA \dots$) stacking (see Figure 1.2.1). Thus the influence of Y on the energetics of the I_2 stacking fault can be studied by GSFE calculations. This part of our study represents a continuation of our previous experimental and theoretical study on the I_1 intrinsic stacking fault (see [37] for details).

6.3.1 The Three Primary Slip Systems

The GSFEs of $\{0001\}$ along $\langle 11\bar{2}0 \rangle$ calculated by DFT and EAM methods are plotted as function of shifted displacement for pure Mg and Mg-Y alloy and shown in Figure 6.3.1. The USFEs based on DFT calculations for pure Mg and Mg-Y alloys (Mg_{47}Y , 2.08 at.% Y) are 0.276 J/m^2 and 0.214 J/m^2 respectively, with an obvious energy reduction of 0.062 J/m^2 or 22.5% of 0.276 J/m^2 . This is in agreement with previous DFT results [95]. Obviously reductions of USFEs are also seen in curves by EAM calculations. For pure Mg and Mg-Y alloy of the same Y concentration, the USFEs are 0.233 J/m^2 and 0.190 J/m^2 , with reduction of 0.043 J/m^2 or 18.5 % of 0.233 J/m^2 . Therefore, by addition of Y in pure Mg the reduced GSFE trends calculated by both methods are consistent. The two GSFE curves of Mg-Y alloy are generally in good agreement as a whole, with a maximum difference of less than 12 % (of 0.214 J/m^2). However, the GSFE curves of pure Mg are quite different (about 15 % of 0.276 J/m^2), especially at the point corresponding to USF. But both GSFE curves of Mg-Y alloy calculated by the two methods are lower than that of pure Mg, and thus can be concluded that the addition of

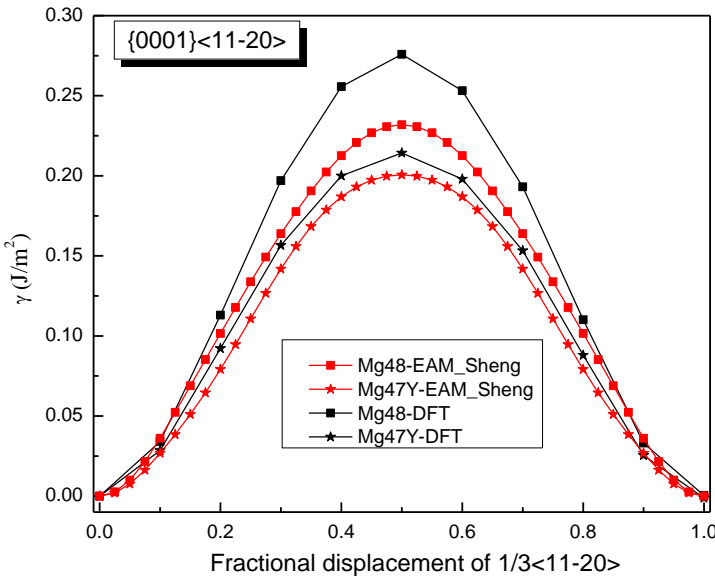


Figure 6.3.1:

GSFE profiles of Mg and Mg alloys as a function of the shifted displacement along the $\langle 11\bar{2}0 \rangle$ direction in the basal plane. The USF corresponds to a shifted displacement of $0.5a$ where a is the lattice parameter of pure Mg or $Mg_{47}Y$.

Y in pure Mg reduces the USFE and thus the energy barrier which dislocations moving on the slip system must overcome.

The GSFE curves of prismatic slip system $\{10\bar{1}0\}\langle 11\bar{2}0 \rangle$ for pure Mg and Mg-Y alloy ($Mg_{55}Y$, 1.82 at.% Y) are shown in Figure 6.3.2. In the four GSFE curves, there is only one global maximum respectively, which corresponds to the USF of the studied slip system. Based on DFT calculation, the USFE of Mg-Y alloy (0.128 J/m^2) is much lower than that of pure Mg (0.231 J/m^2) with strong energy decrease of 44.6 % (nearly half of 0.231 J/m^2). The USFE of pure Mg is in good agreement with previous DFT results [26, 80]. In the framework of EAM, the calculated energy decrease is also very significant, namely 34.7 % of the USFE in pure Mg (0.190 J/m^2). Actually, except the decrease of USFE, strong global reduction of GSFEs is observed by alloying Y in pure Mg from the calculated results either by employment of DFT or EAM method. The GSFEs of pure Mg calculated by DFT and EAM are relative different, but that of Mg-Y alloy are in very good agreement. No matter calculated based on DFT or EAM, the GSFEs of pure Mg are higher than Mg-Y alloy.

The GSFEs of pyramidal slip system $\{10\bar{1}1\}\langle 11\bar{2}0 \rangle$ are also calculated for pure Mg and Mg-Y alloy ($Mg_{47}Y$, 2.08 at.% Y) based on DFT and EAM (see Figure 6.3.3). The GSFE curves of Mg-Y alloy based on DFT and EAM match well. Same case like $\{0001\}\langle 11\bar{2}0 \rangle$ and $\{10\bar{1}0\}\langle 11\bar{2}0 \rangle$, the GSFEs of pure Mg based on the two methods are relatively different. However, no matter if calculated by DFT or EAM GSFEs in Mg-Y alloy are lower than those of pure Mg. The DFT-based USFEs of Mg-Y alloys are seen a reduction

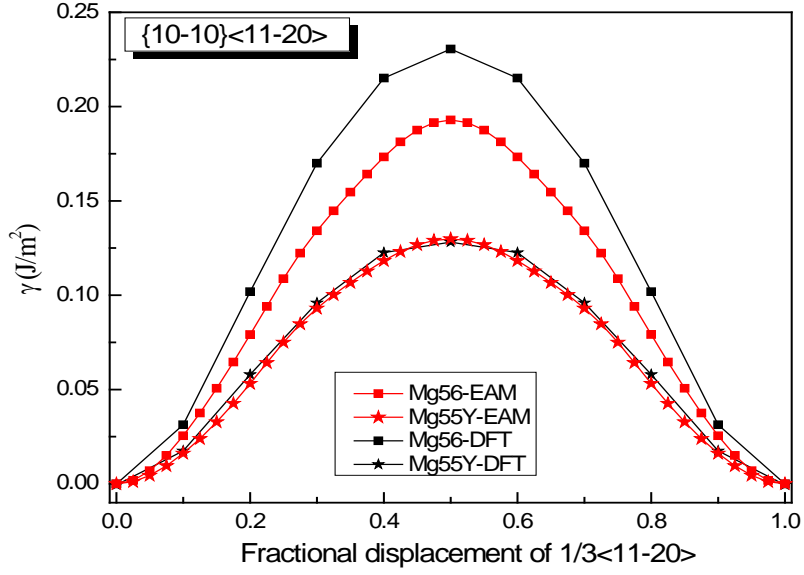


Figure 6.3.2:

GSFE profiles of Mg and Mg alloys as a function of the shifted displacement along the $\langle 11\bar{2}0 \rangle$ direction in the prismatic plane. The USF corresponds to a shifted displacement of $0.5a$ where a is the lattice parameter of pure Mg or Mg_{55}Y .

of 9 % of 0.343 J/m^2 (USFE of pure Mg). This reduction calculated based on EAM is about 3.7 % of 0.323 J/m^2 (USFE of pure Mg). The DFT-based USFE of pure Mg is in very good agreement with previous DFT results [40, 80].

The GSFE profiles of $\{0001\}\langle 10\bar{1}0 \rangle$ for pure Mg and Mg-Y alloy (Mg_{47}Y , 2.08 at.%) are plotted as functions of shifted displacement in Figure 6.3.4. The four curves show similar characteristics with a local minimum (shifted displacement about $\frac{1}{3}$) and a global maximum (about $\frac{2}{3}$) at the same position. The local minimum corresponds to the stacking configuration $\dots \text{ABABABACBCBC} \dots$, which is exactly I_2 SFE. The I_2 SFEs of pure Mg and Mg-Y alloy calculated by DFT are 0.037 J/m^2 and 0.030 J/m^2 respectively, with energy reduction of 0.007 J/m^2 (19 % of 0.037 J/m^2). By EAM the values are 0.017 J/m^2 (pure Mg) and 0.008 J/m^2 (Mg-Y alloy). Compared to I_2 SFE of pure Mg, that of Mg-Y alloy decreases 0.009 J/m^2 (53 % of 0.017 J/m^2). The maximum corresponds to the unstable stacking fault $\dots \text{ABABABBCBCBC} \dots$. The two adjacent B layers cause an energy increase, which can be weakened by reconstruction of the second B layer. The maximal GSFEs calculated by DFT for pure Mg and Mg-Y alloy are 0.475 J/m^2 and 0.445 J/m^2 , with energy difference 0.030 J/m^2 . From EAM the calculated USFEs are 0.444 J/m^2 and 0.413 J/m^2 , with energy difference 0.031 J/m^2 . As a whole, no matter if for pure Mg or Mg-Y alloys the GSFEs calculated by EAM are slightly lower than that by DFT. However, the trend of GSFE reduction by alloying Y is same. The DFT-based local maximum and minimum GSFEs (I_2 SFE) are quantitatively in excellent agreement with published results [95, 26, 80]. The experimental value of I_2 SFE of Mg-3.wt.-%-Y

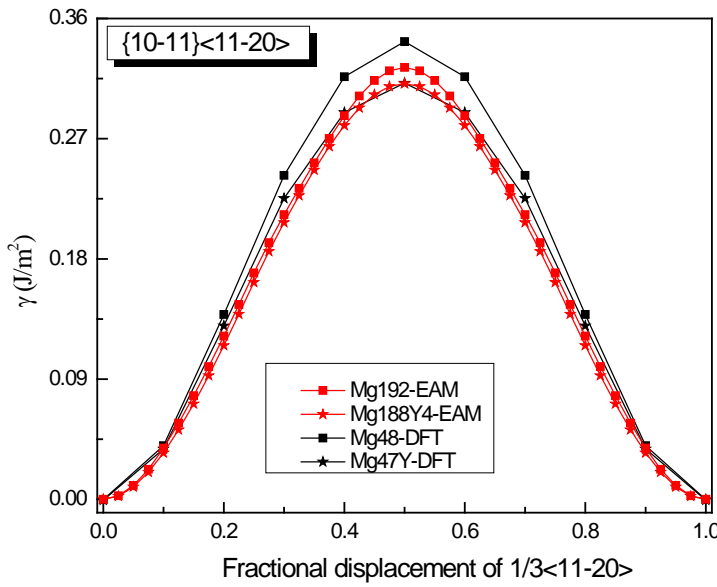


Figure 6.3.3:

GSFE profiles of Mg and Mg alloys as a function of the shifted displacement along the $\langle 11\bar{2}0 \rangle$ direction in the pyramidal plane. The USF corresponds to a shifted displacement of $0.5a$ where a is the lattice parameter of pure Mg or $Mg_{47}Y$.

is $1.5 \pm 0.5 \text{ mJ/m}^2$ [37], which is smaller than pure Mg (19.2 mJ/m^2). Therefore the experimental and theoretical trends are qualitatively same.

6.3.2 GSF of Non-basal Plane Slip

As one of the most important non-basal slip systems, $\{11\bar{2}2\}\langle 11\bar{2}3 \rangle$ is studied. The GSFEs of the slip system are calculated for pure Mg and Mg-Y ($Mg_{47}Y$, 2.08 at.%) based on the two methods (see Figure 6.3.5). The GSFE curves share similar shapes, in which there are two maximums (one local maximum and one global maximum) and one local minimum at different positions. The local minimum corresponds to a stable stacking fault (SSF). The stable stacking fault energy (SSFE) of Mg-Y alloy (0.293 J/m^2) calculated by DFT is lower than that of pure Mg (0.318 J/m^2). However, the SSFE calculated by EAM method of Mg-Y (0.268 J/m^2) is higher than that of pure Mg (0.276 J/m^2). The maximum of GSFE (USFE) calculated either by DFT or EAM is larger for Mg-Y alloy than for pure Mg. Previous DFT results [40] are slightly smaller than our data.

Before the shifted displacement is larger than half of the length of Burgers vector ($\sim \frac{1}{2}\frac{1}{3}\langle 11\bar{2}3 \rangle$) the DFT-based GSFEs of Mg-Y alloy are lower than that of pure Mg; after this, the GSFEs of pure Mg are lower than Mg-Y alloy. The EAM results show similar profile, but the starting position ($\sim \frac{1}{3}\frac{1}{3}\langle 11\bar{2}3 \rangle$) where GSFEs of Mg-Y alloy are globally larger than pure Mg is different. The GSFEs calculated by both DFT and EAM methods

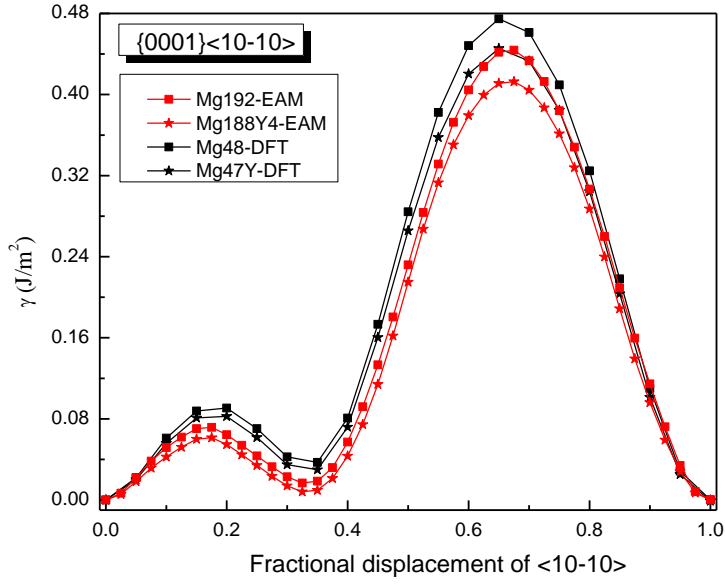


Figure 6.3.4:

GSFE profiles of Mg and Mg alloys as a function of the shifted displacement along the $\langle 10\bar{1}0 \rangle$ direction in the basal plane. The total shifted displacement is $\frac{\sqrt{3}}{3}a$ where a is the lattice parameter of pure Mg or Mg₄₇Y. The stable stacking fault energy (SSFE) and USFE correspond to shifted displacements of $\frac{1}{3}a$ and $\frac{2}{3}a$ respectively.

are in relative good agreement.

The DFT-based shallow minima (0.020 J/m² for pure Mg and 0.015 J/m² for Mg-Y alloy) indicate a dissociation of perfect dislocation $\frac{1}{3}\langle 11\bar{2}3 \rangle$ following the reaction

$$\frac{1}{3}\langle 11\bar{2}3 \rangle = \lambda \frac{1}{3}\langle 11\bar{2}3 \rangle + (1 - \lambda) \frac{1}{3}\langle 11\bar{2}3 \rangle \quad (\lambda \simeq 0.4). \quad (6.3.1)$$

where λ is a constant coefficient for a dissociation reaction. When $\lambda = 0.4$, the rows of each atoms in the adjacent two gliding planes seem to be more regular than any other cases (see Ref. [115], Fig. 7 0.6 < $c + a$ >).

The dissociation was found by other authors but with different λ values. In Ref. [40], based on DFT and EAM (Liu potential [25]) $\lambda = 0.33, 0.25$ respectively for pure Mg. In [115] based on EAM under the condition of in-plane atomic relaxations $\lambda = 0.5$. The different λ values are due to the different calculation methods and specific conditions. By dissociation the non-basal dislocations are more energetically stable in the form of two partial dislocations with the stacking fault region inbetween. Smaller SSFEs will generally produce longer separated distance between partials and thus larger width of SSFs. By alloying Y in Mg, the SSFE reduces. Therefore in Mg-Y alloys, the SSFs of larger width are more energetically favorable to form. More detail about the SSF of $\{11\bar{2}2\}\langle 11\bar{2}3 \rangle$ will be further described in the next section.

The computational results of the five slip systems together with published data are summarized in Table 6.3.1. The maximal GSFEs of the three primary basal slip systems

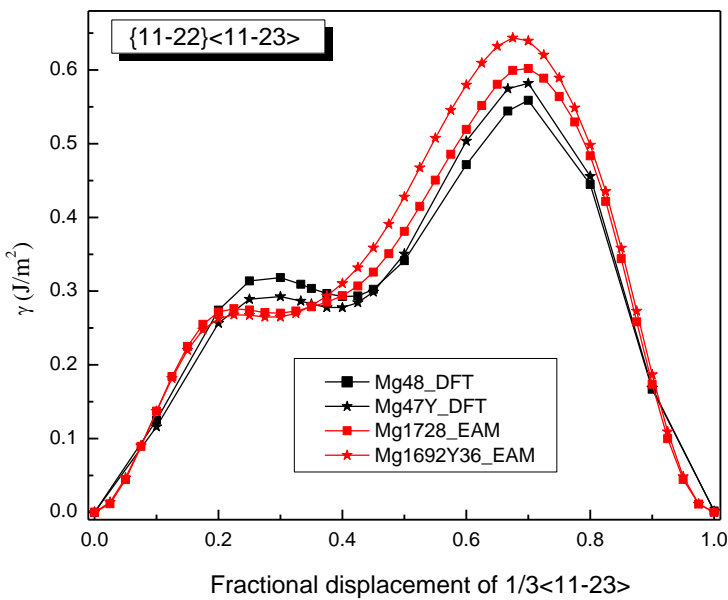


Figure 6.3.5:

GSFE curves of Mg and Mg alloys as a function of the shifted displacement along the $\langle 11\bar{2}3 \rangle$ direction in the non-basal plane $\{11\bar{2}2\}$. The total shifted displacement is the length of Burgers vector $\frac{1}{3}\langle 11\bar{2}3 \rangle$. The SSFE, local USFE and global USFE correspond to shifted displacements of about 0.4, 0.25 and 0.7 calculated by DFT, and about 0.3, 0.22 and 0.7 by EAM.

indicate that highest Peierls stress is expected for $\frac{1}{3}\langle 11\bar{2}0 \rangle$ dislocations on pyramidal plane and lowest on prismatic plane. The ratios SSFE/USFE are calculated for slip systems $\{0001\}\langle 10\bar{1}0 \rangle$ and $\{11\bar{2}2\}\langle 11\bar{2}3 \rangle$ and listed in Table 6.3.1. When SSFE/USFE decreases the deformation mechanism by partial dislocations is favoured. It is seen from the Table 6.3.1 that SSFE/USFE decreases for $\{0001\}\langle 10\bar{1}0 \rangle$ after alloying Y in pure Mg, which means the deformation mechanism by partial dislocations is more energetically inclined. For $\{11\bar{2}2\}\langle 11\bar{2}3 \rangle$, there is no clear change of SSFE/USFE, so it is hardly to conclude the influence of alloying Y.

Table 6.3.1:

DFT- and EAM-calculated values of USFE, SSFE and SSFE/USFE₁ of pure Mg and Mg-Y alloys for the selected 5 slip systems. USFE₁ is the local maximum of GSFE, and USFE₂ is the global maximum.

Supercell	DFT	EAM							
		SSFE	USFE ₁	USFE ₂	SSFE/USFE ₁	SSFE	USFE ₁	USFE ₂	SSFE/USFE ₁
1-Mg	-		0.276, 0.288 ^a	-	-	-	0.233	-	-
1-Mg-Y	-		0.214, 0.248 ^a	-	-	-	0.190	-	-
2-Mg	0.037, 0.036 ^a , 0.034 ^c , 0.039 ^d	0.091, 0.092 ^a , > 0.092 ^c , 0.101 ^d	0.475	0.41, 0.39 ^a , < 0.37 ^c , 0.39 ^d	0.017, 0.044 ^c	0.072, 0.082 ^c	0.444	0.24, 0.54 ^c	
2-Mg-Y	0.030, 0.025 ^a	0.083, 0.071 ^a	0.445	0.36, 0.35 ^a	0.008	0.061	0.413	0.13	
3-Mg	-	0.231, 0.473 ^a , 0.218 ^c , ~ 0.225 ^d	-	-	-	0.266, 0.170 ^c	-	-	
3-Mg-Y	-	0.128, 0.558 ^a	-	-	-	0.124	-	-	
4-Mg	-	0.343, 0.310 ^b , ~ 0.340 ^d	-	-	-	0.323, 0.226 ^b	-	-	
4-Mg-Y	-	0.312	-	-	-	0.311	-	-	
5-Mg	0.298, 0.236 ^b	0.318, 0.243 ^b	0.559, 0.485 ^b	0.94, 0.97 ^b	0.270, 0.198 ^b	0.276, 0.206 ^b	0.602, 0.505 ^b	0.98, 0.96 ^b	
5-Mg-Y	0.278	0.293	0.582	0.95	0.265	0.268	0.644	0.989	

The energies in the table are in J/m². The numbers before the name of material systems denote different slip systems. 1- $\{0001\}\langle 11\bar{2}0 \rangle$, 2- $\{0001\}\langle 1\bar{1}00 \rangle$, 3- $\{10\bar{1}0\}\langle 11\bar{2}0 \rangle$, 4- $\{10\bar{1}1\}\langle 11\bar{2}0 \rangle$, 5- $\{11\bar{2}2\}\langle 11\bar{2}3 \rangle$. The EAM data from Ref. [26] are also results of Sun EAM. The data taken from Ref. [80] are the results of density functional theory.

^a Ref. [95];

^b Ref. [40];

^c Ref. [26];

^d Ref. [80].

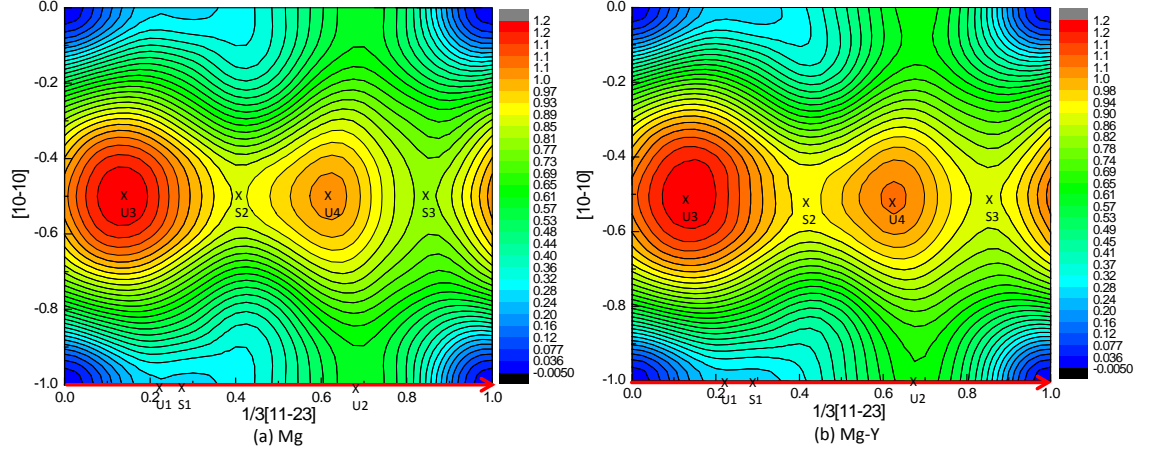


Figure 6.3.6:

Projection of $\{11\bar{2}2\}$ plane gamma surface with 0.040 J/m^2 isolines for the EAM potential developed by H. Sheng. The $\frac{1}{3}\langle 11\bar{2}3 \rangle$ Burgers vector and the minimum energy path are same (see red arrows). S1, S2 and S3 indicate the three SSFs, and U1, U2, U3 and U4 the two USFs. The GSFE of U1, U2 and S1 are USFE_1 , USFE_2 and SSFE calculated based on EAM in Table 6.3.1. For U3, U4, S2 and S3, the corresponding GSFEs are (a) 1.218 J/m^2 , 1.033 J/m^2 , 0.889 J/m^2 and 0.807 J/m^2 ; (b) 1.226 J/m^2 , 1.075 J/m^2 , 0.930 J/m^2 and 0.888 J/m^2 .

As shown in Figure 6.3.1-6.3.5, the EAM potentials developed for Mg and Mg-Y by H. Sheng are quite reliable, which will be employed for the calculation of gamma surface of non-basal plane in the following section.

6.3.3 Gamma Surface of Non-basal Plane

In order to better understand $\langle 11\bar{2}3 \rangle$ non-basal slip process and SSF on $\{11\bar{2}2\}$ plane, the GSFEs for pure Mg and Mg-Y alloy based on EAM are calculated and drawn as projection of gamma surfaces (see Figure 6.3.6). There is no obvious difference between the projections of gamma surfaces for pure Mg and Mg-Y alloy. In both Figures 6.3.6 (a) and (b), the lowest-energy slip path is a line section along $y = 0$, which is exactly the Burgers vector $\frac{1}{3}\langle 11\bar{2}3 \rangle$. On the path there are two maximums (U1, U2) and one minimum (S1) without consideration of the point where $x = 0$ and $y = 0$. This can be seen more clearly in Figure 6.3.5. There are also two minima (S2, S3) in the gamma surface, but the values are much higher than S1. So S1 is the most stable stacking fault on $\{11\bar{2}2\}$ plane, which corresponds to reaction Eq. 6.3.1 of dislocation dissociation. The calculation of gamma surface for pure Mg was performed in Ref. [115] (see Fig. 4 of the Ref. [115]) and quantitatively agrees with our results.

Along $[10\bar{1}0]$ there exists a curved minimum path across S3 point. The fact that the GSFE at S3 point is even higher than that at U2 show this minimum path is not energetically favorable.

6.4 Conclusions

Using DFT and newly developed EAM potential, we present GSFE profiles for five selected slip systems in both pure Mg and Mg-Y alloys. The results of the three $\langle a \rangle$ slip systems show that the USFEs decrease upon Y additions in Mg. From the slip system $\{0001\}\langle 10\bar{1}0 \rangle$ the I_2 SFEs for pure Mg and Mg-Y are also obtained, and the I_2 SFE of Mg-Y alloy is lower than that computed for pure Mg. Importantly, the generalized stacking fault energies associated with displacement along the $\langle 11\bar{2}3 \rangle$ direction in the non-basal plane $\{11\bar{2}2\}$ are initially lower but with increasing displacement become higher than those of Mg. This is in contrast to the basal slip systems, for which the Mg-Y energies are consistently lower than for Mg. Lastly, after careful testing of our newly developed EAM Mg-Y potential, the generalized stacking fault energies for all glide systems within the $\{11\bar{2}2\}$ plane are calculated using this potential and the GSFE profiles are visualized as a two-dimensional gamma surface. Our theoretical study has been complemented by an experimental TEM analysis that confirmed our theoretical prediction that the I_2 stacking fault energy is reduced due to Y additions.

To summarize, as a complement to previous experimental studies, we use theoretical methods to decompose the complex interplay of various mechanisms acting in Mg alloys in order to study some of them individually. Focusing solely on a few selected slip systems, we conclude that the impact of Y additions on generalized stacking fault energies is rather complex. On the one hand, the Y atoms reduce both stable and unstable stacking fault energies in the case of studied $\langle a \rangle$ slip systems. On the other hand, this influence may not be generalized to all slip systems as we predict also an increase of energies due to Y additions for most of the displacements along the $\langle 11\bar{2}3 \rangle$ direction in the non-basal plane $\{11\bar{2}2\}$ and a shift in position of stable SF. Due to the fact that previous studies of fcc materials linked the stable and unstable stacking fault energies with the mobility and activity of dislocations, we speculate that our findings can have similar consequences in the case of Mg alloys. As a verification of this speculation will necessarily require further theoretical studies addressing the full complexity of these materials, we have also developed and carefully tested a new EAM potential. The comparison of first-principles and EAM results indicates that our EAM potential may be suitable for future larger-scale atomistic simulations.

Chapter 7

The Solute Solution Effect in Mg Alloys

Generalized stacking fault energies indicate the mobility of dislocations. However, by applying so-called Peierls-Nabarro model with generalized stacking fault energies as input, we can calculate the core structures of dislocations and their Peierls stresses. Peierls stress is a measurement of dislocation mobility. As a continuation of chapter 6, this chapter will discuss the core structures and Peierls stresses of basal dislocations in Mg and Mg alloys in the framework of Peierls-Nabarro model.

7.1 Introduction

As a complementary approach of experiment to gain insight into the deformation mechanisms, theoretical simulations of dislocation cores of both $\langle a \rangle$ -type and $\langle c+a \rangle$ -type dislocations have been performed [40, 26, 80, 81]. To name a few examples, Yasi and co-workers [26] simulated the core structures of basal and prismatic dislocations by using the flexible boundary condition method and later the same authors developed different models to calculate the critical resolved shear stresses (CRSS) of basal dislocations [78] and the cross-slip stresses of prismatic screw dislocations [79]. This knowledge was recently further combined with a solute strengthening effect by Leyson and co-workers in their simulations of basal dislocations of Mg-Al alloys [42]. As another example, Shin *et al.* [80] developed so-called orbital-free density functional theory (OFDFT) method and applied it to dislocation core structures and subsequently also to Peierls stresses [81] in pure Mg.

The aforementioned atomistic-scale simulation methods belong to the direct methods that address dislocation cores by explicitly constructing them in computer simulations in an atom by atom manner. The structure is subsequently relaxed by molecular dynamics simulations. The molecular dynamics simulations can be of quantum-mechanical nature as, e.g., the density functional theory based flexible boundary condition method (DFT-FBC) [116], or based on atomistic inter-atomic potential simulations, such as embedded atom methods (EAM). It should be noted that the DFT-FBC simulations are accurate

but computationally very expensive. Atomistic simulations are fast but there is lack of reliable EAM potentials for Mg alloys.

Different from the direct methods, the indirect methods do not describe the dislocation core structure explicitly and employ the Peierls-Nabarro model [39]. The dislocation core structures can be analyzed by the two-dimensional Peierls-Nabarro model which was developed by Leibfried and Dietze [117]. The primary input is taken from the generalized stacking fault energies (GSFEs, so-called gamma surface) proposed by Vitek [28]. Gamma surface can be accurately calculated by DFT methods at moderate computational cost. Therefore, Peierls-Nabarro modeling represents a computationally highly efficient albeit more approximate alternative to the above discussed direct full field atomistic simulation methods. In the last years these models have been substantially improved and optimized. For example, Wang and co-workers have added gradients of misfit density to the total energy functional of dislocations in order to address dislocations possessing narrow cores [118]. Others have discretized the originally used arctan-type functions to describe the misfit density and obtained better results for Al [119, 120], since the discretized functions can provide more flexibility than the analytical (arctan-type) functions. Very recently Tsuru et. al. employed a semidiscrete variational PN model to study the core structures and Peierls stresses of Mg and two Mg alloys, namely Mg-Al and Mg-Y [38].

Despite numerous examples of applying the Peierls-Nabarro model to pure metals, its application to alloys is not straightforward. Calculations of gamma surfaces of alloys represent conceptional and computational challenges due to vast configurational spaces of different atomic species. Here we propose an efficient, and at the same time accurate, approach which is based on an approach that allows us to represent the full gamma surface using a few carefully selected sample points only. After carefully testing our proposed approach we demonstrate its performance in a high-throughput studying an extensive set of Mg binary alloys containing 20 different solutes for which we accurately predict widely dissociated cores of basal-plane $\langle a \rangle$ -dislocations and analyze the influence of solutes on the Peierls stress. In the final part we discuss error propagation in our Peierls-Nabarro model to estimate how DFT errors would affect the final results.

7.2 Computational Methodology

7.2.1 Peierls-Nabarro Model

The equilibrium configuration of a dislocation is within the Peierls-Nabarro model determined by the balance of restoring force and elastic resistance of the crystal lattice. Let us suppose that we have an edge dislocation in a Cartesian coordinate. The dislocation line runs along the z axis (for screw dislocation the dislocation line runs along the x axis), slips in the xz plane and its Burgers vector \vec{b} is parallel to x . The mathematical

Table 7.2.1:

The elastic constants (all in GPa) of Mg taken from Ref. [99] that were used as input for the Peierls-Nabarro model Eq. 7.2.1.

Elastic Constant	C ₁₁	C ₁₂	C ₁₃	C ₃₃	C ₄₄	K _e	K _s
value	59.5	26.1	21.8	61.6	16.4	1.96	1.31

expression of such a dislocation is

$$2K \int_{-\infty}^{+\infty} \frac{\vec{\rho}(x')}{x - x'} dx' = -\frac{d\gamma(\vec{u})}{d\vec{u}} \quad (7.2.1)$$

where the left side is the elastic resistance and the right side represents the restoring forces. Specifically \vec{u} is the misfit function and $\vec{\rho}(x)$ is the misfit density $\vec{\rho}(x) = d\vec{u}(x)/dx$. The generalized stacking fault energy, $\gamma(\vec{u})$, or gamma surface, is the key input quantity of the model. In a two dimensional case, \vec{u} is a vector consisting of components along x and z , u_x and u_z respectively. Mathematically $\vec{u} = (u_x, u_z)$. Further, K is a proportionality (so-called energy factor) that is in isotropic materials described by the shear μ and the Poisson constant ν , $K = K_e = \mu/4\pi(1 - \nu)$ for edge dislocations and $K = K_s = \mu/4\pi$ for screw dislocations. The subscript K_e and K_s indicates whether the constant is for an edge 'e' or a screw 's' dislocation. In an anisotropic media, K depends on slip system and dislocation character. For a basal $\langle a \rangle$ dislocation, $K_e = 1/4\pi(\bar{C}_{11} + C_{13})((C_{44}(\bar{C}_{11} - C_{13}))/((C_{33}(\bar{C}_{11} + C_{13} + 2C_{44})))^{1/2}$, $\bar{C}_{11} = (C_{11}C_{33})^{1/2}$; $K_s = 1/4\pi(C_{44}C_{66})^{1/2}$, $C_{66} = (C_{11} - C_{12})/2$. The values used in our simulations are summarized in Table 7.2.1.

An analytical solution of \vec{u} determined by Eq. 7.2.1 exists only for rather simple gamma surfaces. For more complex (and more realistic) gamma surfaces, solutions can be obtained only numerically. Often, the solution is obtained by expanding \vec{u} into a series of arctan functions [39]. The arctan function is a suitable basis since it is the analytical solution of Eq. 7.2.1 when the gamma surface is expressed by one cosine function. Dislocations described by arctan-type functions are called Peierls dislocations.

Specifically in our study, we focus on $\langle a \rangle$ -type dislocations that are known to dissociate and where the distance between the two partials is rather large[26]. This $\langle a \rangle$ -type edge dislocations can be well described by only four arctan functions, i.e., two for the edge component and two for the screw component. The misfit functions are then written as follows

$$u_x(x) = \frac{b}{2\pi} \arctan \frac{x - d_e/2}{w_e} + \frac{b}{2\pi} \arctan \frac{x + d_e/2}{w_e} + \frac{b}{2}; \quad (7.2.2a)$$

$$u_z(x) = \frac{\sqrt{3}b}{6\pi} \arctan \frac{x - d_s/2}{w_s} - \frac{\sqrt{3}b}{6\pi} \arctan \frac{x + d_s/2}{w_s}. \quad (7.2.2b)$$

where $u_x(x)$ and $u_z(x)$ describe the edge and the screw displacements, respectively. Here d_e or d_s is the distance between the edge or screw components of the two partial dislocations and w_e or w_s is the width of the edge or screw components of the Peierls dislocations. The subscript differentiates the edge component from the screw.

By proposing the solution in the form of trial functions Eq. 7.2.2 and applying the variational principle we transform the integral-differential Eq. 7.2.1 into an optimization problem. The left part of Eq. 7.2.1 is transformed into the elastic energy E_{el} [39],

$$E_{el} = H_{11} \left(\sum_{i,j} p_i p_j \ln \left(\frac{R}{w_i + w_j} \right) - \sum_{i < j} p_i p_j \ln \left(1 + \frac{r_{e,ij}^2}{(w_i + w_j)^2} \right) \right) + H_{33} \left(\sum_{i,j} q_i q_j \ln \left(\frac{R}{v_i + v_j} \right) - \sum_{i < j} q_i q_j \ln \left(1 + \frac{r_{s,ij}^2}{(v_i + v_j)^2} \right) \right) \quad (7.2.3)$$

H is Stroh tensor. $\{H_{11}, H_{33}\} = \{K_e, K_s\}$. $p_1 = p_2 = \frac{b}{2\pi}$, $q_1 = q_2 = \frac{\sqrt{3}b}{6\pi}$. The terms in the first bracket are the elastic energy of edge component, the second is the elastic energy of screw component. The half width of the partials $w_1 = w_2 = w_e$, $v_1 = v_2 = w_s$. R is the outer cut-off radius, $r_{e,ij}$ and $r_{s,ij}$ is the distance between the Peierls dislocations i and j . The distances $r_{e,12} = d_e$ for edge components and $r_{s,12} = d_s$ for screw components. The right part is transformed into the misfit energy E_A , i.e., the integral of the gamma surface within the core region of a dislocation

$$E_A = \int_{-R}^R \gamma(u_x(x), u_z(x)) dx \quad (7.2.4)$$

In our present work, we take the gradient of the misfit energy E_A as Peierls stress. Since the stress field far away from the dislocation core does not affect the core structure, a large but finite R is sufficient for the evaluation. In the present study we take $R = 5000b$, where b is the length of the Burgers vector of basal $\langle a \rangle$ dislocation. A larger R does not change the numerical solutions. The total energy of a dislocation is the sum of misfit energy and elastic energy,

$$E_{tot} = E_{el} + E_A. \quad (7.2.5)$$

Minimizing the total energy E_{tot} to create a dislocation is equivalent to solve Eq. 7.2.1. Therefore, we minimize E_{tot} (Eq. 7.2.5) in our present study in order to determine the geometry (characterized by parameters w and d) of the studied dislocations. For the minimization we use the particle swarm algorithm (PSA). This algorithm can effectively avoid local minima in the solution space and find the optimal solution [121, 122, 41].

7.2.2 Plane Wave Expansion of the Gamma Surface

Generally, for a crystal, the gamma surface can be expressed by the displacement vector $\vec{u} = (u_x, u_z)$,

$$\gamma(\vec{u}) = \sum_{\vec{G}} c_{\vec{G}} \exp(i2\pi\vec{G}\vec{u}) \quad (7.2.6)$$

where $\vec{G} = (m\frac{1}{a_x}, n\frac{1}{a_z})$, $m, n = 0, \pm 1, \pm 2, \dots \pm \infty$, a_x and a_z are the lengths of one period of the computational supercell along the x and z directions, so that $\gamma(\vec{u}) = \gamma(\vec{u} + \vec{T})$, translation vector $\vec{T} = (a_x, a_z)$. The coefficient $c_{\vec{G}}$ can be calculated by the Fourier transform

$$c_{\vec{G}} = \frac{1}{a_x a_z} \iint_{(0,0)}^{(a_x, a_z)} \gamma(u_x, u_z) \exp(-i2\pi\vec{G}\vec{u}) du_x du_z \quad (7.2.7)$$

Writing $c_{\vec{G}} = R_{\vec{G}} + iI_{\vec{G}}$, the gamma surface can be reformulated as

$$\gamma(\vec{u}) = \sum_{\vec{G}} R_{\vec{G}} \cos(2\pi\vec{G}\vec{u}) - I_{\vec{G}} \sin(2\pi\vec{G}\vec{u}) \quad (7.2.8)$$

where \vec{G} defines the reciprocal space of the gamma surface. After being Fourier transformed, the gamma surface can be represented by discrete points in reciprocal space. Each of these points corresponds to one coefficient of the terms shown in Eq. 7.2.6. Since $\gamma(\vec{u})$ is a real number, the imaginary terms disappear in Eq. 7.2.8. For convenience, the maximum coordinate of the reciprocal points $\vec{G}_k = (i/a_x, j/a_z)$, $|i| \leq k$, $|j| \leq k$ included in an expression of a gamma surface will be employed to represent the quality of the gamma surface.

7.2.3 Computational Parameters

The computational parameters for density functional theory calculations are same as the calculations in the previous chapter.

In the previous chapter, only a cross section of basal-plane gamma surface along $\frac{1}{3}[11\bar{2}0]$ is computed. In this chapter the whole gamma surface will be calculated. The two perpendicular vectors $\frac{1}{3}[11\bar{2}0]$ and $[10\bar{1}0]$ are selected within the $\{0001\}$ plane and all possible slip displacements can be written as a combination of these two vectors. Suppose u_x/a and $u_z/\sqrt{3}a$ are fractional displacements along these two directions determined by the selected vectors, the GSF vector \vec{f} is then written as

$$\vec{f} = \frac{u_x}{a} \frac{1}{3}[11\bar{2}0] + \frac{u_z}{\sqrt{3}a} [10\bar{1}0], \quad (7.2.9)$$

where $0 \leq u_x \leq a$ and $0 \leq u_z \leq \sqrt{3}a$. More details about the calculation of gamma surfaces can be found, e.g., in Refs. [34, 115].

In order to compare quantum-mechanical and atomistic approaches, the gamma surface of pure Mg was also calculated using atomistic simulations with an Embedded Atom Method (EAM) potential developed by Sun [24]. Using the same supercells as in the ab initio calculations, these simulations were performed employing the LAMMPS [100] code.

7.3 Gamma Surface Analysis

As stated above, the energetics of the gamma surface is the most important information that is necessary in Eq. 7.2.5. However, quantum-mechanical calculations that determine

these energies with a high accuracy, are computationally rather costly. As we are aiming at a rapid high-throughput testing of different solutes, lengthy calculations of hundreds of energies within dense meshes covering the gamma surface are not feasible. Therefore, in order to reduce the computational costs, we below propose an approach within which the energies of only five specific points are shown to be sufficient for accurately studying the core structure of $\langle a \rangle$ dislocations in hcp materials. Our approach will be validated for Mg and Mg-Y alloys.

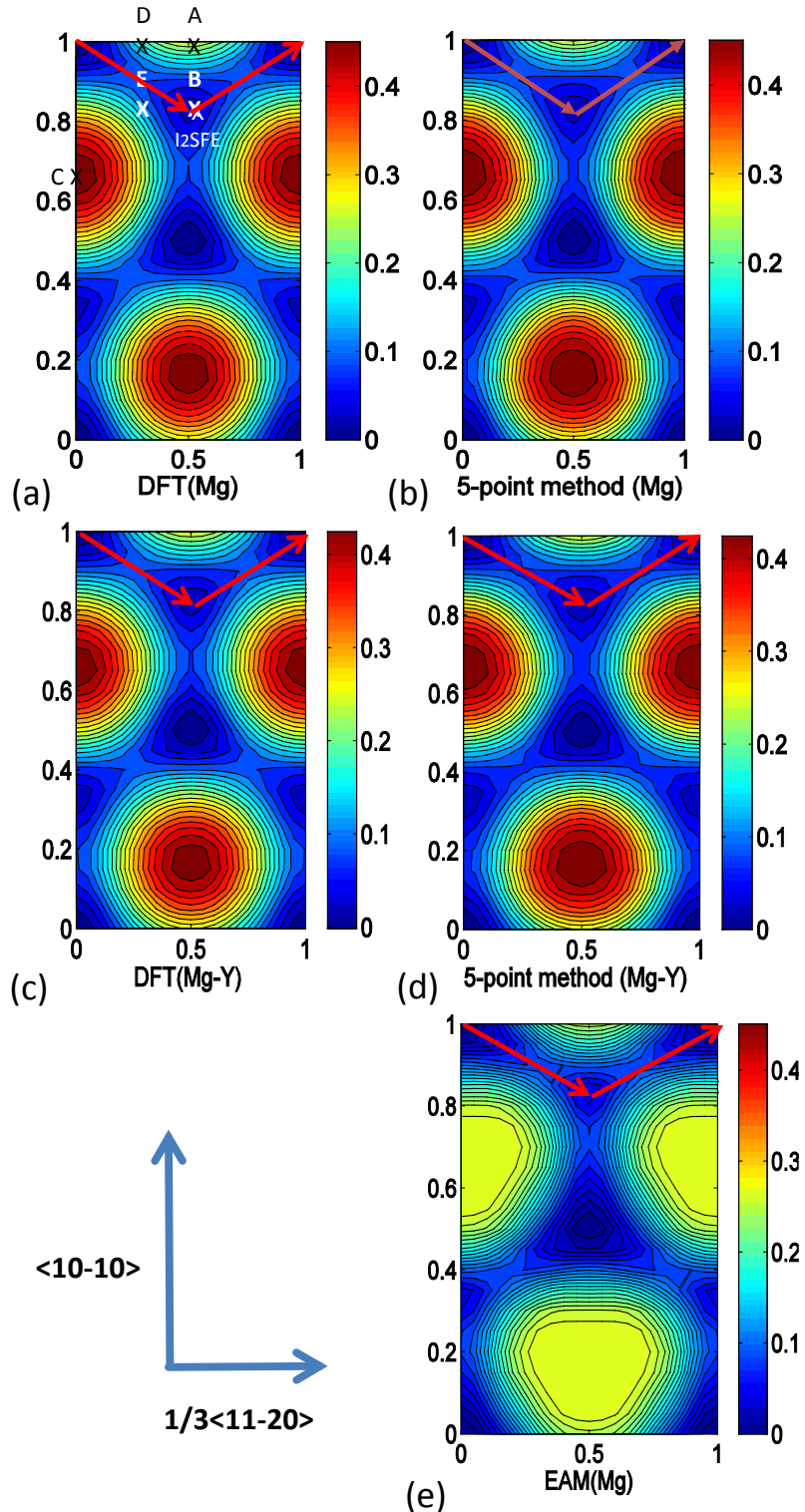
The gamma surface of basal plane in pure Mg has a three-fold symmetry (Figure 7.3.1 (a)). Within the unit cell there are three global unstable stacking fault energies (0.473 J/m^2) and three stable stacking fault energies (0.037 J/m^2). The minimum energy path (MEP) along the $\langle 11\bar{2}0 \rangle$ direction starts from the point corresponding to a perfect crystal and goes through a stable stacking fault energy to later reach another point corresponding to the perfect crystal (see red arrows). However the three-fold symmetry of Mg-Y gamma surface (Figure 7.3.1 (d)) is slightly broken by the addition of yttrium since the three global unstable stacking fault energies are different (0.440 J/m^2 , 0.440 J/m^2 , 0.438 J/m^2).

For comparison the identical gamma surface is also computed employing the EAM potential (Figure 7.3.1(b)). The EAM gamma surface shares the same features as the DFT one, but the maximum GSFE is significantly lower (see the color-coded scale). This difference results in barrier along the MEP.

As our aim is to determine the Peierls stress of the basal $\langle a \rangle$ -type dislocation, we analyze the sensitivity of the derived Peierls stress on the way we approximate/fit the gamma surface. This allows us to judge the quality of the gamma surface fitting accordingly. Specifically, we construct a series of gamma surfaces with different plane wave cutoff based on the , i.e., different number of k in \vec{G}_k in Eq. 7.2.8. Starting with a high plane wave cutoff we find that only very few terms within the expansion are larger than 1 mJ/m^2 while the majority of the terms equals to zero. This indicates that the Fourier representation rapidly converges implying that an accurate representation of the gamma surface can be achieved by only a few low frequency terms.

The dislocation core structure parameters are listed in Table 7.3.1 and are visualized in Figure 7.3.2. The edge components become convergent quickly for both (a) pure Mg and (c) Mg-Y alloy. When $k \geq 1$ the parameter values of edge components of Mg and Mg-Y are convergent; however for screw components the convergent core structures are obtained when $k \geq 5$ (see Figure 7.3.2(b) pure Mg and (d) Mg-Y alloy). Therefore the screw components are critical in determining the convergence of the dislocation cores. The safe cutoff of plane wave for both Mg and Mg-Y alloy is $\vec{G}_k \geq \vec{G}_5$.

Figure 7.3.3 shows that Peierls stress changes with the cutoff of plane wave. It is seen that Peierls stress is very sensitive to the number of plane wave applied in expressing gamma surface. The Peierls stress of pure Mg can drop from 45.8 MPa (for Mg-Y, 32.1 MPa) directly to 0 MPa, and then increase to 2.06 MPa (1.14 MPa for Mg-Y) before it becomes stable. When $\vec{G}_k \geq \vec{G}_5$, the value of the Peierls stress becomes rather stable even though small fluctuation still exists.


Figure 7.3.1:

Contour figures of basal-plane gamma surfaces for Mg and Mg-Y alloy computed by DFT or EAM method. The gamma surfaces obtained by application of 5-point method are shown as well for comparison. The five data points A, B, C, D, E employed in our 5-point method are denoted in subfigure (a). The minimum energy pathways are indicated by red arrows. The unit of color bar is J/m^2 .

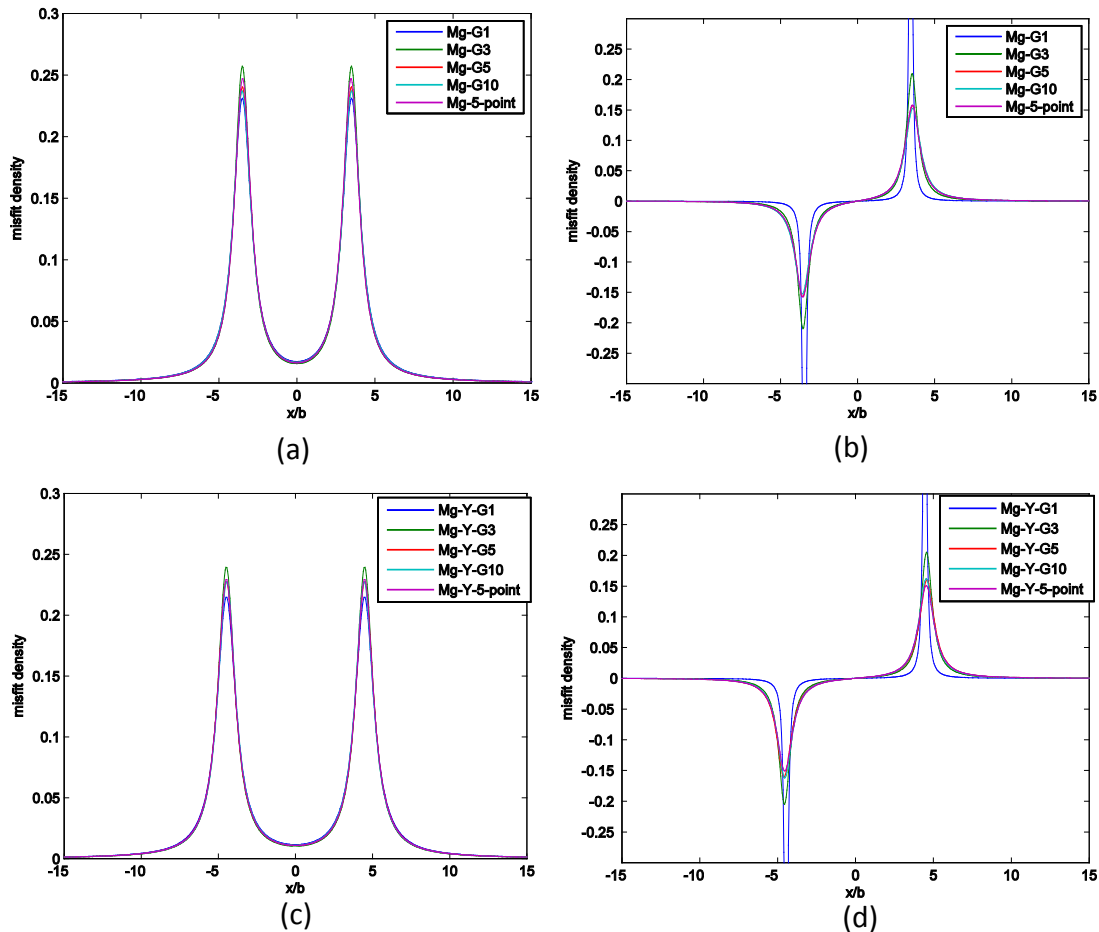


Figure 7.3.2:

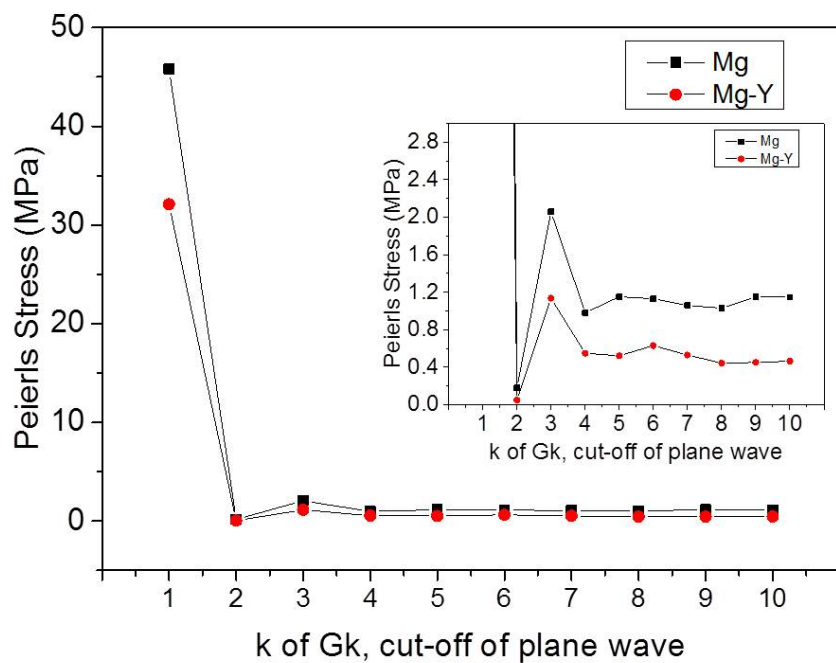
The test of the core structure of the $\langle a \rangle$ -type edge dislocation. With increasing number of plane wave series the core changes are convergent. (a) the edge component of the dislocation in Mg; (b) the screw component of the dislocation in Mg; (c) the edge component of the dislocation in Mg-Y alloy; (d) the screw component of the dislocation in Mg-Y alloy.

Table 7.3.1:

Geometrical parameters Peierls stresses of the $\langle a \rangle$ -type basal-plane edge dislocation calculated for different plane wave cutoffs (expressed by \vec{G}_k).

(a) pure Mg					
\vec{G}_k	d_e/b	d_s/b	w_e/b	w_s/b	τ/MPa
\vec{G}_1	6.995	6.900	0.695	0.093	45.8
\vec{G}_3	6.984	7.077	0.623	0.436	2.06
\vec{G}_5	6.979	7.143	0.668	0.581	1.15
\vec{G}_{10}	7.008	7.183	0.677	0.597	1.15
5-point	6.947	7.097	0.649	0.579	1.08

(b) Mg-Y alloy					
\vec{G}_k	d_e/b	d_s/b	w_e/b	w_s/b	τ/MPa
\vec{G}_1	8.953	8.904	0.745	0.095	32.1
\vec{G}_3	8.965	9.119	0.668	0.447	1.14
\vec{G}_5	8.964	9.173	0.704	0.570	0.522
\vec{G}_{10}	8.913	9.077	0.704	0.564	0.464
5-point	8.956	9.086	0.698	0.607	0.577


Figure 7.3.3:

The test of the Peierls stress of the $\langle a \rangle$ -type edge dislocation in pure Mg. With increasing number of plane wave series the value of the Peierls stress becomes stable at \vec{G}_5 .

Since the three-fold symmetry of Mg gamma surface, the Fourier expansion under the condition of \vec{G}_5 can be expressed by symmetrized plane wave (or equivalent trigonometric functions). Its full expression is Eq. 7.3.1 plus smaller high frequency terms with coefficients of the order of $10^{-1} - 10^{-2} \text{ mJm}^{-2}$. These small terms challenge the accuracy of current DFT method, and therefore can be considered as background noise.

For convenience the expression (Eq. 7.3.1) without the smaller terms is referred as 5-point expression, considering that in principle the 5 coefficients in the equation can be determined by 5 points of gamma surface (one of the 6 coefficients is excluded since we have a default condition $\gamma_{basal}(0, 0) = 0$). This method to determine the gamma surface is referred to 5-point method by the authors. The dislocation core structures and Peierls stresses computed by our 5-point method are listed in Table 7.3.1 under "5-point". The results computed by the 5-point method are in good agreement with results computed by applying \vec{G}_{10} gamma surface. The maximal error bar belongs to the Peierls stress of Mg-Y alloy, about 24%. This error bar is satisfied considering that yttrium breaks the symmetry of gamma surface and can introduce more error when Eq. 7.3.1 is applied to Mg-Y alloy. More discussion about the errors in Peierls-Nabarro model can be found in section 7.6.

$$\begin{aligned}
 \gamma_{basal}(u_x, u_z) = & R_0 \\
 & + R_1 \{ \cos(2\pi(\frac{u_x}{a} - \frac{u_z}{\sqrt{3}a})) + \cos(2\pi(\frac{u_x}{a} + \frac{u_z}{\sqrt{3}a})) + \cos(4\pi(\frac{u_z}{\sqrt{3}a})) \} \\
 & + R_2 \{ \cos(2\pi(\frac{u_x}{a} - \frac{3u_z}{\sqrt{3}a})) + \cos(2\pi(\frac{u_x}{a} + \frac{3u_z}{\sqrt{3}a})) + \cos(4\pi(\frac{u_x}{a})) \} \\
 & + R_3 \{ \cos(4\pi(\frac{u_x}{a} + \frac{u_z}{\sqrt{3}a})) + \cos(4\pi(\frac{u_x}{a} - \frac{u_z}{\sqrt{3}a})) + \cos(8\pi(\frac{u_z}{\sqrt{3}a})) \} \\
 & + I_1 \{ \sin(2\pi(\frac{u_x}{a} - \frac{u_z}{\sqrt{3}a})) - \sin(2\pi(\frac{u_x}{a} + \frac{u_z}{\sqrt{3}a})) + \sin(4\pi(\frac{u_z}{\sqrt{3}a})) \} \\
 & + I_2 \{ \sin(4\pi(\frac{u_x}{a} - \frac{u_z}{\sqrt{3}a})) - \sin(4\pi(\frac{u_x}{a} + \frac{u_z}{\sqrt{3}a})) + \sin(8\pi(\frac{u_z}{\sqrt{3}a})) \} \quad (7.3.1)
 \end{aligned}$$

where a is the lattice parameter.

The gamma surfaces for Mg and Mg-Y approximated by Eq. 7.3.1 are shown in Figure 7.3.1 (b) and (d). They reproduce the key characteristics of the quantum-mechanically calculated ones (Figure 7.3.1 (a)). The predicted stable stacking fault energies and unstable stacking fault energies agree quantitatively well with the DFT derived ones. For pure Mg its quality is much better than that of the computationally inexpensive EAM-computed gamma surface (Figure 7.3.1 (e)), which can only qualitatively reproduce the main features. The comparison of the DFT computed gamma surface with a high number of calculated mesh points (Figure 7.3.1 (a)) and the one approximated by 5-point method (Figure 7.3.1 (b) and (d)) further confirms that it is satisfied to employ 5-point method to calculate Peierls stress for basal $\langle a \rangle$ dislocation.

7.4 The five GSFEs of Mg alloys

Even though five data points are sufficiently enough to obtain the gamma surface, not all possible data points are an equally good choice. On one hand, data points that are too close to each other may result in noticeable numerical errors. On the other hand, the data points in the area around the MEP in the gamma surface are very important. Considering both points, we choose the five data points *A*, *B*, *C*, *D* and *E*, which are referred to Figure 7.3.1(a). The I_2 stacking fault energy (*B*), the unstable SFE along the $\langle a \rangle$ -type direction (*A*) and the global maximum USFE (*C*) have also a clear physical meaning and significance. In pure hcp metals, I_2 stacking fault energy (*B*) is usually considered to be the maximum energy barrier that dissociated $\langle a \rangle$ -type dislocations must overcome to move, so it is relevant to the mobility of dissociated $\langle a \rangle$ -type dislocations. Similarly, point *A* is relevant to the mobility of perfect $\langle a \rangle$ -type dislocations. Finally, the point *C* is the barrier to nucleate $\langle a \rangle$ -type dislocations. Apart from these three points, the two points *C* and *D* which are close to the MEP are selected.

A set of 20 solutes with either hcp or double hcp crystal structures are selected from the Periodic Table of the Elements. The 5 GSFEs computed by DFT for these 20 Mg alloys are listed in Table 7.4.1. According to the values of the GSFEs, the following 5 sequences are obtained (the locations of pure Mg and Mg-Y are stressed in bold fonts):

According to *A*:

La<Pr<Nd<**Y**<Ho<Er<Tm<Lu<Zr<Hf<Sc<Ti<**Mg**<Be<Zn<Tl<Re<Os<Co<Tc<Ru;

According to *B*:

La<Pr<Nd<Ho<Er<Tm<Lu<**Y**<Tl<Zn<Sc<Hf<**Mg**<Zr<Be<Ti<Co<Re<Tc<Os<Ru;

According to *C*:

La<Pr<Nd<**Y**<Ho<Er<Tm<Lu<Zr<Hf<Sc<Ti<**Mg**<Be<Zn<Tl<Re<Os<Co<Tc<Ru;

According to *D*:

La<Pr<Nd<Ho<Er<**Y**<Tm<Zr<Hf<Sc<Lu<Ti<Be<Zn<Tl<**Mg**<Re<Os<Co<Tc<Ru;

According to *E*:

La<Pr<Nd<**Y**<Ho<Er<Tm<Lu<**Mg**<Hf<Zr<Sc<Be<Ti<Zn<Tl<Co<Re<Os<Tc<Ru.

Three of the five data sets (*A*, *B*, *C*) are shown in Figure 7.4.1.

The chemical element sequences according to *A* and *C* are exactly the same, but different from the three sequences according to *B*, *C* and *E*. Any two of these three sequences are also different. This finding indicates that the alloying elements do not change the gamma surface of a pure host material (here the Mg matrix) in a homogeneous manner that can be described by a single scaling factor. Some general trends can be seen, such as that if unstable GSFEs (e.g. *A* or *C*) are lower, the corresponding I_2 SFEs (*B*) are lower, too. The maximum values of all five parameters are those computed for the Mg-Ru system, and minimum ones are those of Mg-La. Ruthenium increases the GSFEs (*A* – *E*) of pure Mg by 0.01-0.05 Jm^{-2} . La can reduce the GSFEs (*A* – *E*) of pure Mg by 0.02-0.04 Jm^{-2} . Interestingly, the I_2 SFE (*B*) of Mg-La is 1 mJm^{-2} , very close to 0, followed by Mg-Pr, 8 mJm^{-2} and Mg-Nd, 11 mJm^{-2} . The other elements change GSFEs moderately. Next to our values Table 7.4.1 also lists published theoretical and

Table 7.4.1:

Generalized stacking fault energies of selected five points in basal gamma surface for 20 Mg₄₇X alloys. The planar and bulk concentrations are 25% and 2.08%, respectively.

solute	A Jm ⁻²	B Jm ⁻²	C Jm ⁻²	D Jm ⁻²	E Jm ⁻²
Mg	0.275,0.288[95]	0.037,0.036[95], 0.033[96],	0.473	0.159	0.158
Mg-Exp.		0.060-0.15[123]			
Y	0.257,0.248[95]	0.030, 0.025[95]	0.446	0.145	0.146
Be	0.277	0.038	0.476	0.154	0.166
Co	0.302	0.077	0.495	0.168	0.191
Er	0.258	0.027	0.448	0.145	0.152
Hf	0.267	0.036	0.458	0.149	0.160
Ho	0.257	0.025	0.447	0.145	0.151
La	0.234	0.001	0.422	0.132	0.132
Lu	0.262	0.029	0.453	0.152	0.155
Nd	0.242	0.011	0.430	0.137	0.139
Os	0.302	0.083	0.491	0.168	0.193
Pr	0.240	0.008	0.428	0.135	0.137
Re	0.301	0.078	0.491	0.167	0.191
Ru	0.308	0.085	0.502	0.170	0.197
Sc	0.271	0.036	0.465	0.151	0.162
Tc	0.306	0.080	0.498	0.169	0.194
Ti	0.275,0.355[95]	0.042, 0.036[95]	0.469	0.153	0.166
Tl	0.282	0.035	0.485	0.158	0.168
Tm	0.260	0.028	0.451	0.146	0.154
Zn	0.279,0.256[95]	0.035,0.037[95]	0.480	0.155	0.166
Zr	0.267,0.328[95]	0.038,0.026[95]	0.457	0.149	0.160

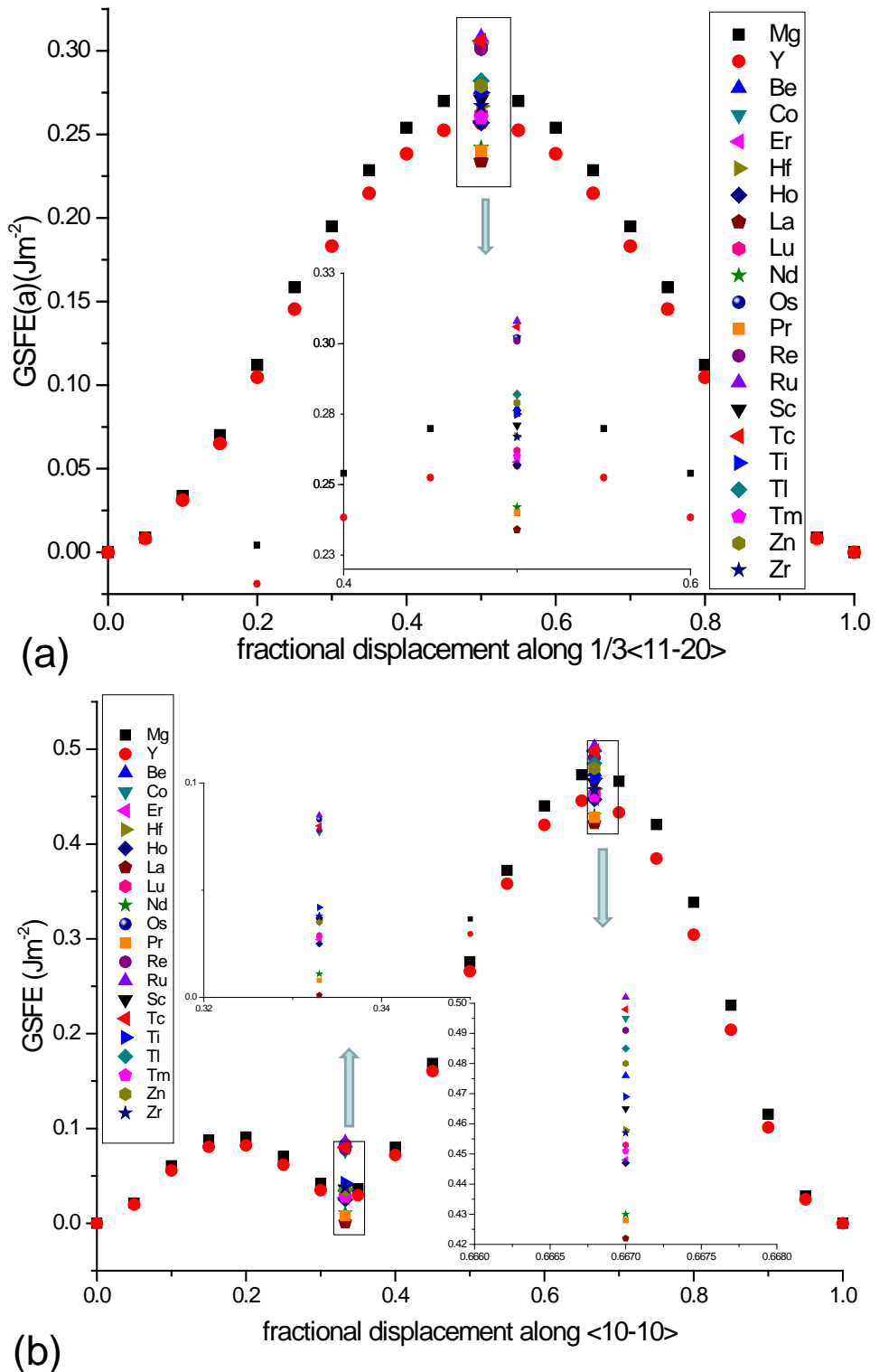


Figure 7.4.1:

Three GSFEs predicted for Mg alloys. (a) GSFE along $1/3<11\bar{2}0>$, point A; (b) I_2 SFE (point B) and global unstable stacking fault energies C. The positions of these GSFEs in the whole gamma surface are referred to Figure 7.3.1(a).

experimental GSFEs. For Mg, the published theoretical data validate our GSFEs of points *A* and *B*. Comparing with the experimental data the lower experimental bound is a factor of two larger than the theoretical value. The reason may be that the stacking fault energy in pure Mg is rather small, making an accurate experimental determination of this value very challenging. The I_2 SFEs of Mg-Y, Mg-Ti, Mg-Zn and Mg-Zr published by Muzyk *et al.* [95] agree well with ours. The USFE (at point *A*) of Mg-Y is also very close to our result, while those of Mg-Zn, Mg-Ti and Mg-Zr are slightly different. These differences might arise from the different computational methods and slightly different values for input parameters required by VASP software.

7.5 Dislocation Properties

7.5.1 Pure Mg

The gamma surfaces of pure Mg were evaluated by both EAM (employed Finnis-Sinclair potential developed by Sun [24]) and DFT for comparison. Since the GSFEs by EAM and DFT are quite different, the dislocation cores obtained using these two approaches are also very different. The predicted dislocation core width by PN model using EAM gamma surface is $\approx 3b$, and by DFT $\approx 7b$. Hence, the EAM core is much more compact than the one derived by DFT. The difference can be explained by Volterra dislocation model. In the model the core width is inversely proportional to the stable stacking fault energy. Indeed EAM predicts a higher I_2 stable stacking fault energy (48 mJm^{-2}) and generalized stacking fault energies along the minimum energy path (relative to maximum GSFE) (see Figure 7.3.1 b) than the DFT calculations ($I_2\text{SFE}=37 \text{ mJm}^{-2}$).

The parameters of the core structure can be employed to compute the hydrostatic stress field of the dislocation [41] in Mg which is shown in Figure 7.5.1 (a). The magnitude of the stress is used to color the atoms. The colored atoms clearly indicate the location of the two partial dislocations. Between the two partials is the stacking fault.

Wang employed a modified Peierls-Nabarro model (including a new gradient term which is considered to be important to describe dislocations having a narrow core) to calculate the core structure of pure Mg [118]. The core width calculated in Wang's work is $6.7b$ which is in excellent agreement with ours, $7b$. Applying the modified model with the gradient terms they predicted much wider half width (e.g. w_d, w_s) for each partials. The planar core was computed directly by Yasi *et al.* [26] using so-called flexible boundary condition (DFT-FBC) [116], which is considered to be very accurate in determination of dislocation cores. The distance between the two partials calculated by them is $5.2b$, which is slightly smaller than ours.

The Peierls stress computed by DFT is 1.15 MPa, which is one order smaller than that from the EAM simulations (22.9 MPa). Both values are substantially larger than experimental values observed in pure Mg single crystals (0.5-0.8 MPa). If we use all the available DFT data and go beyond the 5-point method by taking Fourier coefficients of \vec{G}_{10} for computing the gamma surface, the Peierls stress is still 1.15 MPa (actually the

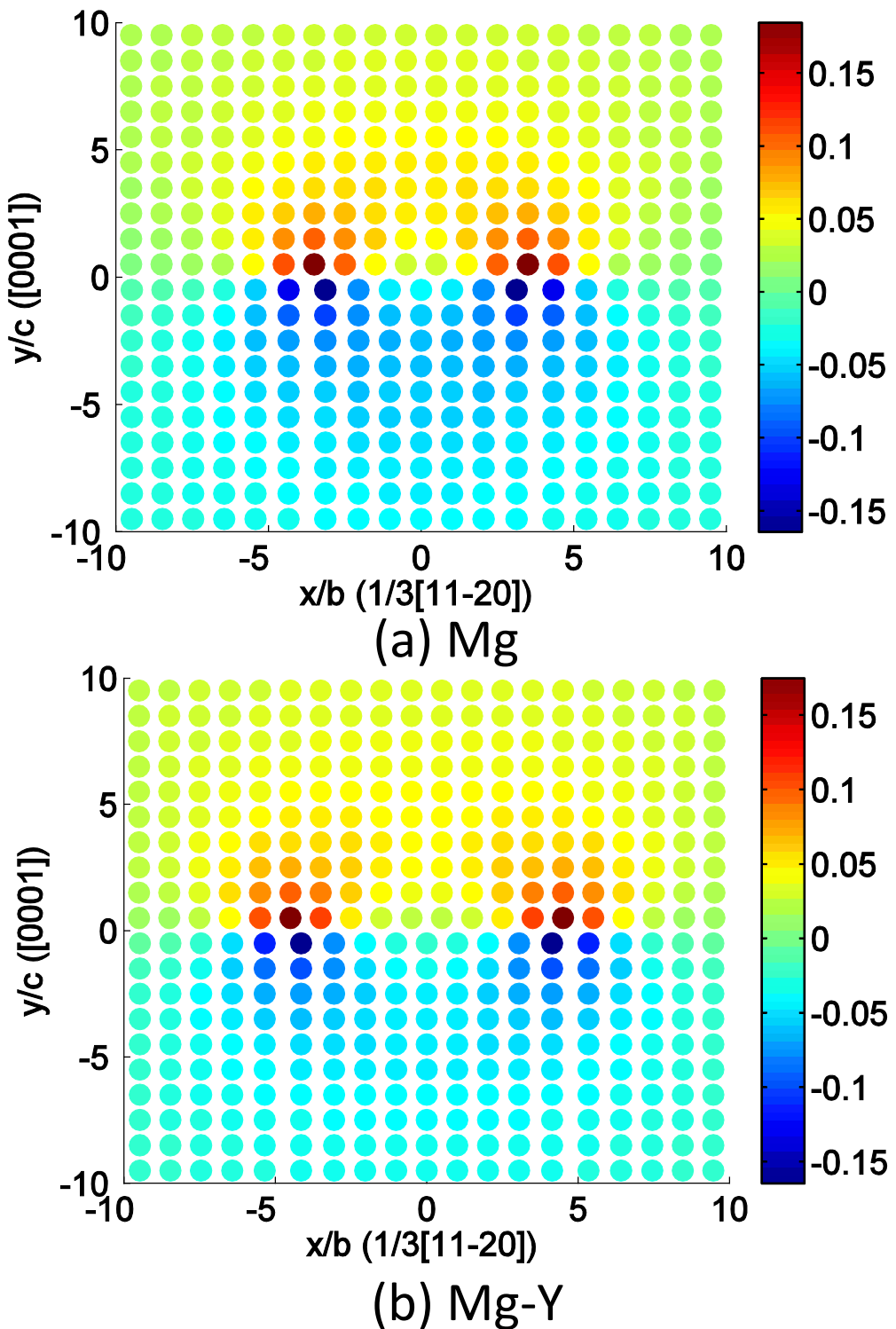


Figure 7.5.1:

The core structures of pure Mg and Mg-Y alloy. The color bar denotes the hydrostatic stress values in GPa. The colored atoms clearly show the location of two partial dislocations with stacking fault inbetween. b and c are the lengths of one period in each direction.

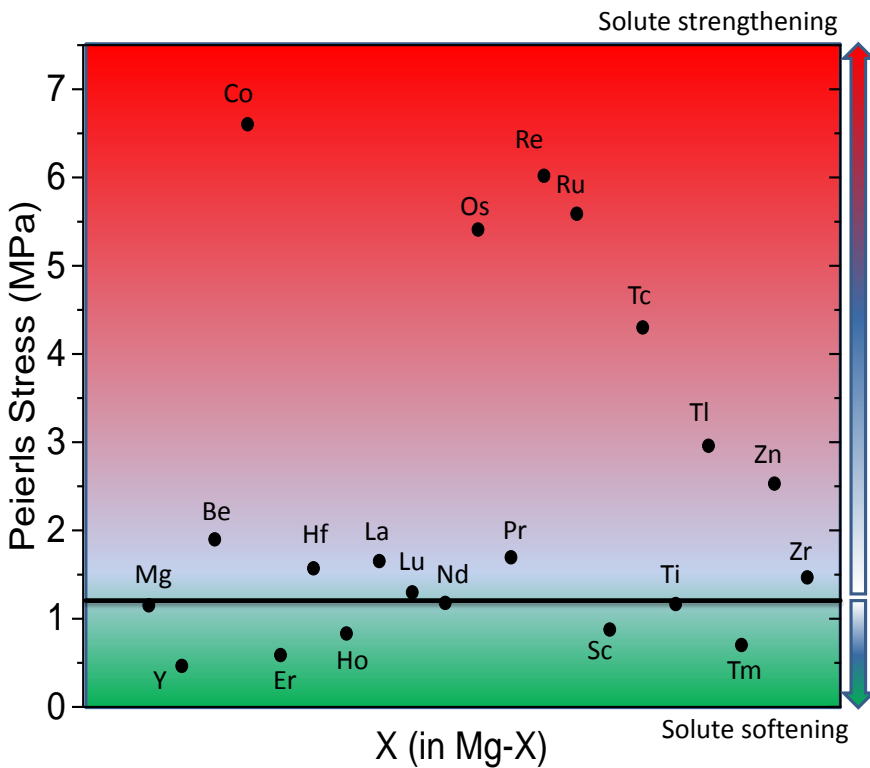


Figure 7.5.2:

The Peierls stresses of 20 Mg alloys predicted by Peierls-Nabarro model using 5-point method. The black line corresponds to the Peierls stress of Mg.

difference is minor, about 0.005 MPa).

7.5.2 Mg Alloys

Employing our 5-point approach dislocation the core structures and Peierls stresses of 20 Mg alloys are computed and their characteristics are summarized in Table 7.5.1. The Peierls stresses along with the solutes in the Mg alloys are visualized in Figure 7.5.2. The black line in Figure 7.5.2 denotes the Peierls stress of pure Mg. In principle the solutes above the line increase the Peierls stress of Mg, which shows so-called solute strengthening effect; the solutes below the line reduce the Peierls stress and shows solute softening effect.

However, when the error bar of the Peierls stress is considered, the actual changes of Peierls stresses which are close to the Peierls stress of pure Mg are uncertain. The error bar of Peierls stress of Mg-Y alloy is employed here. In this spirit the solutes are divided into three groups: (i) the first group, consisting of Be, Zn, Tl, Tc, Os, Ru, Re and Co when added as solutes into Mg lead to more compact core structures ($3.0 \text{ } b$ - $7.1 \text{ } b$, $b=3.19 \text{ \AA}$) and larger Peierls stress than pure Mg (1.9-6.6 MPa). (ii) Elements in the second group, including Ti, Nd, Lu, Zr, Hf, La, and Pr change as solutes in Mg the core

widths from 7.0 b -19.2 b and Peierls stresses moderately (1.2-1.7 MPa). (iii) The solute elements in the third group containing Y, Er, Tm, Ho and Sc extend the core width from 9 b -13 b , and the resulting Peierls stresses are generally very low (0.46-0.88 MPa). As an example, the dislocation core structure of Mg-Y is shown in Figure 7.5.1(b). Under the condition that the error bar of Mg-Y alloy applies to all Mg alloys, it can be concluded that the first group is able to strengthen the basal $\langle a \rangle$ dislocation, and the third group is able to soften the basal $\langle a \rangle$ dislocation. The effect of the second group is however unclear.

The relation between Peierls stresses of basal $\langle a \rangle$ dislocations and the ductility of Mg and Mg alloys is complicated and unclear. It is very difficult to directly connect the Peierls stress with ductility in these materials. But Peierls stress itself is a concept that is closely related with ductility. If the Peierls stresses of all slip systems relevant to deformation become lower in a Mg single crystal, the material is very likely to be more ductile. However, in polycrystal Mg and Mg alloys, the knowledges about ductility that we can obtain from the Peierls stresses of only basal $\langle a \rangle$ dislocations are not much. Therefore we will try to apply our method to other slip system, like prismatic $\langle a \rangle$ dislocation in order to get a deeper insight of ductility phenomena.

7.6 Case Study of Error Propagation in the Peierls-Nabarro Model

After discussing parametrization Fourier expansion of the gamma surface, we now analyze error-propagation within the Peierls-Nabarro model in cases of pure Mg and Mg-Y. Apart from systematic errors due to the model assumptions, there are three sources of errors entering the Peierls-Nabarro model: (i) the approximation of the elastic energy E_{el} (Eq. 7.2.3); (ii) the numerical algorithm applied to solve the model; (iii) the accuracy of gamma surface.

To estimate (i), we note that the basal plane of hcp metal can be treated as isotropic. We can therefore ignore the interaction between screw component and edge component when expressing the elastic energy and the corresponding error is considered negligible. To address (ii) we note that the applied numerical algorithm in this study is Particle Swarm Optimization. This algorithm is believed to effectively avoid trapping in local minima, nevertheless, this cannot be guaranteed. In order to find the global minimum and avoid local minima, we therefore run the optimization calculations several times with slightly different initial parameters. Therefore, the major source of errors is represented by the gamma surface as the only input for the Peierls-Nabarro model.

Our analysis is based on the data in Table 7.6.1(a) which are part of Table 7.3.1. In order to analyze error-propagation properties, the results computed by gamma surfaces of \vec{G}_{10} for both Mg and Mg-Y are employed below as references. These results are assumed by definition to be error free (see "E0" in Table 7.6.1(b)). Represent the gamma surface of \vec{G}_5 and drop the terms \vec{G}_k ($5 < k \leq 10$), we introduce the first error "E1" (see Table

Table 7.5.1:

Geometrical parameters of dislocation cores and Peierls stresses for 20 Mg alloys. The Peierls stresses of Mg alloys are normalized by that of pure Mg computed by the 5-point approach.

solute	d_e/b	d_s/b	w_e/b	w_s/b	τ_p/MPa
Mg-DFT1 ^a	7.00	7.18	0.68	0.60	1.15
Mg-DFT2 ^b	6.95	7.10	0.65	0.59	1.15
	6.7 [118]	6.7 [118]	3.7 [118]	3.0 [118]	
Mg-EAM ^c	3.06	2.90	0.45	0.38	22.9
Mg-Exp. ^d					0.52-0.81[124, 125, 126]
Mg-FBC ^e	5.2[26]				
Y	8.91	9.08	0.70	0.56	0.46
Be	6.98	7.07	0.61	0.52	1.90
Co	3.03	3.16	0.55	0.48	6.60
Er	12.93	13.00	0.67	0.56	0.59
Hf	6.99	7.09	0.64	0.54	1.57
Ho	10.96	11.04	0.66	0.56	0.83
La	19.18	19.24	0.72	0.59	1.65
Lu	8.96	9.06	0.64	0.55	1.30
Nd	13.10	13.18	0.69	0.58	1.18
Os	3.01	3.15	0.56	0.49	5.41
Pr	17.09	17.15	0.69	0.58	1.70
Re	3.03	3.17	0.56	0.48	6.02
Ru	3.01	3.14	0.55	0.48	5.59
Sc	8.93	9.01	0.63	0.53	0.88
Tc	4.82	4.92	0.58	0.51	4.30
Ti	6.95	7.05	0.62	0.53	1.17
Tl	7.00	7.10	0.59	0.50	2.96
Tm	10.94	11.00	0.65	0.54	0.70
Zn	6.94	7.11	0.64	0.52	2.53
Zr	6.98	7.09	0.64	0.54	1.47

a: gamma surface of \vec{G}_{10} expression;

b: gamma surface of 5-point approach;

c: gamma surface computed by Finnis-Sinclair-EAM potential using LAMMPS;

d: experimental results;

e: direct simulation of dislocation using DFT.

7.6.1(b)). The core structure and the Peierls stresses calculated by 5-point method includes the approximations of (i) dropping the terms included in \vec{G}_5 but excluded from gamma surface of 5-point method and (ii) using only 5 points to fit the gamma surface of 5-point method (Eq. 7.3.1). These two parts of error sources are put into the error "E2". In the case of Mg-Y alloy, the error "E2" also includes the influence of yttrium on the gamma surface symmetry. The total errors introduced by the 5-point method are listed under "E3" in the table. Applying the data under the lists of \vec{G}_{10} , \vec{G}_5 and "5-point", these four errors can be calculated by the following equations:

$$\begin{aligned} E0 &= \frac{\vec{G}_{10} - \vec{G}_{10}}{\vec{G}_{10}} \times 100\%; \\ E1 &= \frac{\vec{G}_5 - \vec{G}_{10}}{\vec{G}_{10}} \times 100\%; \\ E2 &= \frac{5 - \text{point} - \vec{G}_5}{\vec{G}_5} \times 100\%; \\ E3 &= \frac{5 - \text{point} - \vec{G}_{10}}{\vec{G}_{10}} \times 100\%. \end{aligned} \quad (7.6.1)$$

Table 7.6.1(b) shows the results of these errors. Under "E3" are listed the error bars of our 5-point method. Generally the error bars of the Peierls stresses are much larger than those of the core structure parameters. For example, the maximal error bars of the core structure parameters are 4% in pure Mg and 7% in Mg-Y alloy, while for Peierls stresses the error bars can be as large as 6% in pure Mg and 24% in Mg-Y alloy. Therefore the Peierls stresses are more sensitive to the approximations of gamma surfaces than the core structures. The small variations of core structures are magnified when passing to Peierls stresses. Since the yttrium slightly breaks the symmetry of the gamma surface which introduces an additional approximation to the case of Mg, the error bars of Mg-Y are generally larger than those of Mg in terms of both the core structure parameters and the Peierls stresses. Therefore in the case of other Mg alloys the error bar of Peierls stress of Mg-Y is applied for safety reason.

The errors listed under "E1" are less than 3% for pure Mg, which means the smaller terms of high frequencies (the coefficients $< 10^{-1} \text{mJm}^{-2}$) are not important in our calculations for pure Mg. However, leaving out of these terms causes moderate error in case of Mg-Y alloy, 12.5%. Application of only 5 data points to fit Eq. 7.3.1 instead of expressing the gamma surface up to \vec{G}_5 using the 20×20 mesh can introduce errors of about 6% to Peierls stress and less than 3% to the core structure in pure Mg. In Mg-Y alloy, this approximation leads to errors of 10.5% to Peierls stress and up to 6% to the core structure. These error bars prove that it is reasonable to make the approximations and our data are useful. To the best knowledge of the authors, we analyze the error propagation in the case of pure Mg and Mg-Y alloy. This can be used to, for example, carefully check the previous published results and direct the future users of Peierls-Nabarro model.

Table 7.6.1:

Error propagation in the Peierls-Nabarro model in the cases of pure Mg and Mg-Y alloy.

(a) The core structure parameters and Peierls stresses computed by different expressions of the gamma surface.

	γ_{basal}	d_e/b	d_s/b	w_e/b	w_s/b	τ/MPa
Mg	\vec{G}_{10}	7.008	7.183	0.677	0.597	1.15
	\vec{G}_5	7.009	7.040	0.668	0.581	1.15
	5-point	6.947	7.097	0.649	0.579	1.08
Mg-Y	\vec{G}_{10}	8.913	9.077	0.704	0.564	0.464
	\vec{G}_5	8.964	9.173	0.704	0.570	0.522
	5-point	8.956	9.086	0.698	0.607	0.577

(b) The error bars of quantities listed in (a). $E0 = \frac{\vec{G}_{10} - \vec{G}_5}{\vec{G}_{10}} \times 100\%$;
 $E1 = \frac{\vec{G}_5 - \vec{G}_{10}}{\vec{G}_{10}} \times 100\%$; $E2 = \frac{5\text{-point} - \vec{G}_5}{\vec{G}_5} \times 100\%$; $E3 = \frac{5\text{-point} - \vec{G}_{10}}{\vec{G}_{10}} \times 100\%$.

	Errors	$d_e/\%$	$d_s/\%$	$w_e/\%$	$w_s/\%$	$\tau/\%$
Mg	E0	0.00	0.00	0.00	0.00	0.00
	E1	0.01	-1.99	-1.33	-2.68	0.44
	E2	-0.88	0.81	-2.84	-0.34	-6.25
	E3	-0.87	-1.20	-4.14	-3.02	-5.84
Mg-Y	E0	0.00	0.00	0.00	0.00	0.00
	E1	0.58	1.05	-0.08	1.09	12.50
	E2	-0.10	-0.95	-0.86	6.38	10.54
	E3	0.48	0.09	-0.94	7.54	24.35

7.7 Conclusions

The gamma surfaces of Mg and Mg alloys have been systematically studied employing both quantum-mechanical and atomistic simulations and used as input information for corresponding calculations based on the Peierls-Nabarro model to determine the dislocation core structures and Peierls stresses of basal-plane $\langle a \rangle$ -type dislocations. We summarize our most important conclusions as follows:

- (i) We first show that the gamma surface of basal-plane $\langle a \rangle$ -type dislocations in hcp materials can be very well approximated by a Fourier series with only a few terms and coefficients determined from the knowledge of only five special points within the generalized stacking fault energy surface. Our comparative analysis is based on quantum-mechanical calculations and the quality is judged according to the Peierls stress that is derived from Peierls-Nabarro model that uses the gamma surface as input. Our statement is supported by analyzing error-propagation properties of Peierls-Nabarro model. Therefore, our 5-point method that greatly reduces the computational costs, is justified to be applied to other Mg alloys in a high-throughput manner. Our tests performed for pure Mg and Mg-Y show that the five input values from ab initio calculations provide better dislocation core geometries than faster atomistic simulations calculated by EAM potential developed by Sun.
- (ii) Our analysis of 20 different solutes show that the energetics of the gamma surfaces is upon alloying not changed uniformly in a manner that would allow for a description of change by a single scaling factor. Therefore, care should be taken when extending the analysis of gamma surfaces to different concentrations of solutes by scaling factors.
- (iii) For pure Mg, the predicted basal-plane $\langle a \rangle$ -type dislocation core structure calculated using a DFT derived gamma surface is $7b$ wide. The calculated Peierls stress is 1.15 MPa, which is pretty close to the experimental values.
- (iv) Among the 20 solutes, Be, Zn, Tl, Tc, Os, Ru, Re and Co are able to strengthen the basal $\langle a \rangle$ dislocation, while Y, Er, Tm, Ho and Sc soften the basal $\langle a \rangle$ dislocation. The effects of the other solutes are however unclear.

The success of the 5-point method for calculating basal $\langle a \rangle$ -type dislocations encourages us to continue to use it for prismatic $\langle a \rangle$ -type dislocations in a next step. By combining the knowledge of both types of slip systems, we can select solutes which reduce the gap between the Peierls stresses of basal and prismatic slip (e.g. increase basal slip or decrease prismatic slip). The narrowed gap allows for a more homogeneous deformation of Mg alloys and thus may ductilize the the rather brittle Mg.

Chapter 8

Conclusions: Design of Novel Ductile Mg Alloys

This thesis is aimed at providing a deeper fundamental knowledge and understanding of processes that are responsible for an increased macroscopic ductility detected in Mg alloys with rare-earth additions. Magnesium alloys combine low densities with a relatively high strength and that is particularly interesting for automobile and aerospace industries. A wider use of Mg alloys has been, unfortunately, hindered by their low room-temperature ductility that prevents, e.g., forming and shaping during common manufacturing production processes. Rare-earth additions are known to ameliorate the ductility in Mg alloys but an atomistic origin of the experimentally found ductility has not been clear so far. Therefore, theoretical means, quantum-mechanical and atomistic calculations as well as continuum methods, have been used in this thesis to shed more light on this important and interesting phenomenon.

The author of this thesis was during his Master studies involved in a theoretical research that was aimed at explaining experimental findings collected at the Max-Planck-Institut für Eisenforschung (MPIE) in Düsseldorf, Germany. The experimental mechanical testing of pure bulk Mg and of a single phase solid solution Mg-3-wt.-%-Y showed five-fold higher ductility and (at the same time) lower l_1 intrinsic stacking fault energies in Mg-Y alloys. Prior to this thesis and during its early stages, quantum-mechanical calculations of l_1 intrinsic stacking fault energies in Mg-Y alloys were performed and the computed chemical trend was found to be in a qualitative agreement with experimental findings. The author of this thesis then proposed a multi-scale scheme that explains the macroscopic ductility as a consequence of the lowering of the atomic-scale l_1 intrinsic stacking fault energies (Acta Materialia 60 (2012) 3011).

The first part of the thesis is focused on extending the above mentioned multi-scale connection between atomic-scale stacking fault energy changes and macroscopic ductility beyond Mg-Y alloys. Combining density functional theory calculations and the axial next nearest neighbor Ising (ANNNI) model, the l_1 intrinsic stacking fault energies were computed for 20 different binary Mg alloys containing solutes crystallizing in their pure form either in hexagonal close-packed (hcp) or double hcp (dhcp) structures. Among

the studied solutes, only the 10 rare-earth elements (Sc, Pr, Nd, Gd, Tb, Dy, Ho, Er, Tm, Lu) were found to reduce the l_1 intrinsic stacking fault energy and, consequently, increase the ductility of Mg alloys. Importantly, the theoretically predicted connection between Y and lanthanides in terms of the l_1 stacking fault energy reduction in Mg alloys was established for the first time. The other 10 studied non-rare-earth elements (Be, Tl, Zr, Tc, Re, Co, Ru, Os, Zn, Tl) were, however, found to increase the l_1 intrinsic stacking fault energy (and thus not ameliorate the brittleness in Mg alloys). The former computed results and the theoretical prediction that rare-earth elements increase the ductility in Mg alloys, was experimentally confirmed at MPIE by synthesizing, characterization and testing of Mg-Tb, Mg-Dy, Mg-Ho, and Mg-Er alloys that all turned out to be ductile (Acta Materialia 70 (2014) 92).

The above described part of the research resulted in a theoretical prediction that none of the studied non-rare-earth solutes can increase the ductility in Mg alloys. But the previously considered set of solutes was limited to those crystallizing in either hcp or dhcp structure. An anticipated next step would be to broaden the search and consider more elements from the Periodic table and/or try also multi-component combinations. Specifically in case of higher-order alloys, the number of quantum-mechanical calculations would be exponentially increasing in a combinatorial manner.

In order to avoid these exponentially growing computational expenses, a method allowing for a fast solute assessment without lengthy ab initio calculations was identified. Focusing on known (and tabulated) materials properties of elemental solutes, relations between them and the l_1 stacking fault energies in corresponding Mg alloys containing these solutes have been analyzed. Our analysis of five materials parameters of 18 different elemental solutes showed that the l_1 stacking fault energies are (i) strongly anti-correlated to the atomic volume (Pearson correlation coefficient $r = -0.97$), (ii) correlated to the electronegativity ($r = 0.95$) and (iii) logarithmically related to the bulk modulus ($r = 0.90$). Setting the properties of yttrium (that was found to ductilize Mg alloys) as a reference, so-called yttrium similarity index was proposed based on the above listed three relations. This single numerical quantity combines all three criteria and rationalizes the complexity of prediction of l_1 stacking fault energies. The value of yttrium similarity index ranges from 1 (an ideal match with yttrium) to 0 indicating an element that is maximally different from Y. As this new numerical indicator faithfully reproduced the trends of quantum-mechanically computed stacking fault energies for $Mg_{15}X$ alloys with 18 different solutes, it was evaluated for 76 elements from the periodic table of the elements. Only one non-rare-earth element, lithium, was predicted to reduce the l_1 stacking fault energy. Seeing this limited options in the case of binary Mg alloys, the search for alternative solutes was expanded to ternary Mg alloys.

In order to evaluate ternary alloys, the concept of the yttrium similarity index was extended to multiple -solute states by proposing the use of a virtual element representing concentration-weighted properties (the atomic volume, electronegativity and the bulk modulus) of multiple solutes. This newly introduced yttrium similarity index was then applied within a high-throughput theory-guided rapid prototyping of new ternary Mg-

alloys. Out of 2850 solute combinations tested, 133 solute pairs (not including any rare-earth elements) possess the yttrium similarity index larger than 0.85 and 11 of them have it higher than 0.95 (with the value of 1 indicating an element matching yttrium). Subsequent quantum-mechanical calculations of these 11 solute combinations shown lower I_1 stacking fault energies (compared with the elemental Mg) in case of all of them. Leaving aside at this stage a thermodynamic complexity of multiple solutes, the proposed yttrium similarity index thus proved to be 100 % effective in identifying promising solute candidates that reduce the I_1 stacking fault energy in Mg alloys and are expected to ductilize them (accepted by New Journal of Physics, 2015).

Importantly, the yttrium similarity index has been proposed and used in a direct manner when its value is evaluated for different solutes but its relatively transparent mathematical structure enables also inverse modeling approaches to being applied. This is a major advancement when compared with quantum-mechanical calculations of I_1 stacking fault energies as these calculations are truly difficult (if possible at all) to invert.

After analyzing one specific stacking fault (I_1) and its relation to the ductility in Mg alloys, the research was extended to other stacking faults and energy barriers experienced by dislocations when propagating through Mg alloys. Both these are conveniently studied by computing so-called generalized stacking fault energy surfaces (or gamma-surfaces). Employing quantum-mechanical calculations, generalized stacking fault energies for five slip systems in both elemental magnesium (Mg) and Mg-Y alloys were determined. These calculations predicted that the addition of yttrium results in a reduction in the unstable stacking fault energy of basal slip systems. Specifically in the case of an I_2 stacking fault, the predicted reduction of the stacking fault energy due to Y atoms was experimentally verified by transmission electron spectroscopy (TEM) measurements at the Max-Planck-Institut für Eisenforschung (MPIE) in Düsseldorf. A similar reduction was also found for the stable stacking fault energy of the $\{11\bar{2}2\}$ $\langle11\bar{2}3\rangle$ non-basal slip system. On the other hand, other energies along this particular γ -surface profile increase with the addition of yttrium. In parallel to our quantum-mechanical calculations, a new set of embedded-atom-method (EAM) Mg-Y potentials was developed in cooperation with Prof. H. W. Sheng from the George Mason University in Fairfax, USA. The comparison of quantum-mechanical and atomistic results indicates that the new potential is suitable for future large-scale atomistic simulations (New Journal of Physics 15 (2013) 043020). Lastly, we have combined the quantum-mechanically computed basal-plane generalized stacking fault energies as input for continuum Peierls-Nabarro model in order to predict the geometry and properties of dislocation cores. Using ab initio calculations and Fourier transform we analyze the basal-plane gamma surface in pure Mg and show that the knowledge of energies of only five specific points is sufficient to accurately predict the core structure of $\langle a \rangle$ dislocations. Our 5-point approach greatly reduces the computational costs related to the Peierls-Nabarro model and allow for a high-throughput application of the Peierls-Nabarro model to study dislocation cores changes in Mg upon alloying.

Our approach was employed to study Mg binary alloys containing 9 rare-earth and 11 other solutes that crystallize in either hcp or dhcp structures. Based on the Peierls

stresses of these 20 Mg alloys calculated from the Peierls-Nabarro model, the solutes are divided into three groups: (i) The first group, consisting of Be, Zn, Ti, Tc, Os, Ru, Re and Co when added as solutes into Mg lead to more compact core structures ($3.0 b$ - $7.1 b$, $b=3.19 \text{ \AA}$) and larger Peierls stress than pure Mg (1.9-6.6 MPa). (ii) Elements in the second group, including Ti, Nd, Lu, Zr, Hf, La, and Pr as solutes in Mg change the core widths from $7.0 b$ - $19.2 b$ and Peierls stresses moderately (1.2-1.7 MPa). (iii) The solutes in the third group containing Y, Er, Tm, Ho and Sc extend the core width from $9 b$ - $13 b$, and the resulting Peierls stresses are generally very low (0.46-0.88 MPa). Considering the approximations of our method, we conclude that the the first group has clear solute strengthening effect and the third group has clear solute softening effect, while the effects of second group are unclear. (Physical Review B 92 (2015)064107) To conclude, this thesis collects numerous theoretical findings related to atomic-scale processes and mechanisms governing the plasticity in Mg alloys and these predictions were experimentally tested and, in fact, confirmed. In a divide-and-conquer manner, high-throughput quantum-mechanical calculations have been used to determine solute-induced changes in (i) stacking fault energies, (ii) energy barriers experienced by dislocations in motion and (iii) the geometry and properties of dislocation cores. Despite this thoroughness, a theoretical analysis of twinning processes has only started (and has not been included in the thesis) and a higher-level theoretical model combining all these plasticity mechanisms (and their mutual interplays) is left for future studies. The newly obtained knowledge and understanding have been used to propose new multi-component ductile Mg alloys within a theory-guided combinatorial materials design. Importantly, many of these newly proposed chemical compositions of Mg alloys are rare-earth free. A way towards a new generation of ductile Mg alloys is thus paved.

Bibliography

- [1] S. R. Agnew. *JOM: J. Miner. Met. Mater. Soc.*, 56:20, 2004.
- [2] E. Doege, K. Droeder, and S. Janssen. Wiley-VCH, Weinheim, 2004. chapter 5.
- [3] B. L. Mordike and T. Ebert. *Mater. Sci. Eng. A*, 302:37, 2001.
- [4] E. A. Nyberg, A. A. Luo, K. Sadayappan, and W. Shi. *Adv. Mater. Process*, 166:35, 2008.
- [5] L. B. Railsback. <http://www.gly.uga.edu/railsback/FundamentalsIndex.html>.
- [6] S. Sandlöbes, S. Zaefferer, I. Schestakow, S. Yi, and R. Gonzalez-Martinez. *Acta Mater.*, 59(2):429–439, 2011.
- [7] M. M. Avedesian and H. Baker. *Magnesium and magnesium alloys*, in: *ASM Speciality Handbook*. ASM International, Metals Park, OH, 1999.
- [8] R. von Mises and Z. Angew. *Math. Mech*, 8:161, 1928.
- [9] S. L. Couling, J. F. Pashak, and L. Sturkey. *Trans. ASM*, 51:94–107, 1959.
- [10] K. Momma and F. Izumi. *J. Appl. Crystallogr.*, 44:1272–1276, 2011.
- [11] G. Gottstein. *Physical Foundations of Material Science*. Springer, 2004.
- [12] P. Hirth and J. Lothe. *Theory of Dislocations*. New York Wiley & Sons, 2nd edition, 1982.
- [13] R. Stevens and L. J. Miles. *J. Mater. Sci.*, 11:1911–1918, 1976.
- [14] J. W. Christian and V. Vitek. *Rep. Prog. Phys.*, 33:307–411, 1970.
- [15] A. W. Buff Jr. *Metall. Trans.*, 1:2391–2413, 1970.
- [16] F. E. Hauser, P. R. Landon, and J. E. Dorn. *Trans. ASM*, 48:986, 1956.
- [17] G. V. Raynor. *The Physical Metallurgy of Magnesium and Its Alloys*. New York, NY, 1959.

- [18] M. Nakanishi K. Kubota K. Higashi N. Saito, M. Mabuchi. *Scr. Mater.*, 36(5): 551 – 555, 1997.
- [19] S. R. Agnew, J. A. Horton, and M. H. Yoo. *Metall. Mater. Trans. A*, 33(3): 851–858, 2002.
- [20] W. A. Counts, M. Friák, D. Raabe, and J. Neugebauer. *Acta Mater.*, 57(1):69 – 76, 2009.
- [21] W. A. Counts, M. Friák, D. Raabe, and J. Neugebauer. *Adv. Eng. Mater.*, 12(7): 572–576, 2010.
- [22] N. Stanford, D. Atwell, and M.R. Barnett. *Acta Mater.*, 58(20):6773 – 6783, 2010.
- [23] J. Bohlen, S. Yi, D. Letzig, and K. U. Kainer. *Mater. Sci. Eng. A*, 527(26):7092 – 7098, 2010.
- [24] D. Y. Sun, M. I. Mendelev, C. A. Becker, K. Kudin, T. Haxhimali, M. Asta, J. J. Hoyt, A. Karma, and D. J. Srolovitz. *Phys. Rev. B*, 73:024116, 2006.
- [25] X.-Y. Liu, J. B. Adams, F. Ercolessi, and J. A. Moriarty. *Modell. Simul. Mater. Sci. Eng.*, 4(3):293, 1996.
- [26] J. A. Yasi, T. Nogaret, D. R. Trinkle, Y. Qi, L. G. Hector Jr., and W. A. Curtin. *Modell. Simul. Mater. Sci. Eng.*, 17(5):055012, 2009.
- [27] J. E. Sinclair, P. C. Gehlen, R. G. Hoagland, and J. P. Hirth. *J. Appl. Phys.*, 49: 3890, 1978.
- [28] V. Vítek. *Phil. Mag.*, 154(18):773–786, 1968.
- [29] X.-Y. Cui, H.-W. Yen, S.-Q. Zhu, R. Zheng, and S. P. Ringer. *Journal of Alloys and Compounds*, 620(0):38 – 41, 2015.
- [30] K.-H. Kim, J. B. Jeon, and B.-J. Lee. *Calphad*, 48(0):27 – 34, 2015.
- [31] J. Zhang, Y. Dou, G. Liu, and Z. Guo. *Comput. Mater. Sci.*, 79(0):564 – 569, 2013.
- [32] S. L. Shang, W. Y. Wang, B. C. Zhou, Y. Wang, K. A. Darling, L. J. Kecskes, S. N. Mathaudhu, and Z. K. Liu. *Acta Mater.*, 67(0):168 – 180, 2014.
- [33] C. Wang, H.-Y. Zhang, H.-Y. Wang, G.-J. Liu, and Q.-C. Jiang. *Scr. Mater.*, 69 (6):445 – 448, 2013.
- [34] Z. Pei, L.-F. Zhu, M. Friák, S. Sandlöbes, J. von Pezold, H. W. Sheng, C. P. Race, S. Zaefferer, B. Svendsen, D. Raabe, and J. Neugebauer. *New J. Phys.*, 15 (4):043020, 2013.

- [35] G. Schoeck. *Comput. Mater. Sci.*, 21(1):124 – 134, 2001.
- [36] G. Schoeck. *Mater. Sci. Eng. A*, 333(1-2):390 – 396, 2002.
- [37] S. Sandlöbes, M. Friák, A. Dick, S. Zaefferer, S. Yi, D. Letzig, Z. Pei, L.-F. Zhu, J. Neugebauer, and D. Raabe. *Acta Mater.*, 2012.
- [38] T. Tsuru, Y. Udagawa, M. Yamaguchi, M. Itakura, H. Kaburaki, and Y. Kaji. *J. Phys.: Condens. Matter*, 25(2):022202, 2013.
- [39] G. Schoeck. *Mater. Sci. Eng. A*, 400-401(0):7 – 17, 2005.
- [40] T. Nogaret, W. A. Curtin, J. A. Yasi, L. G. Hector Jr., and D. R. Trinkle. *Acta Mater.*, 58(13):4332 – 4343, 2010.
- [41] D. Ma, M. Friák, J. von Pezold, D. Raabe, and J. Neugebauer. *Acta Mater.*, 85 (0):53 – 66, 2015.
- [42] G. P. M. Leyson, L. G. Hector Jr., and W. A. Curtin. *Acta Mater.*, 60(13-14): 5197 – 5203, 2012. ISSN 1359-6454.
- [43] R. Martin. *Electronic Structure: Basic Theory and Practical Applications*. Cambridge University Press, Cambridge.
- [44] R. Car and M. Parrinello. *Phys. Rev. Lett.*, 55:2471–2474, 1985.
- [45] R. Labusch. *physica status solidi (b)*, 41(2):659–669, 1970.
- [46] P. Hohenberg and W. Kohn. *Phys. Rev.*, 136:B864, 1964.
- [47] W. Kohn and L. J. Sham. *Phys. Rev.*, 140:A1133, 1965.
- [48] S.L. Shang, A. Saengdeejing, Z.G. Mei, D.E. Kim, H. Zhang, S. Ganeshan, Y. Wang, and Z.K. Liu. *Comput. Mater. Sci.*, 48(4):813 – 826, 2010.
- [49] K. Lejaeghere, V. Van Speybroeck, G. Van Oost, and S. Cottenier. *Critical Reviews in Solid State and Materials Sciences*, 39(1):1–24, 2014.
- [50] M. Born and J. R. Oppenheimer. *Ann. Phys.*, 84(20):457–484, 1927.
- [51] J. Kohanoff. *Electronic structure calculations for solids and molecules: theory and computational methods*. Cambridge University Press, 2006.
- [52] R. G. Parr and W. Yang. *Density-functional theory of atoms and molecules*. Oxford University Press, 1989.
- [53] P. A. M. Dirac. *Proc. Cambridge Phil. Soc.*, 26:376, 1930.
- [54] J. P. Perdew, K. Burke, and M. Ernzerhof. *Phys. Rev. Lett.*, 77:3865–3868, 1996.

- [55] J. Tao, J. P. Perdew, V. N. Staroverov, and G. E. Scuseria. *Phys. Rev. Lett.*, 91: 146401, 2003.
- [56] H.-V. Nguyen and S. de Gironcoli. *Phys. Rev. B*, 79:205114, 2009.
- [57] A. D. Becke. *The Journal of Chemical Physics*, 98(2):1372–1377, 1993.
- [58] A. D. Becke. *The Journal of Chemical Physics*, 98(7):5648–5652, 1993.
- [59] F. Jensen. *Introduction to Computational Chemistry*. Wiley, Chichester, 2 edition.
- [60] M. Daw and M. Baskes. *Phys. Rev. Lett.*, 50:1285–1288, 1983.
- [61] M. Daw and M. Baskes. *Phys. Rev. B*, 29:6443–6453, 1984.
- [62] M. W. Finnis and J. E. Sinclair. *Philosophical Magazine A*, 50(1):45–55, 1984.
- [63] M. E. Fisher and W. Selke. *Phys. Rev. Lett.*, 44:1502, 1980.
- [64] R. J. Elliot. *Phys. Rev.*, 124:346, 1961.
- [65] M. E. Fisher. *Physics Letters*, 170(4):213–264, 1988. Physics Reports.
- [66] A. Dick, T. Hickel, and J. Neugebauer. *Steel Res. Int.*, 80(9):603–608, 2009.
- [67] Q.-M. Hu and R. Yang. *Acta Mater.*, 61(4):1136 – 1145, 2013.
- [68] K. Schwarz, P. Blaha, and G. K. H. Madsen. *Comput. Phys. Commun.*, 147(1-2): 71 – 76, 2002.
- [69] G. Kresse and J. Hafner. *J. Phys. Rev. B*, 47:558, 1993.
- [70] G. Kresse and J. Furthmüller. *Phys. Rev. B*, 64:11169–11186, Oct 1996.
- [71] G. Kresse and J. Furthmüller. *J. Comput. Mater. Sci.*, 6:15, 1996.
- [72] G. Kresse and J. Joubert. *Phys. Rev. B*, 59:1758, 1999.
- [73] F. D. Murnaghan. *Proc. Nat. Acad. Sci.*, 30:244, 1944.
- [74] C.-L. Fu and K.-M. Ho. *Phys. Rev. B*, 28:5480, 1983.
- [75] D. R. Lide. *Handbook of Chemistry and Physics*. CRC, 86 edition, 2005-2006.
- [76] S. R. Agnew, L. Capolungo, and C. A. Calhoun. *Acta Mater.*, 82(0):255 – 265, 2015.
- [77] S. Sandlöbes, Z. Pei, M. Friák, L.-F. Zhu, F. Wang, S. Zaefferer, D. Raabe, and J. Neugebauer. *Acta Mater.*, 70(0):92 – 104, 2014.

- [78] J. A. Yasi, L. G. Hector Jr., and D. R. Trinkle. *Acta Mater.*, 58(17):5704 – 5713, 2010.
- [79] J. A. Yasi, L. G. Hector Jr., and D. R. Trinkle. *Acta Mater.*, 60(5):2350 – 2358, 2012.
- [80] I. Shin and E. A. Carter. *Modell. Simul. Mater. Sci. Eng.*, 20(1):015006, 2012.
- [81] I. Shin and E. A. Carter. *Int. J. Plasticity*, 60(0):58 – 70, 2014.
- [82] *periodictable.com*.
- [83] <https://www.wikipedia.org>.
- [84] L.-F. Zhu, M. Friák, A. Dick, B. Grabowski, T. Hickel, F. Liot, D. Holec, A. Schlierer, U. Kühn, J. Eckert, Z. Ebrahimi, H. Emmerich, and J. Neugebauer. *Acta Mater.*, 60:1594, 2012.
- [85] S. B. Maisel, M. Höfler, and S. Müller. *Nature*, 491:740, 2012.
- [86] P. Hemzalová, M. Friák, M. Šob, D. Ma, A. Udyansky, D. Raabe, and J. Neugebauer. *Phys. Rev. B*, 88:174103, 2013.
- [87] Z. Li, X. Gu, S. Lou, and Y. Zheng. *Biomaterials*, 29(10):1329 – 1344, 2008.
- [88] M. Salahshoor and Y. Guo. *Materials*, 5(1):135–155, 2012.
- [89] Q. Ma, D. H. St. John, and M. T. Frost. *Scr. Mater.*, 46(9):649 – 654, 2002.
- [90] P. E. Blöchl. *Phys. Rev. B*, 50:17953, 1994.
- [91] J. Koike, T. Kobayashi, T. Mukai, H. Watanabe, M. Suzuki, K. Maruyama, and K. Higashi. *Acta Mater.*, 51(7):2055 – 2065, 2003.
- [92] M. H. Yoo, J. R. Morris, K. M. Ho, and S. R. Agnew. *Metall. Trans. A*, 33A:813, 2002.
- [93] M. H. Yoo. *Metall. Trans. A*, 12A:409–18, 1981.
- [94] M. H. Yoo and J. K. Lee. Deformation twinning in h.c.p. metals and alloys. *Phil. Mag. A*, 63(5):987–1000, 1991.
- [95] M. Muzyk, Z. Pakiela, and K. J. Kurzydlowski. *Scr. Mater.*, 66(5):219 – 222, 2012.
- [96] J. Han, X. M. Su, Z.-H. Jin, and Y. T. Zhu. *Scr. Mater.*, 64(8):693 – 696, 2011.
- [97] E. B. Tadmor and N. Bernstein. *Journal of the Mechanics and Physics of Solids*, 52(11):2507 – 2519, 2004.

- [98] P. E. Blöchl. *Phys. Rev. B*, 50:17953–17979, 1994.
- [99] D. R. Lide. *Handbook of Chemistry and Physics*. CRC Press, 86 edition, 2005–2006.
- [100] S. F. Plimpton. *J. Comput. Phys.*, 117(1):1 – 19, 1995.
- [101] C. S. Barrett and T. B. Massalski. *Structure of Metals*, volume 2. McGraw-Hill, New York, 1966.
- [102] C. Kittel. *Introduction to Solid State Physics*. Wiley, New York, 1976.
- [103] G. Simons and H. Wang. *Single Crystal Elastic Constants and Calculated Aggregate Properties*. MIT Press, Cambridge, MA, 1977.
- [104] W. C. M. Matterns A. R. Miedema F. R. de Boer, R. Boom and A. K. Niessen. *Cohesion in Metals: Transition Metal Alloys*. Noh-Holland, Amsterdam, 1988.
- [105] F. C. Campbell. *Elements of metallurgy and engineering alloys*. ASM International, 2008.
- [106] M. S. Daw S. M. Foiles, M. I. Baskes. *Phys. Rev. B*, 33:7983, 1986.
- [107] A. Cadien T. Fujita H. W. Sheng, M. J. Kramer and M.W. Chen. *Phys. Rev. B*, 83:134118, 2011.
- [108] B. Y. Huang F. Gao W. Y. Hu, B .W. Zhang and D. J. Bacon. *J. Phys.: Condens. Matter*, 13:1193, 2001.
- [109] M. I. Baskes and R. A. Johnson. *Modell. Simul. Mater. Sci. Eng.*, 2:147, 1994.
- [110] J.B. Adams F. Ercolessi. *Europhys. Lett.*, 26:583, 1994.
- [111] F. Gahler P. Brommer. *Modell. Simul. Mater. Sci. Eng.*, 15:295, 2007.
- [112] P. Villars. *Perarson's Handbook: Desk Edition*. ASM, 1997.
- [113] G. Kresse and J. Hafner. *Phys. Rev. B*, 49:14251, 1994.
- [114] <https://sites.google.com/a/gmu.edu/eam-potential-database/Home/MgY>.
- [115] J. R. Morris, J. Scharff, K. M. Ho, D. E. Turner, Y. Y. Ye, and M. H. Yoo. *Phil. Mag. A*, 76(5):1065–1077, 1997.
- [116] C. Woodward and S. I. Rao. *Phys. Rev. Lett.*, 88:216402, 2002.
- [117] G. Leibfried and H. D. Dietze. *Z. Physik*, 131:113, 1951.
- [118] R. Wang, S. F. Wang, X. Z. Wu, and Q. Y. Wei. *Physica Scripta*, 81(6):065601, 2010.

- [119] V. V. Bulatov and E. Kaxiras. *Phys. Rev. Lett.*, 78:4221–4224, 1997.
- [120] G. Lu, N. Kioussis, V. V. Bulatov, and E. Kaxiras. *Mater. Sci. Eng. A*, 309-310 (0):142–147, 2001.
- [121] J. Kennedy and R. Eberhart. Particle swarm optimization. *IEEE*, page 1942, 1995.
- [122] R. Poli. *Journal of Artificial Evolution and Applications*, 2008:1–10, 2008.
- [123] R. E. Smallmann and P. S. Dobson. *Metal. Trans.*, 1:2383, 1970.
- [124] E. Schmid. *Z. Elektrochem*, 37:447, 1931.
- [125] P. W. Bakarian and C. H. Mathewson. *Trans. AIME*, 152:226, 1943.
- [126] H. Conrad and W. D. Robertson. *Trans. AIME*, 209:503, 1957.
- [127] <https://www.vasp.at/vasp-workshop/slides/pseudoppdatabase.pdf>.

Appendices

Electronic Configurations of Elements

In the following table listed are the electronic configurations of the elements and configurations of their valence electrons which are employed in the VASP software package [69, 70, 71]. For Pr, Nd, Tb, Dy, Ho, Er and Tm, the potentials created for valency 3 are employed (X_3) and their valence electron configurations are not explicitly shown here. The readers are referred to Ref. [127] for more details.

Table A.1:

The electronic configurations and the electrons considered as valence electrons in the pseudopotentials used in ab-initio calculations. Val. el. is the abbreviation of the valence electrons.

Element	Configuration	Val. el.	Element	Configuration	Val. el.
Mg	[Ne]2s ²	2s ²	Pr	[Xe]4f ³ 6s ²	-
Zn	[Ar]3d ¹⁰ 4s ²	4s ² 3d ¹⁰	Nd	[Xe]4f ⁴ 6s ²	-
Tl	[Xe]4f ¹⁴ 5d ¹⁰ 6s ² 6p ¹	6s ² 6p ¹ 5d ¹⁰	Gd	[Xe]4f ⁷ 5d ¹ 6s ²	5p ⁶ 5d ¹ 6s ²
Zr	[Kr]4d ² 5s ²	4d ² 5s ²	Tb	[Xe]4f ⁹ 6s ²	-
Be	[He]2s ²	2s ²	Dy	[Xe]4f ¹⁰ 6s ²	-
Ti	[Ar]3d ² 4s ²	3p ⁶ 4s ² 3d ²	Ho	[Xe]4f ¹¹ 6s ²	-
Re	[Xe]4f ¹⁴ 5d ⁵ 6s ²	5p ⁶ 5d ⁵ 6s ²	Er	[Xe]4f ¹² 6s ²	-
Co	[Ar]3d ⁷ 4s ²	3d ⁷ 4s ²	Tm	[Xe]4f ¹³ 6s ²	-
Os	[Xe]4f ¹⁴ 5d ⁶ 6s ²	5p ⁶ 6s ² 5d ⁶	Lu	[Xe]4f ¹⁴ 5d ¹ 6s ²	5p ⁶ 5d ¹ 6s ²
Ru	[Kr]4d ⁷ 5s ¹	4p ⁶ 5s ¹ 4d ⁷	Sc	[Ar]3d ¹ 4s ²	3p ⁶ 4s ² 3d ¹
Tc	[Kr]4d ⁵ 5s ²	4p ⁶ 5s ² 4d ⁵	Y	[Kr]4d ¹ 5s ²	4s ² 4p ⁶ 5s ² 4d ¹

Symbols: [He]=1s², [Ne]=[He]2s²2p⁶, [Ar]=[Ne]3s²3p⁶, [Kr]=[Ar]3d¹⁰4s²4p⁶, [Xe]=[Kr]4d¹⁰5s²5p⁶.

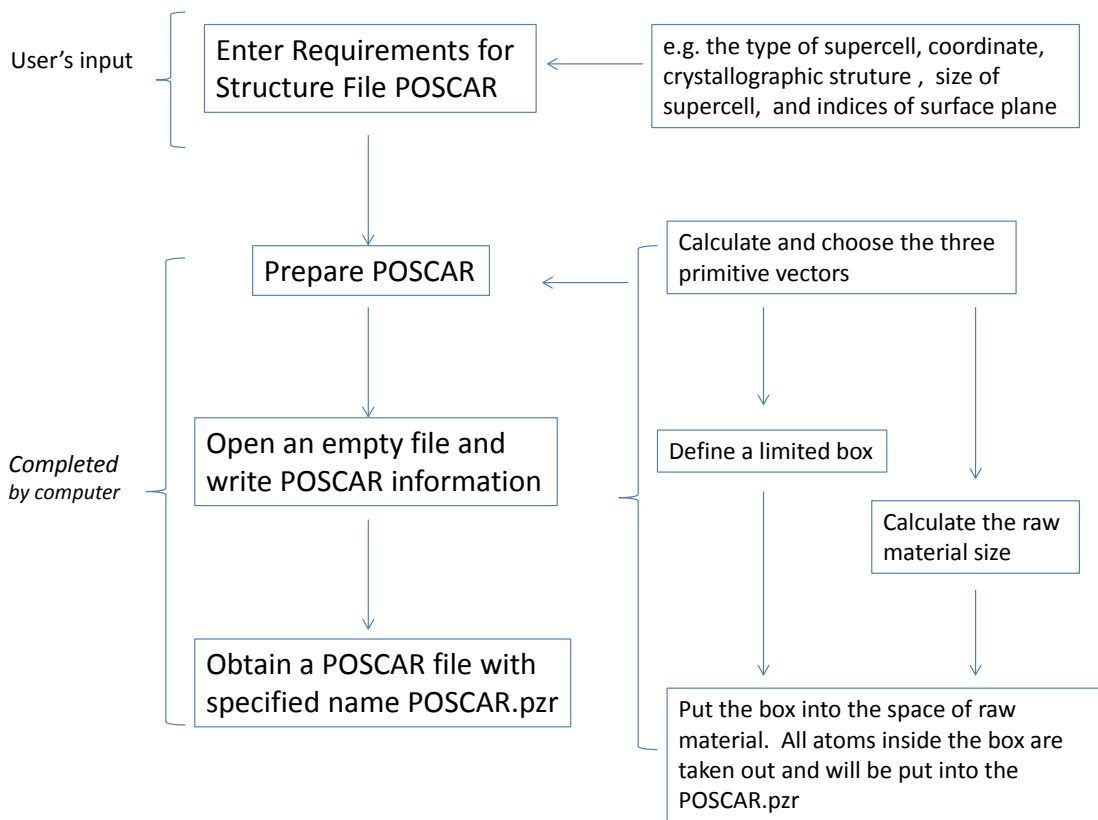


Figure A.1:
The flow chart of the algorithm employed in POSCAR Creator.

Software Tools to Generate Supercells of Slip Systems

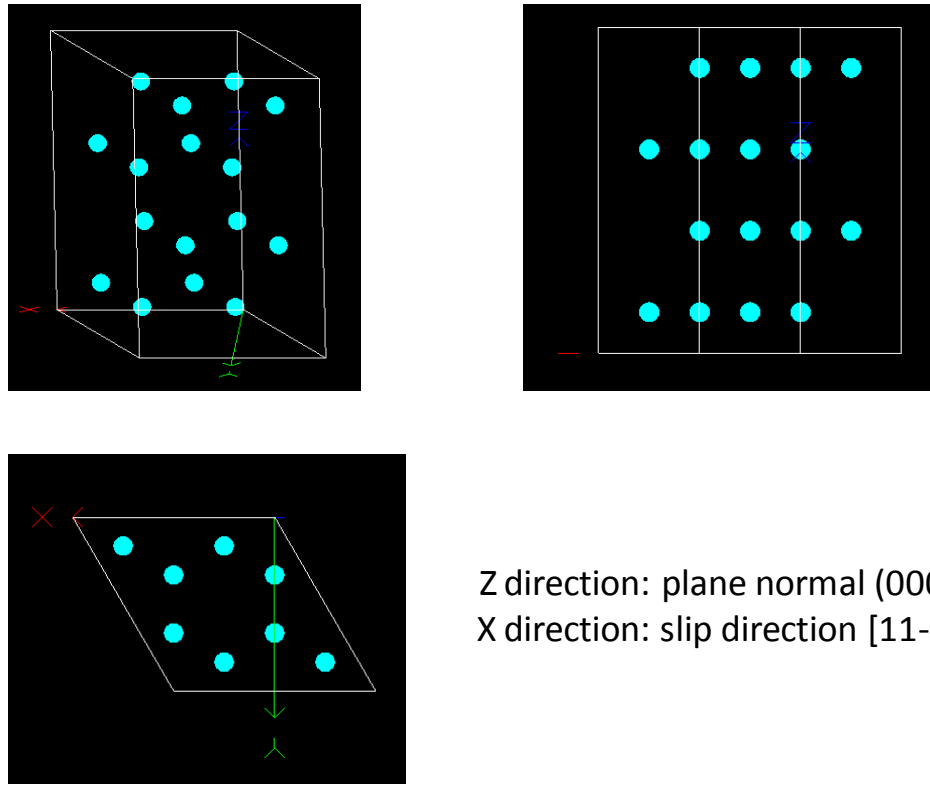
To introduce a generalized stacking fault into a supercell we need to firstly define a slip plane and a slip direction. For convenience we can define the surface of the supercell as the slip plane and one primitive vector of the supercell as the slip direction. However it is not easy to construct such a supercell for, e.g., hexagonal crystal structures. To tackle this problem the author has written two codes using C++ and OpenGL. One generates a supercell (named as POSCAR_Creator) and the other visualizes the created supercell (POSCAR View).

POSCAR_Creator creates input-structure file which can be used directly by the VASP code. The idea of POSCAR_Creator is to construct of a limited and closed parallelepiped space (a box). One pair of the box surface is chosen to be parallel to the slip plane in question. The built parallelepiped box is inserted into a large lattice space with designated crystallographic structure (so-called raw material in Figure A.1); and all the atoms inside the box belong to the supercell (see Figure A.1) and the others are removed.

The design of such a box requires tedious mathematical operations involving matrix and vector algebra. Constructing a parallelepiped box requires three vectors and three

lengths. The three vectors are the three primitive vectors which determine the directions of the twelve edges of the box and thus finally the plane normals of the six sides. The three lengths determine the length of the twelve edges of the box and thus finally the number of atoms in the supercell. The search of suitable primitive vectors is completed by the algorithm. The three lengths must be supplied by the user.

The second code is used to visualize the structure file. With the help of POSCAR_View the user can easily judge whether the structure created by POSCAR_Creator is correct or not. Therefore, POSCAR_View is complementary to POSCAR_Creator. POSCAR_View is compiled in the framework of OpenGL, which is a powerful tool to write code for rendering graphics. It supplies quantities of encapsulated functions which can be invoked directly by users. By employing these functions the visualization can be realized in an easy and convenient way. Figure A.2 is an example of application of POSCAR_View to basal $\langle a \rangle$ slip.



Z direction: plane normal (0001);
 X direction: slip direction [11-20].

Figure A.2:

Schematic figure of the 16-atom supercell for glide system $\{0001\}\langle 11\bar{2}0 \rangle$. The figures are generalized by POSCAR_View, a code to visualize the atomic positions in a supercell.

Elemental Solute Properties

The elemental properties employed in yttrium similarity index in chapter 4 and 5 are listed in Table A.2. These data are taken from Refs. [82] and [83].

Table A.2:

"No." is atomic number, "El." the abbreviation of elements. The 3rd column to 5th are electronegativity ν (by Pauling scale), bulk modulus B and atomic volume V .

No.	El.	ν	B (GPa)	V (\AA^3)	YSI	No.	El.	ν	B (GPa)	V (\AA^3)	YSI
1	H	2.2	41	1.19	0.504	44	Ru	2.2	220	13.60	0.514
3	Li	0.98	11	21.50	0.837	45	Rh	2.28	380	13.70	0.328
4	Be	1.57	130	8.09	0.657	46	Pd	2.2	180	14.70	0.553
5	B	2.04	320	7.30	0.406	47	Ag	1.93	100	17.10	0.684
6	C	2.55	33	8.83	0.472	48	Cd	1.69	42	21.60	0.793
7	N	3.04	41	1.40	0.287	49	In	1.78	41	26.10	0.796
8	O	3.44	41	0.89	0.167	50	Sn	1.96	58	27.00	0.741
9	F	3.98	41	0.59	0.001	51	Sb	2.05	42	30.20	0.720
11	Na	0.93	6.3	39.50	0.866	52	Te	2.1	65	34.00	0.703
13	Al	1.61	76	16.60	0.761	53	I	2.66	7.7	42.70	0.502
14	Si	1.9	100	20.00	0.711	55	Cs	0.79	1.6	117.00	0.000
15	P	2.19	11	28.20	0.667	56	Ba	0.89	9.6	65.00	0.607
16	S	2.58	7.7	27.20	0.537	57	La	1.1	28	37.50	0.931
17	Cl	3.16	1.1	3.94	0.264	58	Ce	1.12	22	34.80	0.951
19	K	0.82	3.1	75.90	0.478	59	Pr	1.13	29	35.30	0.956
20	Ca	1	17	43.00	0.858	60	Nd	1.14	32	34.20	0.967
21	Sc	1.36	57	25.00	0.892	62	Sm	1.17	38	34.00	0.979
22	Ti	1.54	110	17.60	0.765	63	Eu	1.2	8.3	48.10	0.816
23	V	1.63	160	13.80	0.679	64	Gd	1.2	38	33.10	0.992
24	Cr	1.66	160	12.10	0.660	65	Tb	1.2	38.7	32.10	0.987
25	Mn	1.55	120	12.20	0.706	66	Dy	1.22	41	31.60	0.983
26	Fe	1.83	170	11.80	0.621	67	Ho	1.23	40	31.20	0.978
27	Co	1.88	180	11.00	0.598	68	Er	1.24	44	30.60	0.971
28	Ni	1.91	180	10.90	0.592	69	Tm	1.25	45	30.10	0.964
29	Cu	1.9	140	11.80	0.630	70	Yb	1.1	31	43.80	0.867
30	Zn	1.65	70	15.20	0.743	71	Lu	1.27	48	29.50	0.955
31	Ga	1.81	41	19.60	0.748	72	Hf	1.3	110	22.30	0.833
32	Ge	2.01	75	22.70	0.704	73	Ta	1.5	200	18.10	0.684
33	As	2.18	22	21.70	0.651	74	W	2.36	310	15.90	0.401
34	Se	2.55	8.3	27.20	0.547	75	Re	1.9	370	14.70	0.403
35	Br	2.96	1.9	42.50	0.404	76	Os	2.2	462	14.00	0.237
37	Rb	0.82	2.5	92.70	0.287	77	Ir	2.2	320	14.20	0.415
38	Sr	0.95	41	55.30	0.724	78	Pt	2.28	230	15.40	0.496
39	Y	1.22	41	33.00	1.000	79	Au	2.54	220	17.00	0.446
40	Zr	1.33	91.1	23.30	0.857	80	Hg	2	25	24.60	0.720
41	Nb	1.6	170	18.00	0.705	81	Tl	1.62	43	28.70	0.857
42	Mo	2.16	230	15.50	0.524	82	Pb	2.33	46	30.40	0.627
43	Tc	1.9	41	14.20	0.683	83	Bi	2.02	31	35.50	0.730

Curriculum Vitae

Personal Data

Name: Zongrui Pei
Date of Birth: October 29th, 1986
Place of Birth: Henan, China

Education

2005-2009 Bachelor, study Material Science and Engineering in University of Science and Technology, Beijing (USTB)
2009-2012 Master, study Metallurgical Engineering in Rheinisch-Westfaelische Technische Hochschule Aachen (RWTH Aachen)
2012-2015 Doctorand, study in Aachen Institute for advanced study in Computational Engineering Science (AICES) in RWTH Aachen, and Max-Planck-Institut für Eisenforschung (MPIE), GmbH, Düsseldorf

Publications

1. S. Sandlöbes, M. Friák, S. Zaefferer, A. Dick, S. Yi, D. Letzig, Z. Pei, L.-F. Zhu, J. Neugebauer, D. Raabe, The relation between ductility and stacking fault energies in Mg and Mg-Y alloys, *Acta Materialia* 60 (6), 3011-3021, 2012.
2. Z. Pei, L.-F. Zhu, M. Friák, S. Sandlöbes, J. von Pezold, H. W. Sheng, C. P. Race, S. Zaefferer, B. Svendsen, D. Raabe, J. Neugebauer, Ab initio and atomistic study of generalized stacking fault energies in Mg and Mg-Y alloys, *New Journal of Physics* 15 (4), 043020, 2013.
3. S. Sandlöbes, Z. Pei, M. Friák, L.-F. Zhu, F. Wang, S. Zaefferer, D. Raabe, J. Neugebauer, Ductility improvement of Mg alloys by solid solution: Ab initio modeling, synthesis and mechanical properties, *Acta Materialia* 70, 92-104, 2014.
4. Z. Pei, M. Friák, S. Sandlöbes, R. Nazarov, B. Svendsen, D. Raabe, J. Neugebauer, Rapid theory-guided prototyping of ductile Mg alloys: from binary to higher-order materials, *New Journal of Physics*, 2015, in press.
5. Z. Pei, D. Ma, M. Friák, B. Svendsen, D. Raabe, J. Neugebauer, From generalized stacking fault energies to dislocation cores: impact of solutes on the Peierls stress in magnesium, *Physical Review B* 92, 064107, 2015.

Conferences & Workshops

1. Z. Pei, S. Sandlöbes, S. Zaefferer, A. Dick, M. Friák, L.-F. Zhu, S. Yi, D. Letzig, D. Raabe, and J. Neugebauer, Ab initio stacking fault energy calculations in Mg-Y alloys. DPG spring meeting, March 10-15, 2013, Regensburg, Germany.
2. Z. Pei, L.-F. Zhu, M. Friák, S. Sandlöbes, S. Zaefferer, B. Svendsen, J. Neugebauer, D. Raabe, Ab initio study of stacking fault energies in Mg alloys. European Congress and Exhibition on Advanced Materials and Processes (EUROMAT2013), September 8-13, 2013, Sevilla, Spain.
3. Z. Pei, M. Friák, B. Svendsen, D. Raabe, J. Neugebauer, Ab initio study of stacking fault energies in Mg alloys. AICES retreat, September 23-25, 2013, Vaals, Netherlands.
4. Z. Pei, L.-F. Zhu, M. Friák, S. Sandlöbes, S. Zaefferer, B. Svendsen, D. Raabe, J. Neugebauer, Relation between thermodynamic stability and stacking fault energies in Mg alloys: An ab-initio study. DPG spring meeting, March 30- April 4, 2014, Dresden, Germany.
5. Z. Pei, L.-F. Zhu, M. Friák, S. Sandlöbes, H. Sheng, B. Svendsen, D. Raabe, J. Neugebauer, Ab initio and atomistic study of generalized stacking fault energies in Mg and Mg-Y alloys. 12th Junior Euromat, July 21-25, 2014, Lausanne, Switzerland.
6. Z. Pei, L.-F. Zhu, M. Friák, S. Sandlöbes, S. Zaefferer, B. Svendsen, D. Raabe, J. Neugebauer, Ab initio study of stacking fault energies in Mg alloys, Materials Science and Engineering Congress, September 23-25, 2014, Darmstadt, Germany.
7. Z. Pei, M. Friák, S. Sandlöbes, B. Svendsen, S. Zaefferer, D. Raabe, J. Neugebauer, Ab-initio Guided Materials Design of Ductile Mg Alloys. MRS Fall Meeting, December 1-5, 2014, Boston, USA.
8. Z. Pei, D.Ma, M. Friák, J. Neugebauer, Impact of solutes on the Peierls stress in magnesium: A Peierls-Nabarro model study. 2nd German-Austrian Workshop "Computational Materials Science on Complex Energy Landscapes", January 19-23, 2015, Kirchdorf, Austria.
9. HLRS Parallel Programming Workshop, November 26-27, 2012, Jülich, Germany.
10. 45th IFF Spring School, "Computing Solids: Models, ab-initio methods and supercomputing", March 10-21, 2014, Jülich, Germany.